TECHNISCHE UNIVERSITÄT MÜNCHEN

Lehrstuhl für Klinik und Poliklinik für Nuklearmedizin

Contrast Agent Development and Delivery for Optoacoustic Imaging

Yuanyuan Jiang

Vollständiger Abdruck der von der Fakultät für Medizin der Technischen Universität München zur Erlangung des akademischen Grades eines

Doktors der Naturwissenschaften

genehmigten Dissertation.

Vorsitzende(r): Prof. Dr. Claus Zimmer

Prüfer der Dissertation:

1. Prof. Dr. Gil Gregor Westmeyer
2. Prof. Dr. Wolfgang Wurst

Die Dissertation wurde am 14.06.2016 bei der Technischen Universität München eingereicht und durch die Fakultät für Medizin am 04.01.2017 angenommen.

Abstract

Advanced molecular imaging technology provides exciting opportunities for quantitative visualization of biochemical events at a cellular and molecular level. It is driven by the novel technology of imaging instrumentations and the expansion of specific targeted reporters/probes to differentiate targets from non-specific background signals. Multispectral optoacoustic tomography (MSOT), is an emerging noninvasive imaging modality that combines the optical excitation and ultrasound signal detection based on the photoacoustic effect. It has the ability to create real-time, volumetric, multispectral, and multiscale images from organelles to organs. Employing multispectral illumination on the optical absorbing molecules, MSOT has been shown to be a powerful tool for resolving tissue chromophores or exogenous contrast agents with high spatial and temporal resolution at imaging depths of centimeters.

This presented work includes three strategies to enhance the sensitivity and potential applications for optoacoustic imaging technique. The first study was carried out in the spectral domain and aims to examine genetically encoded pigments with properties such as minimum photobleaching, near-infrared range absorption and enzymatically amplification for greater optoacoustic signal efficiency. The biosynthetic pigment violacein exhibits these beneficial photophysical properties and has been shown to a valuable bacterial label for high resolution, three-dimensional bacterial imaging. Additionally, the time domain is examined to understand how it can be used to identify contrast agents that change their signal trajectories in response to controlled laser pulses. Specifically, it is demonstrated how reversibly switchable fluorescent proteins (RSFPs) could be identified with a high sensitivity based on their photocontrolled signal trajectories. This 'temporal unmixing' is possible with high contrast- to-noise ratios, even in the presence of strongly absorbing blood. To enable molecular neuroimaging in rodents, a technique for the ultrasound-mediated blood-brain barrier opening is adapted for delivering synthetic contrast agents to a large portion of the rodent brain. These approaches will help facilitate molecular optoacoustic imaging to for basic research and biomedical studies on preclinical disease models.

Abbreviations

MSOT	Multispectral optoacoustic tomography
FSFP	Reversibly switchable fluorescent protein
CNR	Contrast noise ratio
MRI	Magnetic resonance imaging
CT	Computed tomography
US	Ultrasound
PET	Positron emission tomography
SPECT	Single photon emission computed tomography
OA	Optoacoustic
FOV	Field of view
FMT	Fluorescence molecular tomography
BLI	Bioluminescence imaging
SPIO	Superparamagnetic iron oxide
FDG	Fluorodeoxyglucose
MFP	Mean free path
TMFP	Transport mean free path
FP	Fluorescent protein
FPS	Fluorescent proteins
ICG	Indocyanine green
OPO	Optical parametric oscillator
SNR	Signal-to-noise ratio
NIR	Near-infrared
PCA	Principal component analysis
ICA	Independent component analysis
VCA	Vertex component analysis
HbO_2	Oxyhemoglobin

Hb	Deoxyhemoglobin
CBV	Cerebral blood volume
HbT	Total hemoglobin
BOLD	Blood oxygen level dependent
fMRI	Functional MRI
OCT	Optical coherence tomography
GFP	Green fluorescent proteins
iRFP	Near-infrared fluorescent protein
BphP	Bacteriophytochrome photoreceptor
TYR	Tyrosinase
DOX	Doxycycline
BBB	Blood-brain barrier
Vio	Violacein
PAFPs	Photoactivatable fluorescent proteins
PSFPs	Photoactivatable fluorescent proteins
tuMSOT	Temporally unmixed MSOT
MIP	Maximum intensity projection
ROI	Region of interest
PRF	Pulse repetition frequency
PL	Pulse length
Gd	Gadolinium
RARE	Acquisition with relaxation enhancement
MEMRI	Manganese-enhanced MRI
CSF	Cerebrospinal fluid
MI	Mechanical Index

Contents

Chapter 1 Introduction

1.1 Molecular imaging

Molecular imaging has grown exponentially in the past decades and is currently an active field for preclinical disease diagnosis and therapy [1][2]. Generally, molecular imaging aims for noninvasive, real-time visualization of biochemical events at a cellular and molecular level within living cells, tissues, and subjects [3]. In the past years, advanced imaging technologies and image probes have been developed at a rapid pace enabling a variety of methods for understanding complex biological phenomena, identifying regions of pathology, providing unique insights regarding the mechanisms of disease, and supporting the translations to clinic practices [4].

The fundamental components for the acquisition of molecular level structural and/or functional information include imaging instruments, target tools, and animal models. Advances in *in vivo* imaging technologies are now extending clinical researchers that beyond traditional *ex vivo* studies. A number of imaging modalities have been used in animals, including magnetic resonance imaging (MRI), X-ray computed tomography (CT), ultrasound (US), positron emission tomography (PET) and single photon emission computed tomography (SPECT), optical imaging and optoacoustic (OA) imaging, among others. Small animal imaging technology not only benefits understanding of the mechanisms of diseases but also benefits the clinical practices [5]. Targeting mouse models for human diseases, ranging from cancer to Alzheimer's disease, researchers can find vital clues to the causes, diagnosis, and treatment of these disorders [6]. The increasing availability of proteins, synthetic dyes and other probes enables researchers to study gene expression, protein function, and cellular processes. More recently, the progress of molecular imaging has become particularly dependent on novel multi-functionalized imaging probes, which are highly sensitive for monitoring the cellular level interactions. To address the aims of molecular level visualization, there is rising emphasis on the development of appropriate probes to monitor interactions in animal models.

1.2 Imaging modalities and contrast agents

From the perspective of imaging dimensions, there are two major groups of imaging modalities. The first group has a variable size for preclinical dimension of small imaging and human-based clinical studies. It includes CT, MRI, US, nuclear imaging modalities (PET, SPECT), and the multi-modality approaches. The second group, mainly based on the photonics is macroscopic imaging. Traditional three-dimensional *in vivo* microscopy (such as confocal, two-photon microscopy) methods, based on detected photons, are typically suitable for transparent live specimens or small mammals, as their limited penetration depth below 1 mm and a restricted field of view (FOV) [7]. Novel optical imaging methods like fluorescence molecular tomography (FMT), and bioluminescence imaging (BLI) are accomplished through advanced developments in fluorescent or bioluminescent reporter probes, activatable, and targeted fluorescent strategies. In considering the limits of penetration which arise from optical method, a promising modality, OA imaging, overcomes the problematic aspects of penetration and allows a depth of several millimeters to centimeters and high spatial resolution within 20-200 μm [8]. The choice of imaging modality primarily depends on the specific question to be addressed. Table 1.1 gives a short overview of available small animal systems and their parameters.

X-ray computed tomography is the classical anatomical imaging modality and provides high contrast to lung and skeletal structures. The limitless penetration depth and high spatial and temporal resolution makes CT imaging widely used in clinical and preclinical scans to acquire methodological information. The disadvantage of CT is its high ionizing radiation, poor sensitivity to imaging agents, and limited soft tissue resolution. The word *tomography* in CT technology means to examine a slice or planar section of an object at a time. The information obtained from tomography is actually a map of the attenuation coefficient, a cross-section map of the body, which at a given energy is a function of the density and atomic number (Z) of the object. Hence, objects containing heavy elements give rise to higher attenuation. Therefore, these elements with relatively high atomic numbers such as iodine and bromine have been used as contrast agent. The standard iodine agents are encapsulated in liposomes or polymers because of their high toxicity [9]. Currently, with advanced surface chemistry manipulation and the high Z elements, gold nanoparticles are good candidates for x-ray angiography contrast agents. However, the low sensitivity of CT compatible contrast agents impedes CT from being a method for obtaining molecular level biochemical information.

Magnetic resonance imaging is widely used in biomedical research due to its noninvasive nature and high spatial resolution. It can provide qualitative diagnostic information, morphometric readouts, as well as the spatiotemporal patterns of brain activity. Magnetic resonance imaging uses a powerful magnetic field to align the protons. The magnetization alignment is systematically altered when radio

frequency pulses are applied and then receiving coil detects the emission of electromagnetic radiation. The MRI signal comes from protons in water and the molecular agents in solution interact with water molecules to influence (shorten) parameters of the T_1 and T_2 relaxation time. The most common contrast agents are complexes containing irons of paramagnetic lanthanide gadolinium, the divalent metal manganese, and superparamagnetic iron oxide (SPIO). However, one major drawback of this imaging method is its relatively poor temporal resolution and limited sensitivity to contrast agents.

Ultrasound imaging is a noninvasive and real-time technique in which involves exposing part of the body to high-frequency sound and receiving echoes from acoustic impedance discontinuities along the propagation path. The contrast arises from the ultrasonic property differentiation of the normal from abnormal tissue or the interface between solid and fluid-filled space. A variety of materials including the aqueous solutions, emulsions and suspensions, which increase the echogenicity (reflection) of blood or specific organs, have been used as the contrast agents. One of the problems of US imaging is the standardization of agents' sizes and stabilities, such as microbubble size.

Nuclear modalities exploit the radioactive decay of nuclides with specific decay properties, which make them useful for in functional/pharmaceutical imaging. Positron emission tomography systems record the gamma rays in opposite direction simultaneously after the annihilation of positrons emitted from isotopes. Many chemicals or proteins labelled with ^{11}C or ^{18}F can image physiological and pharmacological processes rapidly with exquisite sensitivity, potentially quantitative advantage. The using of PET imaging has greatly expanded with the help of glucose analog ^{18}F-fluorodeoxyglucose (FDG), which has the capacity to acquire dynamic profiles, reflecting the ligand delivery, binding and metabolisms [10]. Unlike PET, single photon emission computed tomography does not involve the simultaneous detection of correlated photons. SPECT technique detects single gamma ray photon emission by radiotracers at particular energies and therefore the isotope has relatively longer half-life than PET. Similarly, the design of SPECT imaging molecular reporter probes are typically using ligand labelled to isotopes such as iodine-125, technetium 99m, and thallium 201. In particular, a series of these metals together with fluorescent lipids, and MRI agent incorporation with liposomes enables the drug delivery and *in vivo* diagnostic imaging [11]. However, the expansive radioactive tracer generated by cyclotron or nuclear reactor limits its utility.

Optical imaging has proved a versatile and powerful methodology for scientific investigation throughout modern history. FMT utilize the focused laser light with 360^o scanning position of surface at one or multiple wavelengths and collects excitation photons propagating through the tissue for each focal spot. BLI detects internal luminescence generated by a biochemical reaction during which photons are released. The commonly used agents are firefly luciferin and photinus luciferase. Both

FMT and BLI are highly sensitive (Picomoles) compared with other image modalities, but the accuracy is complicated by highly scattering tissue for *in vivo* applications.

No matter the anatomical or functional imaging modalities, those technologies exploit the interactions between various forms of energy and tissue/samples. All the modalities have intrinsic parameters such as spatial and temporal resolution, acquisition time and sensitivity. As each of the technologies has its own advantages and limitations, an imaging modality that combines the structural and functional information has become a focus of medical research.

Table 1.1 Overview of molecular imaging instruments

Modality	**Spatial Resolution**	**Penetration Depth**	**Time**	**Imaging Agents**	**Sensitivity**	**Cost***
CT	50 μm	No limit	Minutes	Iodine, Gold nanoparticles	μmol	$$
MRI	10-100 μm	No limit	Seconds-minutes	SPIO, Gadolinium	nmol	$$$
US	50 μm	No limit	Minutes	Microbubbles	nmol	$$
PET	1-2 mm	No limit	Minutes	^{18}F,^{11}C	fmol	$$$
SPECT	1-2 mm	No limit	Minutes	^{99m}Tc,^{205}TI	pmol	$$$
BLI	1-2 mm	Centimeters	Seconds-minutes	Luciferins	pmol	$$
FMT	1 mm	<10 cm	Seconds-minutes	NIR fluorochromes	pmol	$$
OA	50 μm	Centimeters	Seconds-minutes	ICG, NIR dye	fmol	$$

* $: <100,000; $$: 100-300,000; $$$: >300,000.

Optoacoustic (or photoacoustic) phenomenon was discovered by Prof. Alexander Graham Bell in 1880. Bell found acoustic waves generation from material absorption of modulated sunlight. Only in recent years, the optoacoustic phenomenon is used for biomedical application due to the technology development. In 1994, Robert Kruger imaged optical absorption in a turbid medium with the optoacoustic effect [12]. In 2003, Wang et al. demonstrated both structure and functional imaging *in*

vivo rat for brain utilizing intrinsic absorber hemoglobin [13]. Optoacoustic imaging is a hybrid imaging modality that synergistically combines the advantages of optical imaging and sonography, offering optical contrast of spatial resolution around 100 μm with sonography imaging depths of multiple millimeters to centimeters and millisecond temporal resolution. As showed in Table 1.1, the OA imaging modality fills the gap in existing imaging modalities with comparable resolution sensitivity but revolutionary performance in temporal resolution, cost effectiveness and abundance of molecular contrast agents, especially suitable for small animal molecular imaging.

1.3 Objectives of this research

This thesis focuses on exploring molecular reporter agent applications for OA imaging. This objective related to requirements *in vivo* OA imaging.

1 Instrument

- What is the relationship between the absorption, fluorescence and OA signal?
- What are the instruments and technologies for quantitative OA signal?
- What are the optimal reconstruction and signal processing approaches for resolving the specific absorber?

2 Contrast agents

- What are the requirements for an OA contrast agent?
- Is it possible to develop a gene reporter with enough sensitivity for OA detection?
- Besides spectrum signature, is it feasible to explore a molecule probe property to increase the signal-to-noise ratio when the high intrinsic absorbers present in the tissue?
- Can exogenous contrast agents in the brain be visualized for functional neuroimaging?

The dissertation is structured along as follows:

- The current chapter introduces the necessary concepts for molecular imaging and contrast agents, a comparison of several current molecular imaging modalities, and the structure of the thesis.

- The second chapter presents several variations of optoacoustic imaging systems found in the literature and used in my current study's experiments. Optoacoustic spectrometer setup, multispectral optoacoustic tomography system and volumetric optoacoustic imaging system were presented. Moreover, the reconstruction algorithms and multispectral unmixing techniques to enhance the detection of molecular probes are introduced.

- The third chapter provides an overview of the contrast agent development. A special focus is given to gene-controlled pathways for OA contrast agent development.

- Chapter 4 proposes a novel method for using synthesis pigment which generates a strong OA signal close to the near-infrared (NIR) range and exhibits high photobleaching resistance, enzymatically amplified, fast and robust OA signal.

- Chapter 5 introduce a switchable reversibly fluorescent protein to generate a high contrast to noise signal, a novel contrast agent that can be differentiated from time-varying background signals.

- Chapter 6 addresses the issue of delivering contrast agents to the brain and across the blood-brain barrier (BBB), which blocks almost molecules to the brain.

- Finally, a brief summary and conclusion of the current study is given in chapter 7.

Chapter 2 Theoretical and technical background of optoacoustic tomography

2.1 Introduction

In this chapter, the physical mechanism of pulsed OA signal generation is briefly described, starting with an introduction of light propagation in biological tissue. The relationship between absorption scattering, fluorescence effects, and OA signal generation is presented. The focus is on the imaging setup, reconstruction approaches and spectral unmixing processing.

2.2 The physics of light propagation in biological tissue

Most biomedical imaging or diagnostics involve electromagnetic interaction with matters. Electromagnetic waves are defined by their wavelengths and frequency. This section focuses on the light and matter interactions in the visible (390-700 nm) and near-infrared (700-900 nm) range. Visible light observed by human corresponds to a frequency range of 400-790 THz.

2.2.1 Absorption and scattering

The interaction of photons with different cellular structures results in scattering and photon absorption, which are associated with a change of photon direction and energy loss. In the low photon energy range (<420 keV), the loss of photon energy is defined by the linear total attenuation coefficient μ. It is composed mainly of two components: $\mu = \mu_a + \mu_s$, μ_α is the attenuation coefficient due to tissue's absorption and μ_s is tissue's scattering. The mean free path (MFP) in tissue is the reverse of absorption μ_s because in most cases the scattering is dominant ($\mu_s \gg \mu_\alpha$). There is approximately a μ_s of 10-100 cm^{-1} and a μ_α of 0.15-0.5 cm^{-1} in biological tissue.

The transport mean free path (TMFP) is used to describe a photon undergoing several scattering processes. As the photon travels to 1 TMFP, the dramatic increase in scattering events eventually randomizes the photon's propagation and leads to photon diffusion. This is determined by the scattering coefficient μ_s', which is expressed as $\mu_s' = \mu_s(1 - g)$. The anisotropy function g describes the degree of forward scattering, which is typically 0.8-1 in biological tissues. A higher g value indicates more forward scattering events and longer penetration distances in tissue. There is a strong drive to study biological processes above 1 TMFP as it is traditionally challenging in optical imaging modality. Generally, confocal microscopy and two-photon microscopy are able to image specimens around 10-20 μm, which operating below the penetration limits below 1 TMFP. As OA imaging

essentially detects US waves induced by photon absorption, it works well in the diffusion regime, which is beyond a 10 TMFP range (typically >1 cm). Therefore, its resolution doesn't tightly depend on the photon scattering in tissue.

2.2.2 Absorption and fluorescence

Generally speaking, a molecule absorbing and emitting photons is called a fluorophore. Molecules solely absorbing photons are called chromophores. The absorption of light and its thermal conversion is a fundamental principle of the OA effect. For fluorophore applications in OA imaging, it is critical to understand the light absorption and emitting process due to light illumination.

The various energy levels involved in the absorption and emission of light can be described by the classical Jablonski energy diagram. In the Figure 2.1, the diagram illustrates the singlet ground (S_0), as well as the first (S_1) and second (S_2) excited singlet states. The transitions between excited singlet states S=>S or triplet state T=>T are called internal conversions. Intersystem crossing is the transition between the excited singlet state and its corresponding triplet state S_0 => T_n. Light absorption occurs by inducing electrons from a single ground electronic level S_0 to S_n (n>1). The molecule is energetically unstable in an excited state and therefore it will return to its ground state S_0 in two steps. Immediately following the absorption, the excited molecules in the state S_n partially dissipates its energy partially in the surrounding environment by reaching the lowest excited state S_1, which is known as internal conversion or vibrational relaxation. In the second step the S_1 electron reaches the ground state S_0 through various pathways. This aspect is of particular interest for molecular imaging. If the relaxation is accompanied by the emission of a photon it is known as fluorescence. However, there are several other competitive processes such as

a) Energy absorption.

b) Energy transfer to nearby molecules.

c) Transitions to an excited energetically unstable triplet state T_1 of lower energy then S_1. During the process from the T state to the ground state, phosphorescence, non-radiative energy dissipation, and energy transfer to another molecule can occur.

Fluorescence is a three-stage event that occurs in fluorophore or fluorescent dyes. Excited by an external photon, a valence electron from ground state S_0 is pushed to an excited singlet state with a higher energy level S_n (n>1). This process is fast and happens in femtoseconds (10^{-15} s). The electron then quickly relaxes to an excited sublevel in picoseconds (10^{-12} s) and the emits of a longer wavelength photon. The molecule returns to ground state occurs in nanoseconds (10^{-9} s). Photon absorption occurs within a time frame of 10^{-15} s and the lifetime of fluorescence is from 10^{-9} to 10^{-12} s.

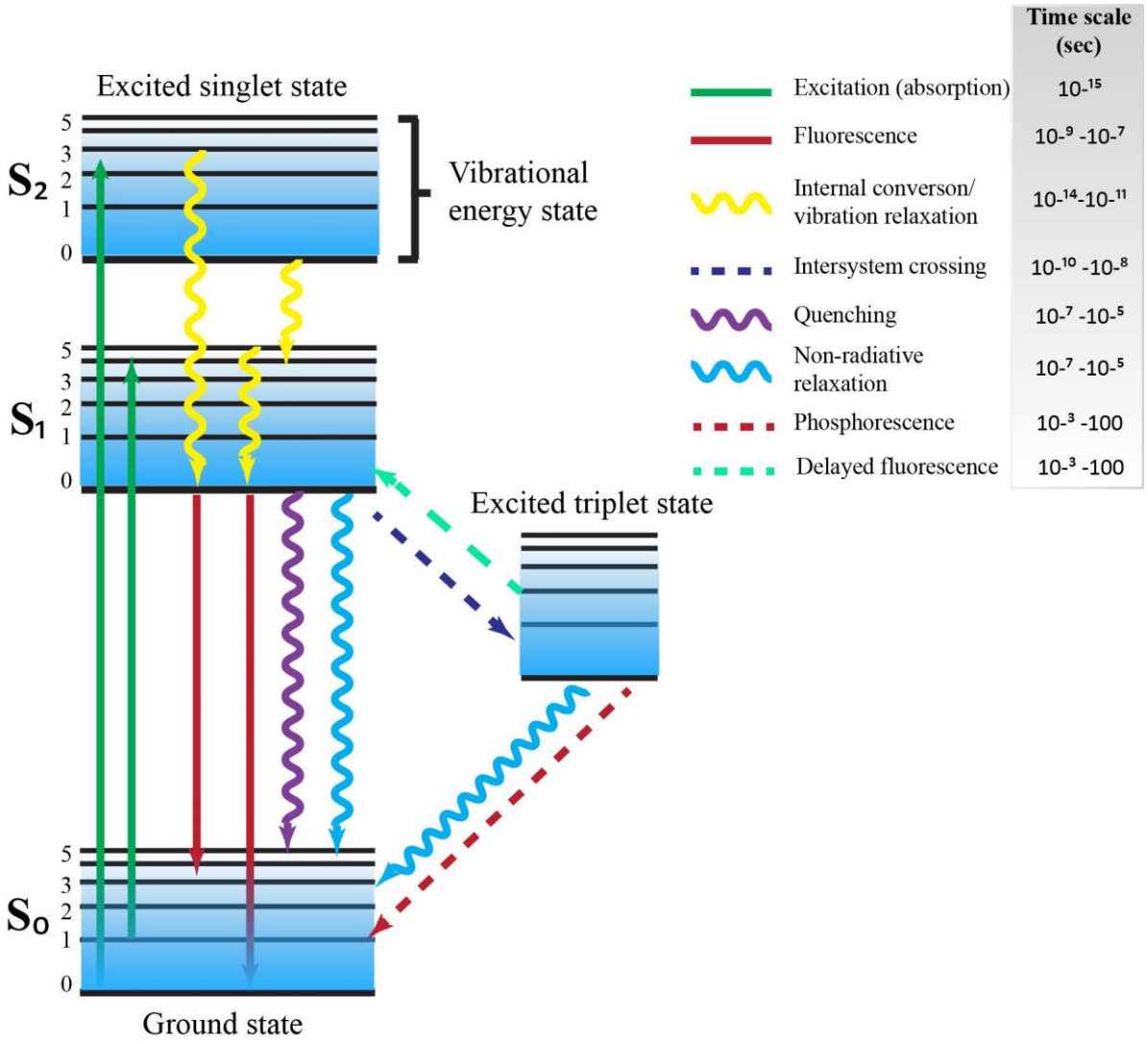

Figure 2.1: The Jablonski Diagram. An electron that leaves the ground state (electronic singlet, S_0) to higher excited state (S_n, $n \geq 1$,) when a single photon is absorbed. It relaxes quickly to lower vibrational state (orange line) and loses energy. When returning to the ground state, it dissipates its remaining energy by emitting a photon with a longer wavelength, *i.e.*, fluorescence emission. Intersystem crossing can occur during the transition of an excited energetically unstable triplet state T_1 of lower energy then S_1. During the process from T state to ground state, phosphorescence, non-radiative energy dissipation, and energy transfer to another molecule can occur. Notice that all events occur on several orders of magnitude of timescale (insert).

2.2.3 Absorption spectrum

The absorption spectrum is one of the key characteristics for the OA contrast agents as their tight dependence on it. An absorption spectrum is the result of electronic, vibrational, and rotational

transitions. The maximum peak of a spectrum corresponds to the electronic transition line. Rotational and vibrational transitions form the rest of the spectrum. Hence, the absorption spectrum profile depends extensively on the relative position of these vibrational states. Local increase in temperature enhances the rotational and vibrational states of molecules, which causes the broadening of spectrum. Therefore, absorption spectrum is sensitive to temperature. Likewise, the emission spectrum of the fluorophore is often the mirror image of the absorption spectrum because the emission of a photon often leaves a fluorophore in a higher vibrational ground state. In general, most of fluorescent effects occur when the excitation is in the ultraviolent or violet spectrum, out of the illumination source spectrum used in most OA systems.

2.3 Optoacoustic signal generation

Upon illumination with pulses light, the absorption of photons by the molecules generates a local rise in temperature. This thermal expansion generates acoustic wave that propagate through the medium and can be detected by an acoustic transducer. To avoid heat conduction, a short enough laser pulse, within the duration of a nanosecond, ensures thermal confinement. The energy $h(\vec{\boldsymbol{r}})$ absorbed per volume during a pulse of length τ can be defined as :

$$h(\vec{\boldsymbol{r}}) = \int_0^{\tau} \mu_a\,(\vec{\boldsymbol{r}})\Phi(\vec{\boldsymbol{r}}, t)dt = \mu_a(\vec{\boldsymbol{r}})\Phi \tag{2.1}$$

where $\Phi(\vec{\boldsymbol{r}}, t)$is fluence rate $(Js^{-1}m^{-2})$ and $\Phi(\vec{\boldsymbol{r}})$ is the fluence (Jm^{-2}) at a given point $\vec{\boldsymbol{r}}$ in space. The local temperature rise is

$$\Delta T = \frac{h}{\rho C_v} \tag{2.2}$$

where h is the deposited energy, and ρ is the density of constant volume with heat capacity of C_v. The acoustic pressure induced by the increase in temperature can be given by

$$\Delta \mathrm{p} = \frac{\beta \Delta T}{K_T} \tag{2.3}$$

where β is the isobaric volume thermal expansion coefficient ($\sim 4 \times 10^{-4} K^{-1}$ for muscle) and K_T is the compressibility. By substituting this with equation 2.2, it can be expressed as

$$\Delta \mathrm{p} = \frac{\beta \mathrm{h}}{K_T \rho C_v}. \tag{2.4}$$

Absorber's thermodynamic properties can be defined the with the constant as a Grüneisen coefficient $\Gamma = \frac{\beta}{K_T \rho C_v}$, leading to

$$\Delta \mathrm{p} = \Gamma \mathrm{h}. \tag{2.5}$$

From equation 2.1, the following equation can be obtained

$$\Delta \mathrm{p} = \Gamma \mu_a(\vec{\boldsymbol{r}}) \Phi(\vec{\boldsymbol{r}}). \tag{2.6}$$

Therefore, the local acoustic pressure is determined by local light fluence and optical absorption properties at a given point. With knowledge of light fluence information and the help of transducers to detect the acoustic waves propagation through a medium, we can then quantify the optical distribution of the sample through optoacoustic image reconstruction:

$$\frac{\partial^2 \mathrm{p}(\vec{\boldsymbol{r}}, \mathrm{t})}{\partial t^2} - c^2 \nabla^2 \mathrm{p}(\vec{\boldsymbol{r}}, t) = \Gamma \frac{\partial^2 \mathrm{H}(\vec{\boldsymbol{r}}, t)}{\partial t}. \tag{2.7}$$

Again, when the duration of the laser pulse is in the order of a few nanoseconds, the rise in temperature can be assured instantaneously, separated as $\mathrm{H}(\vec{\boldsymbol{r}}, t) = \mathrm{H}(\vec{\boldsymbol{r}})\mathrm{H}(t)$. Thus $\mathrm{H}(t)$ can be represented with a Dirac-delta function, $\mathrm{H}(t) \approx \delta(t)$. The propagation of acoustic waves in the medial can be described in terms of time domain. Assuming the acoustic pressure generated at $\vec{\boldsymbol{r}}$ point at given time t after excitation of object Ω, the solution can be further derived by Green's function:

$$\mathrm{p}(\vec{\boldsymbol{r}}, \mathrm{t}) = \frac{\Gamma}{4\pi c^2} \left[\int_{\Omega} \mathrm{H}(\vec{\boldsymbol{r}}') \frac{\delta\left(t - \frac{|\vec{\boldsymbol{r}} - \vec{\boldsymbol{r}}_0|}{c}\right)}{|\vec{\boldsymbol{r}} - \vec{\boldsymbol{r}}_0|} d\vec{\boldsymbol{r}} \right]. \tag{2.8}$$

Equation (2.8) describes the OA detection as a sum of acoustic waves arriving from different points $\vec{\boldsymbol{r}}_0$ of the object Ω, weighted and delayed by a factor dependent on the relative geometry of the detector and object.

The induced temperature, followed by thermal expansion, produces stress that propagates through the sample and then is detected by transducer. The amplitude of the OA signal is proportional to the absorbed energy from laser pulses. In general, the typical time domain of an OA signal is an N-shape bipolar signal due to the fact that only half of the disturbance starts to propagate outwards and the other half propagate inwards from the spherical or cylindrical source [14].

2.4 Optoacoustic imaging instrument

2.4.1 Introduction

Contrast agent development and delivery are heavily related to the implemented instrument. The following section introduces several versions of OA imaging systems that can be found in the literature and are used in the current study's experiment. Optoacoustic spectrometer setup shows the raw OA signal detected by US transducers and the capability to efficiently test contrast agents. Multispectral optoacoustic tomography system offers high-resolution and deep penetration for *in vivo* imaging. Volumetric optoacoustic imaging system provides fast, real-time, three-dimensional tomography images. Furthermore, reconstruction algorithms and multispectral processing techniques to enhance the detection of molecular probes are examined.

2.4.2 Optoacoustic spectrometer

The OA spectrometer is a promising analytical tool to identify contrast agents for which absorbers generate OA signals. Strictly speaking, it is not an imaging device but it can quickly detect OA signaling from fluorescent proteins (FPs), nanoparticles, cells, and dyes. Compared to expansive tomography systems and elegant OA microcopy system, OA spectrometers are much easier to handle, cheaper to build, and less time consuming in performance. They are especially suitable for screening and characterization of the properties of contrast agent for *ex vivo*/ *in vivo* applications. They also show tremendous potential for high sensitivity detection of single circulating tumor cells, red blood cells, and the study of pharmacokinetics for contrast agents. Using this tool, the real-time detection of circulating red and white blood cells, bacteria, and gold nanoparticles are feasible [15]. A continuous flow of samples allows for the assessment of large volume circulating in the sample holder for *in vivo* and *ex vivo* applications.

This chapter introduces the OA spectrometer used for the optimal OA contrast agent screening. Laser pulses directly illuminate these chromophores. The generated OA signal through absorbing energy can easily be measured with a cylindrically focused transducer. In particular, the system is used to measure the fundamental optoacoustic effects related to wavelength, time-resolved, and concentration dependence. These quantitative measurements are thus useful for further studying of optical absorption/scattering characteristics in the tissue.

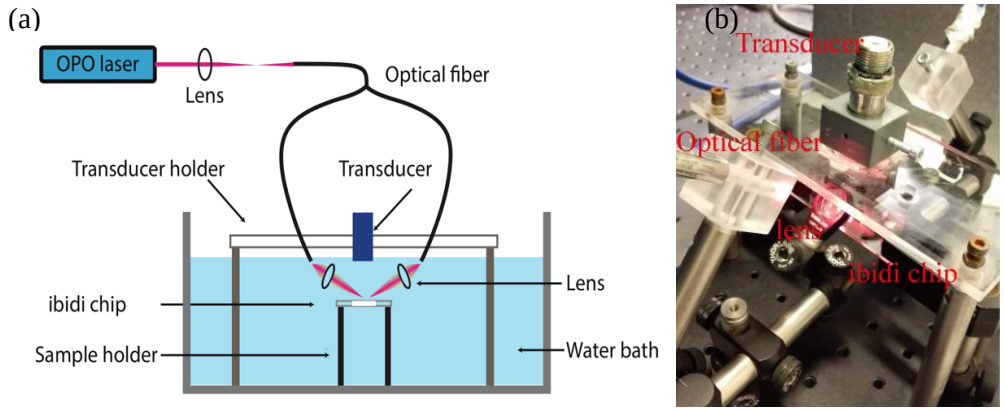

Figure 2.2: Optoacoustic (OA) spectrometer scheme and setup. (a) OA spectrometer scheme, two arm fibers illuminate to the ibidi chip center. (b) Picture of OA spectrometer setup.

To find a chamber suitable for cell flow, cell cultures, and laminar exchanges, a OA spectrometer system is built based on a µ-Slide ibidi chip, which is suitable for cell culture and adherent cells under defined shear stress and shear rate levels (Figure 2.2). The chip channel can connect with Luer adapters and pumps to control injection speed, offering various potentials for cell, protein, and contrast agent testing. For example, the laminar flow characteristic can be used for defined medium or buffer exchange, drug delivery, Ca^{2+} imaging, and living staining. The continuous laminar can be used for blood cells to mimic shear stress conditions in micro capillary, venous, and arterial flow, among others. On the other hand, the flow chip has a high optical quality so the background signal can be minimal due to the extremely low birefringence.

The acoustically coupled flow chip (µ-Slide I 0.2 Luer, hydrophobic, uncoated, ibidi, Munich, Germany), and its OA signals are detected using a single-element transducer (V382-SU, 3.5 MHz, Olympus, Hamburg, Germany). The sample is illuminated from two sides via fiberoptic light guides (Figure 3.1 a) coupled with pulsed laser source delivering pulses of a 10 ns duration with a pulse repetition rate of 50 Hz (SpitLight, Innolas, Krailling, Germany). A third fiber output is used to measure the laser intensity as a function of wavelength with a laser powermeter (FieldMaxII-TOP, Coherent Inc. Santa Clara, USA) to correct for pulse-to-pulse energy variations. Optoacoustic signals are recorded with a digitizer (NI USB-5133, National Instruments, Austin, Texas, USA), connected to a standard computer as a function of laser wavelength.

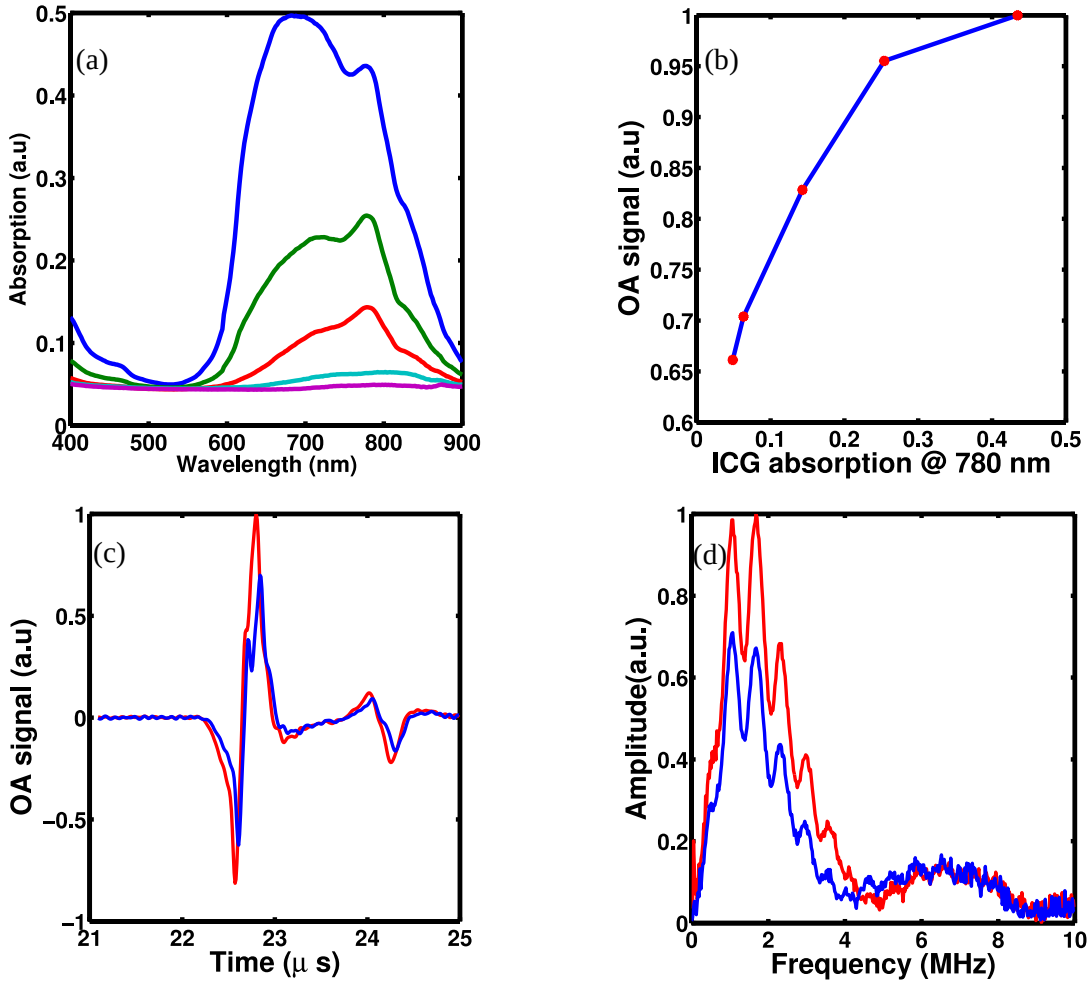

Figure 2.3: Indocyanine green (ICG) concentration and OA signal measurements. (a) ICG absorption of the diluted series. (b) Linear agreement between the absorption measured at 780 nm and their corresponding OA signal. (c) Selected OA signal of the highest concentration (blue) and the four-fold diluted concentration (red). (d) Corresponding frequency spectrum of the (c).

Indocyanine green (ICG) is a common organic dye for OA measurements due to its well-studied fluorescence and OA properties. With an ibidi microscopy chamber (μ-Slide I 0.2 Luer uncoated microscopy chamber), we first tested the dilution series of ICG. The ICG obtained from aliquot (5 mg/ml, 129nM, Pulsion Medical Systems, Germany) with 10 μL with 2 mL DPBS was used as the first sample. Absorption measured absorption spectrum from each solution used was recorded on a spectrometer (OceanOptics CUV-UV + USB2000) and processed with SpectraSuite (OceanOptics, Ostfildern, Germany). The ICG sample was diluted 4 times (50% v/v with DPBS) to obtain the optical from 0.43 to optical density of 0.05 at 780 nm for the last sample in Figure 2.3 (a). The typical time domain of OA signal of the undiluted (blue) and samples diluted 4 times (red) shown in Figure 2.3 (c) and the corresponding frequency domain spectra of the signal are shown in Figure 2.3 (d). The OA

measurement shows linear agreement between the absorption (780 nm) was shown in Figure 2.3 (b). Therefore, this OA spectrometer is used for the contrast agent characteristic study to explore the wavelength and temporal/frequency information of the contrast agent. More details and examples are provided in the following chapter.

Further applications of the OA spectrometer may be largely unexplored, such as the optoacoustic flow cytometer. This can be examined in terms of several prospects:

a) In terms of laser excitation, the OA spectrometer is the most convenient method for laser parameter verification. The OA signal is sensitive to the laser fluence, laser pulse width, laser pulse rate, laser beam diameters, and wavelengths selected. With this cost-efficiently design, laser system such as optic mirror, filters, and illumination console control can be easily adapted based on the chromophores' spectra.

b) The modeling of acoustic detectors is relatively simple. Sensitivity modeling parameters such as transducer geometry, frequency, wideband, and US angular acceptance for conventional focus piezoelectric detectors can be directly modeled into this configuration. Other types of sensor, based on optical resonators and interferometry such as Fabry-Perot interferometers [16], or fiber Brag grating [17] can simply be mounted in the system.

c) For more specific contrast agent cellular characteristic studies, the system is particular effective for tracking the growth of cells/bacteria directly in the ibidi chip. The flow channel facilitates the study of adherent cells under flow conditions such as media buffer exchange, defined flow patterns and temperature control. Moreover, the setup can be readily applied to the quantitative determination of chromophore concentration [18].

2.4.3 Multispectral optoacoustic tomography

As shown from the OA spectrometer, the detection of the focused transducer directly represents the distribution of the optical absorber along the focus point. This method is limited to detecting biomarkers through several millimeters to centimeters of tissue due to tissue scattering. For *in vivo* application, intrinsic tissue absorber such as hemoglobin and melanin will generate background signals, which are complicated to identify with biomarkers via only single wavelength. To address this issue, a multispectral optoacoustic tomography (MSOT) system was developed which offers high-resolution three-dimensional images by acquiring two or three- dimensional OA signals along multiple projections of objects.

To obtain 2D or 3D images, the detector needs to scan along the object or use a transducer array instead. The detection along the line (A-scan) typically is time consuming (minutes to hours) due to scanning around the sample with a single transducer [13][19]. Therefore, a scanning arrangement based on the transducer array is more efficient for obtaining high quality images. To achieve this, a dedicated laser illumination pattern, US scanner geometry, and parallel data acquisition have been implemented. To obtain whole body in real-time optoacoustic visualization, the technique and practical aspects including stepper motor scanner, acoustic coupling medium, animal physiology control, and anesthesia supply also need to be applied.

In the all the experiments of two-dimensional MSOT images were acquired by the latest version with 256 elements MSOT system with following configuration. The illumination and detector geometry of MSOT system are shown in Figure 2.4. The excitation light in NIR range of MSOT system (680-950 nm) is provided by a tunable optical parametric oscillator (OPO) laser system (Innolas laser GmbH, Krailling, Germany). The laser pulse duration is below 10 ns and pulse repetition frequency is 10 Hz. The maximal pulse energy delivered by the OPO laser is $\sim 20\ \mathrm{mJ/cm^2}$ at 740 nm, fulfilling the maximal permissible exposure of laser safety standard [20]. The pulsed beam is guided into a silica fused-end fiber bundle (CreamOptic Industries, Inc. East Longmeadow, MA) that is divided into 10 output arms. This arrangement creates a ring-shaped illumination pattern of ~ 7 mm width on the surface of the animal, coinciding with the ultrasound detection plane. A cylindrically focused piezocomposite 256-elments transducer array (Imasonic SaS, Voragy, France) with a center frequency of 5 MHz offers a 270^{o} cross-section plane coverage around the sample. The detected signals by the transducer array are digitize with custom-made data-acquisition system (Falkenstein Microsystem GmbH, Taufkirchen, Germany) at a sampling rate of 40 mega samples/s. For *in vivo* imaging, mice/samples are wrapped in thin polyethylene membrane and submerged in water tank for acoustic coupling. The linear stage (IAI Industrieroboter GmbH, Schwalback, Germany) with animal holder can be translated with minimum 0.1 mm step to enable imaging of multiple transverse planes.

To summarize, the real-time multispectral optoacoustic tomography whole body imaging system has following major improvements [21][22]:

(a) Multiwavelength and selective-plane illumination

(b) Multi-element ultrasound array for large volume coverage with reasonable frequency

(c) Multi-channel data acquisition with high sampling rates

(d) Model-based reconstruction and multispectral unmixing processing

(e) Linear translation stage and water impermeable animal holder

There are several versions of the MSOT setup through the engineering of the current institute and iThera (iThera Medical GmbH, Kreiling, Germany). The most substantial improvements of these systems are the scanning and detectors. The detection started from single US detector [23], to 64-element curved transducer array [21], to 128, and 256 channels to achieve high resolution and fast real-time imaging. The field of view for tomographic imaging objects evolved from two sides to 172^{o} and to 270^{o} coverage. More details are described in elsewhere [24][25][26].

By varying wavelengths, the unique spectrum signature of a contrast agent of interest can be explored to differentiate targets in tissue. This can be done through the direct subtraction of the images obtained at two wavelengths, with one wavelength close to the tissue absorption and the other one corresponding to the peak of the biomarker, thus its effects canceling out the background contribution. Sophisticated unmixing methods based on the differential of fitting with in prior spectral information can improve sensitivity, especially when the contributions of various absorbers may constitute only small variances over the background. Multispectral technique extends the capabilities of MSOT as the chromophroic molecules distribution in the tissue can be identified with their corresponding wavelengths.

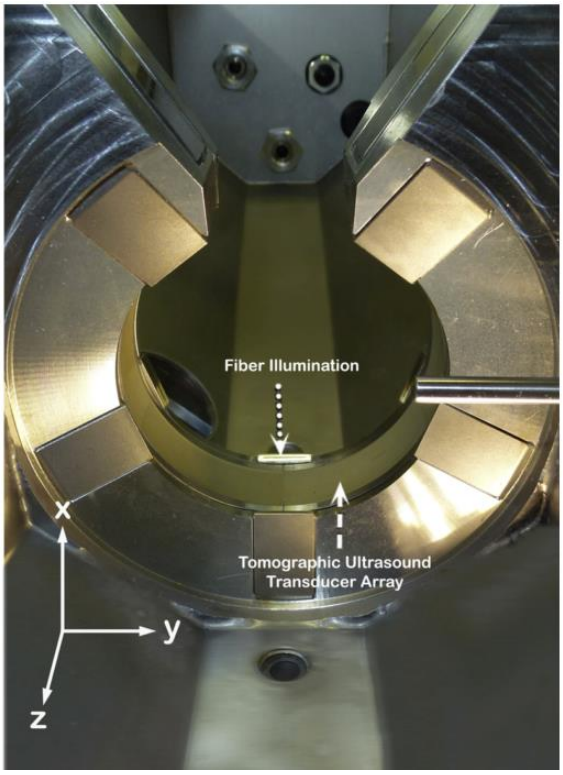

Figure 2.4:Illumination and detection geometry of multispectral optoacoustic tomography (MSOT) system and animal holder.

2.4.4 Volumetric real-time optoacoustic imaging system

As described, the MSOT system offers a revolutionary performance for small animal imaging with high resolution and sensitivity, scalability, and cost effectiveness. The advantages and disadvantages of MSOT system, however, are derived from the imaging configuration while scanning (rotating) a set of transducers around the image object of interest to acquire tomographic OA signal. First, the cross-sectional illumination is still inefficient and provides only restricted angular coverage (even 270°) because of the limitation of detection geometries. Thereby, the scanning OA image system is not adequate for some fast or clinical applications. In many imaging scenarios, such as the imaging of large areas of human breast or skin, tomographic access to the imaged area from all directions is not feasible. Second, the two-dimensional representation is generally inaccurate due to fact that inherent OA signal waves which actually propagate in three dimensions rather than two dimensions. Moreover, significant motion artifacts are introduced when the detection array scanning with velocity exceeds several mm/s. More recent volumetric OA imaging system employed no scanning has been proposed based on incorporating an illumination fibers into ultrasound linear arrays [27][28]. X. Luís et al. developed a novel hand-held imaging probe for a real-time volumetric OA imaging system incorporates an annular two-dimensional array of ultrasonic sensors densely distributed on a spherical surface[29] [30].

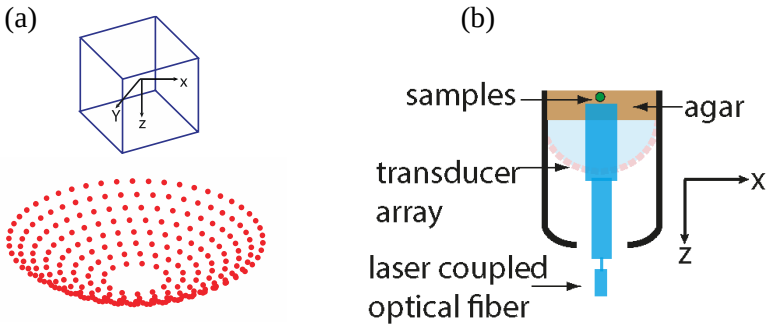

Figure 2.5: Scheme of volumetric optoacoustic tomography imaging system. (a) Side view of distribution of the 256 transducer piezoelectric elements (red points). The cube represents the region of interest. (b) The experimental system for measuring an *in vitro* sample.

The geometry of the custom-made three-dimensional probe (Imasonic SaS, Voray, France) consists of 256 US elements (Figure 2.5 a). The piezocomposite transducer array is used to collect the OA signals in the center of the sphere. This configuration maximizes the signal-to-noise ratio (SNR), as all the densely distributed elements are highly sensitive to the center region. The active detection aperture has a 8 mm diameter circular opening in the center such that a fiber bundle (CeramOptics GmbH, Bonn, Germany) can be inserted for optical illumination. A short-pulsed wavelength-tunable laser with a

pulse repetition rate of 50 Hz (Innolas Laser GmbH, Krailling, Germany) can be used as a light source. For acoustic coupling, the system utilizes a transparent membrane thus avoiding direct contact between the imaged object and the coupling medium. The configuration of the laser beam and three-dimensional probe with a sample on the top of agar is shown in Figure 2.5 b.

The breakthrough capacity of such volumetric visualization in real-time has shown promising application high-frame rate analysis of cardiovascular dynamics and mouse heart [31] and functional neuroimaging with cerebral hemodynamic visualization [32]. The combination of real-time, three-dimensional tomography and powerful multispectral data enrich information for time-resolved and spectrally unmixing of biomarkers in the OA applications. This volumetric system is also used for fast 3D volumetric imaging, as presented in the chapter 4 and chapter 5.

2.5 Optoacoustic image reconstruction

The goal of the OA imaging modality is to provide a quantitative, spatial distribution visualization of absorbers within an optically scattering medium such as biological tissue. As shown in equation 2.6, the OA signal is proportional to the absorption and local optical fluence. $\Delta p = \Gamma \mu_a(\vec{r})\Phi(\vec{r})$. Therefore, the image reconstruction requires solving the inverse problem to find the optical property $\mu_a(\vec{r})$ (or energy absorption in the region) with a set of detected OA signals p and with assumed light influence Φ at a given position $\vec{r}$.

A wide variety of algorithms have been introduced to recover the mapping of optical absorptions [33][34]. These reconstruction methods fall into two main approaches: analytical and algebraic. Analytical inversion often does not accurately account for the geometry of the detector using approximate formulas derived from computer tomography algorithms such as Radon-like back projection. Such algorithms are employed for their simplicity and low computational cost. Closed-form analytic back projection can be applied in time or frequency domains [35][36]. Algebraic approaches solve the forward problem as sum of all linear effects that generate the OA signals. Ultrasonic transducer properties such as impulse response, spatially dependent sensitivity, geometry, the nonuniform illumination, and speed of sound are included in the model matrix. Then the direct or iterative reconstructions are performed by inverting the model matrix and minimizing the error between the calculated theoretical image and the measured data [37][38].

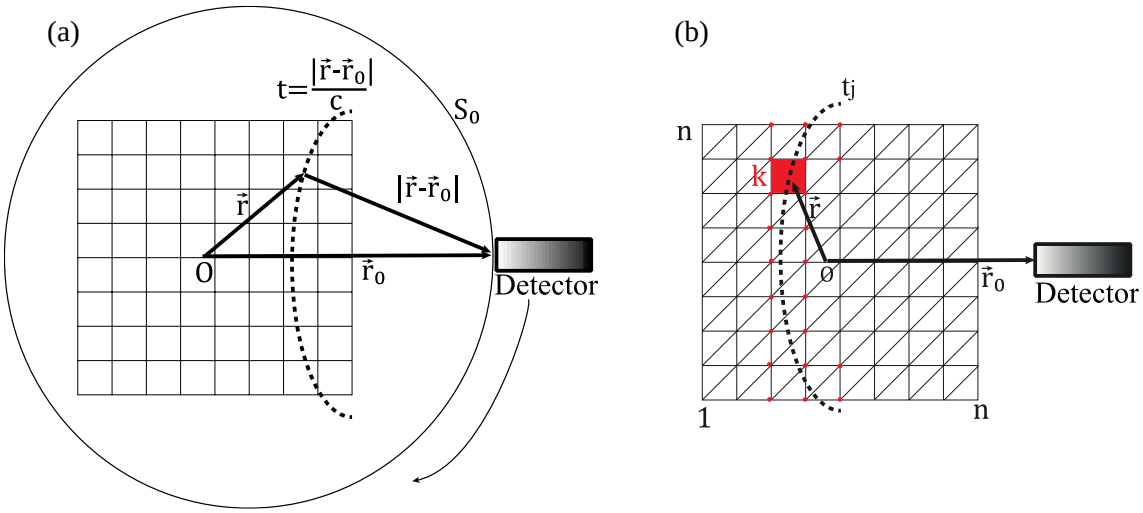

Figure 2.6: (a) Geometry scheme for the back projection algorithm. (b) Geometry of model-based model. Red grid points are involved for interpolation of discretized curve and the given source voxel $\vec{\boldsymbol{r}}_k$ is highlighted.

2.5.1 Back projection

Back projection algorithms are commonly used for real-time visualization due to their simplicity and fast computation time. Image reconstructions ared based on beam forming equation or derived analytical formulas. Xu et al. described the universal back-projection based inversion schemes in 2005 [35]. Derived from the equation 2.8, back projection algorithm reconstructions sum signals onto a grid, mapping the time resolved signals form the detectors.

$$P(\vec{\boldsymbol{r}}) = \int_{\Omega_0} \frac{d\Omega_0}{\Omega_0} \left[2P(\vec{\boldsymbol{r}}_0, \mathrm{t}) - 2t \frac{\partial P(\vec{\boldsymbol{r}}_0, \mathrm{t})}{\partial t} \right]\Big|_{t=|\vec{\boldsymbol{r}}-\vec{\boldsymbol{r}}_0|}, \qquad 2.9$$

where Ω_0 is a solid angle of the whole detection surface S_0 (Figure 2.6, a), typically assumed to be a sphere ($\Omega_0 = 2\pi$). The term $\frac{d\Omega_0}{\Omega_0}$ represents an effective angle weighting to the detection element $\mathrm{d}\Omega_0$, which is determined by the angular position of the sensor and the number of projection.

$$d\Omega_0 = \frac{dS_0}{|\vec{\boldsymbol{r}}-\vec{\boldsymbol{r}}_0|^2} \frac{\widehat{\boldsymbol{n}'}^2(\vec{\boldsymbol{r}}-\vec{\boldsymbol{r}}_0)}{|\vec{\boldsymbol{r}}-\vec{\boldsymbol{r}}_0|}, \qquad 2.10$$

where $\widehat{\boldsymbol{n}'}$ is the normal vector of pointing to the origin.

Equation 2.9 can be interpreted as the back-projection term (expressed in the brackets) is being projected backward on a spherical surface with respect to position $\vec{\boldsymbol{r}}_0$. For each sensor position $\vec{\boldsymbol{r}}_0$, the pixels that are located at a distance $|\vec{\boldsymbol{r}} - \vec{\boldsymbol{r}}_0|$ are assigned to the same the value that corresponds to the

signal measured at $t = \frac{|\vec{r}-\vec{r}_0|}{c}$ minus its derivatives. This is because the detector integrates all contributions from sources that are located on the surface with radius $R = c \cdot t = |\vec{r} - \vec{r}_0|$. The reconstruction is then implemented by sequentially computing the back-projection term and multiplied with the respective weighted factor $\frac{d\Omega_0}{\Omega_0}$.

The back projection algorithm is normally applied for real-time structural display due to the fast performance and approximation of absorbing objects. Because the back projection only considers the time derivative term, the reconstructed images typically have enhanced boundaries and the accentuation of small details such as the low frequency information about the signal is not included. The disadvantage of back projection based on delay-and-sum algorithm is its quantification inaccuracy, which making them inappropriate for quantitative functional or molecular imaging applications.

2.5.2 Model-based inversion

A model-based 2D OA image reconstruction strategy was introduced by Rosenthal et al. in 2010 [38]. The model is based on an analytical solution obtained for a 2D linear detector. The model-based approach based on calibrated system, that is the calculated temporal response of a detector for every pixel in the grid is incorporated in the forward matrix of the setup.

The model is expressed with linear pressure rays as combination of absorbers, in a way that the only effect of the space-dependent speed of sound in time-shift of the optoacoustic signals. Thereby, the integration curve along which the pressure integral is computed needs to be modified

$$P = MH, \tag{2.11}$$

P is a row-vector representing the discretized optoacoustic signals measured by detectors located at different positions $\boldsymbol{r}$ within the region of interest (ROI). *M* is the forward model matrix and *H* is the column vector corresponding to unknown optical absorption on the points of the grid.

To find an analytical solution of the integral of the equation (2.8), model-based approach deal with discrete grid $H_{\vec{r}}(\vec{r}_k)$ at grid coordinate $\vec{r}_k$ (Figure 2.6 b). Measuring instant time t_j, the detect sensor at position $\vec{r}_0$ and given source voxel $\vec{r}_k$, the matrix elements pressure can be expressed as

$$P(\vec{r}_0, t_j) = \sum_k^n M_k(\vec{r}_0, t_j) H_{\vec{r}}(\vec{r}_k), \tag{2.12}$$

where $N = n^2$ is the total number of pixels predetermined for image reconstruction. The function of $M_k(\vec{r}_0, t_j)$ is determined by the type interpolation employed. The red grid points (Figure 2.6 b) are used to calculate the integral of the representing arc of time t_j. Several types of appropriate interpolation functions such as linear, right angle triangles, and angular discretization demonstrate high performance in terms of spatial resolution, reduced artifacts, tand hree dimensional imaging capacity without substantially increasing complexity [37][38][39].

For a given OA imaging system, M depends solely upon geometry of the setup and speed of sound in the medium. Therefore, the forward model is expressed with a linear operator that maps the optical absorption in a grid containing the sample to the resulting integrated wavefield at the detection position. Minimizing the mean square difference between the theoretical pressure (calculated via the model matrix) and the actually detected pressure P_m provides the reconstruction, i.e.,

$$H_{sol} = \underset{H}{argmin} \|P_m - MH\|^2, \tag{2.13}$$

where $\|\cdot\|$ is l_2 norm. The inversion solution can be performed through iterative methods such as Moore-Penrose pseudo-inverse M^+ [40] or the LSQR algorithm [38]. Although the calculation of the pseudo inverse may be burdensome for CPU and memory, it only needs onetime calculation for a given system. Then, the reconstruction can be simplified by fast matrix-vector multiplication of stored model:

$$H_{sol} = M^+ P_m. \tag{2.14}$$

Alternatively, the LSQR algorithm allows fast reconstruction by extracting the sparsity of the model matrix. The sparsity of the model matrix only involves a multiplication of the matrix and its transpose M^T in each iteration.

In principle, the regularization is optional for full-view scenarios (i.e., the signal being acquired along 360° around the imaged sample), as the number of projections it provides is high enough. But in experimental conditions it is not always practical because the samples have to be fully immersed in water for efficient acoustic coupling and the accessible detection. For a limited-view tomographic system, it is convenient to regularize the inversion procedure. In such a case, the reconstruction can be further performed through minimizing:

$$H_{sol} = \underset{H}{argmin} \|P_m - MH\|^2 + \lambda^2 \|LH\|^2. \tag{2.15}$$

The added regularization term is used to suppress ripples in the direction of the artifacts [41]. λ is the regularization parameter ($\lambda > 0$) and matrix L is the regularization operator for spatial filtering or smoothness. Tikhonov or total variation regularization can be implemented. Regularization can reduce reconstruction errors arising from the model-based approach but also reduces accuracy or computational efficiency.

As described, the image formation model-based approach works by minimizing the difference between the measured signals and the theoretical signals. The algorithm models the forward OA propagation either in the time, frequency [42], or wavelet domain [43]. Several iterative inversion schemes, regularizations, and compressed sensing approaches can be further adapted to reduce the artifacts and distortion, therefore improve the image quality. The advantage of a model-based approach is the ability to account for all linear effects and imperfection s of the setup in the model, such as the electrical impulse responses, spatially dependent sensitivity fields of the transducer, and the speed of sound precision. Therefore, it offers improved reconstruction accuracy and flexibility for experimental conditions. However, model-based algorithms require longer calculation times or considerable consumption of memory to store the model. The computation and storage of a full model operator (typically in matrix form) are quite demanding.

2.6 Multispectral processing and unmixing

2.6.1 Introduction

One of the key breakthroughs of the MSOT system is its capacity to make use of spectra signatures of absorbers, for example intrinsic tissue chromophores and administered extrinsic contrast agent. Instead of single wavelength excitation measurement of the biological tissue within a few centimeters, the MSOT system capable of reconstructing a high-resolution mapping of distinct absorber by recording images at multiple wavelengths.

In the simplest case, the distribution of the absorber within a biological tissue can be obtained by direct illumination at the wavelength of peak absorption. This is only true in practice if the absorption of a substance of interest is much higher than the tissue background absorption [44]. However, in many cases, the signal contribution of contrast agents may only constitute small variances over the background. Even the mCherry expression of a relatively transparent zebrafish or the enhanced green fluorescent protein (eGFP) distribution in the small-scale Drosophila is barely visible [19]. Generally speaking, most of the genetically expressed FPs are not preferable for OA imaging in mammalian tissues. This is because of their limited concentration (administration or expressed), low extinction

coefficients, and the insufficient OA signal generation at red-shifted absorption beyond 650 nm to avoid the high absorption from hemoglobin. However, these limitations can be addressed through spectral unmixing method, which improve the contrast and sensitivity by resolving the spectra signature, especially for FPs with relatively narrow spectra window and steep declines from the adjacent absorption peak.

A spectral unmixing processing is an approach to convert the images from multiple wavelength illuminations to a new set of images with the biodistribution of a specific absorber of interest. The resulting images indicate the functional and molecular tissues features, which can be correlated or overlap with anatomical structures by averaging the images of the background absorption. For quantitative representation of contrast agent distribution within tissue, generating images at several wavelengths can substantially increase detection sensitivity. Spectral unmixing is therefore used to recover the biodistribution of specific chromophores with improved sensitivity and selectivity. Even if the exact spectral profile of background *in vivo* imaging is not always known, the main spectral components due to the background absorber (oxygenated and deoxygenated hemoglobin), can used in direct spectra inversion [45].

The simplest spectral unmixing method is directly calculating the difference of images taken peak and background absorption of the substance of interest. This separation is not accurate in terms of sensitivity. With known spectral or temporal information, unmixing methods are based on differential or fitting algorithms to process images on a pixel-by-pixel basis. Spectral unmixing can be processed by differential of fitting algorithms are described in the following section.

2.6.2 Linear spectra fitting

The most common unmixing method is spectral fitting which tries to find the spectra component that best fits its known absorption spectrum in the least squares minimization. Given the multispectral measurement matrix M $(n \times m)$, where n is the number of image pixels and m is the number of measurements, and assuming measured data at position $\vec{\boldsymbol{r}}$ at given laser wavelength λ_i , then

$$M(\vec{\boldsymbol{r}}, \lambda_i) = \sum_{j=1}^{k} U(\vec{\boldsymbol{r}}, \lambda_i)\varepsilon_j(\lambda_i)C_j(\vec{\boldsymbol{r}}), \qquad 2.16$$

where $i = 1,2, \dots, m$ and m are the total number of measurement wavelengths. $U(\vec{\boldsymbol{r}}, \lambda_i)$ represents the spatially varying function of optical fluence with respect to wavelength, and $\varepsilon_j(\lambda_i)$ and $C_j(\lambda_i)$ are the wavelength-dependent molar extinction coefficient for j-th absorber and its spatial distribution (concentration) respectively. Defines spectra matrix S $(k \times m)$ with the absorption coefficient of the k components at the m measurement wavelengths. Spectral signature of the absorbing component j

$$S_j(\lambda_i) = \frac{\varepsilon_j(\lambda_i)}{\|\varepsilon_j\|_\infty}. \quad 2.17$$

Then the spectra matrix can be unmixed with the Moore-Penrose pseudoinverse S^+ [40]

$$S^+ = S^T(SS^T)^{-1}. \quad 2.18$$

The best fits spectra in S can be derived from the generalized inverse S^+. The d spatial distribution from source component reconstruction can be unmixed via:

$$R_{pinv} = MS^+, \quad 2.19$$

However, the separation of this spectral fitting method may be challenging because the accuracy and completeness of the absorption spectra of the agent of interest may not be available, for instance the absorption may change in biological environments during *in vivo* imaging scenario. In addition, the actual resulting images show a nonlinear relationship between the measured signals and the corresponding target concentration, which induced by light fluence attenuation and US speed variation as a function of depth or target size in the tissue [46]. Moreover, the background contributions and systematic error are not always known.

2.6.3 Principal component analysis

Principal Component Analysis (PCA) is a well-known statistical procedure for blind source separation [47]. It is based on the assumption that a set of observations or measurements of possibly correlated variables can be transformed into a new set of values of linearly uncorrelated variables. The resulting of orthogonal transformation from a covariance matrix is called the principal components, in which the linear combination of the variables with maximum variance is projected as the first principal component, that the largest accounts for remaining variance is projected onto the second components and so on. PCA can simply calculated from the eigenvector of the covariance matrix or derived from singular value decomposition (SVD) of measured data M. The components are an orthonormal basis that spans the column space of transformation matrix U:

$$R_{PCA} = U^T M. \quad 2.20$$

The orthonormal matrix U represents the decomposition of principal components for the absorption spectra. The principal components regression can then be used to examine the correspondence between a principal component and a specific absorber of interest.

The benefits of PCA method is that dynamics in high dimensional data can be simplified and the most interesting principle components found by examining the first few largest variances (first $k, k < m$) while discarding the remaining components that represent noise.

2.6.4 Independent component analysis

Independent Component Analysis (ICA) [48] is another blind source unmixing, which is based on the assumption that the independent component are statistically independent and must have nongaussian distribution. According to the central limit theorem, under certain conditions, the distribution of a sum of independent random (nongaussian) variables tends toward a Gaussian distribution. Consequently, the unmixed spectral components are expected to have a less Gaussian distribution than the original measurements. The ICA algorithm, seeking to transform the dependent mixed spectral components into a set of independent source components also yields the corresponding mixing matrix U_{ICA}. One of the classical quantitative measurements of nonguassianity is called kurtosis or the fourth-order cumulant. A fast convergence and robust FastICA method to find the maximum of nonguassianity and then the independent components are derived [48].

Compared to PCA, ICA is a more powerful technique identifying the underlying factors. The unmixed endmembers (substances) satisfy the more general and stronger condition of statistical independence. However, there are no ordered eigenvalues to measure components' significance sorted as PCA. The algorithm attempts to find all the components as available measurements numbers, meaning many noise or minor signal will give rise to computation. Generally, the PCA will be introduced as preprocessing step, which causes dimension reduction, also eliminates the noise or minor components. Therefore, the unmixing is be retrieved from the subset after the PCA reduction.

$$R_{PCA/ICA} = U_{ICA}^{T} R'_{RCA} = U_{ICA}^{T} U_{RCA}^{'T} M. \qquad 2.21$$

More details regarding the performance comparisons of these two blind unmixing methods for multispectral OA images can be found in [49].

Figure 2.7 shows the unmixing performance comparisons of those algorithms by Glatz et al. [49]. Two insertions containing ICG and Cy7 were implanted in the neck area of an euthanized mouse and scanned the region with laser illumination from 700 to 850 nm. The post-processing of the generated spectral and temporal data requires a robust and reliable method for decomposing the constitutive contributions from the measurements.

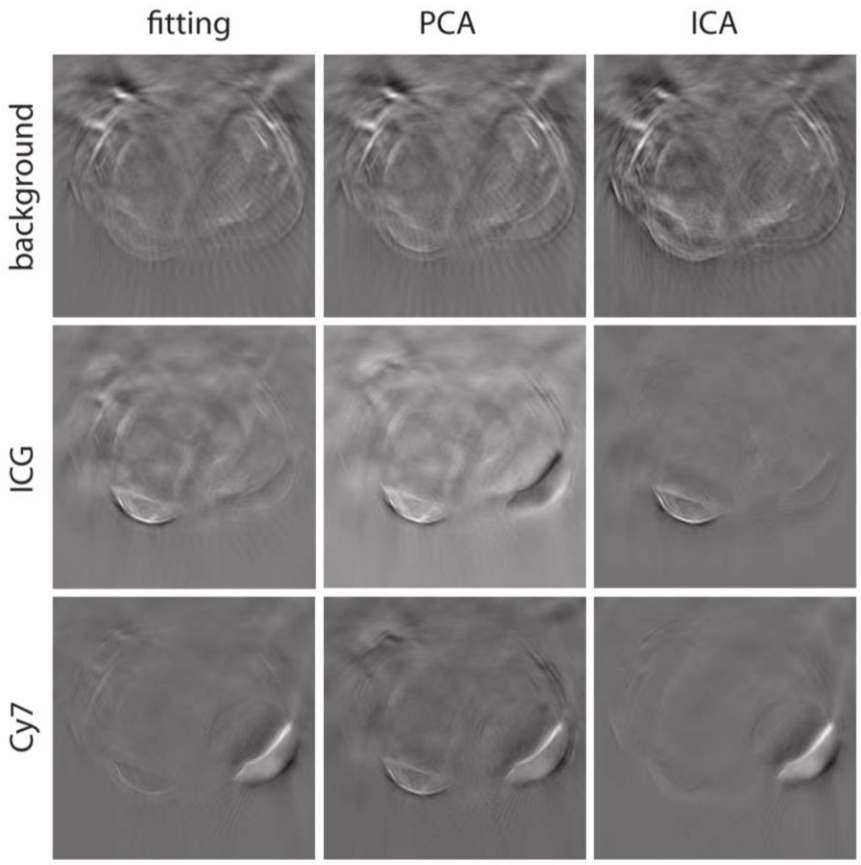

Figure 2.7: Comparison of the unmixing performance for different algorithms by Glatz et al. Reproduced from Ref.[49]. The rows (top to bottom) show the components corresponding to background, ICG and Cy7, respectively. The linear fitting (left), PCA (middle), ICA (left) algorithm from known spectra performance are shown in the column.

2.6.5 Vertex component analysis

In many practical molecular imaging applications, the purpose of the unmixing in MSOT is to determine the distribution of a specific contrast agent with known temporal or spectrum information. The spectral signature of the absorption of the substance of interest can be a priori measured by a spectrometer *in vivo* small animal imaging. Moreover, the oxygenated and deoxygenated hemoglobin spectra information can be added to unmixing components.

Vertex component analysis (VCA) [50] is a new method for unsupervised spectral unmixing is based on the geometry of convex sets. It exploits the fact that the endmembers are the vertices of a simplex and the affine transformation of a simplex is another simplex, helping to find the hidden folded vertices of the simplex. The algorithm iteratively projects data onto a direction orthogonal to the subspaces spanned by the predetermined endmembers.

The algorithm is based on two hypotheses. The first one assumes that there is at least one pixel of the image containing a pure component, i.e., for every component j, there is a position k in the reconstructed image that fulfills $\varepsilon_{VCA,j} = H_{exp}^{k}$, where $\varepsilon_{VCA,j}$ is the j^{th} column of the matrix. A maximum of n components can be obtained with the VCA algorithm. The second hypothesis assumes that a linear combination of the absorption at different wavelengths is constant for every pixel in the image, i.e., for every pixel k of the image the flowing condition is fulfilled:

$$\sum_i a_i \, H(r_k, \lambda_i) = 1, \qquad 2.22$$

where a_i are wavelength-dependent coefficients. Figure 2.8 illustrates the principle of VCA in two-dimensions. Here two absorbing components (with absorption spectra corresponding to two vectors $\vec{a}$ and $\vec{b}$) are present and the sample is imaged at two different wavelengths (Figure 2.8). The black dots correspond to a representation of the absorbed energy at the imaged wavelengths for each pixel of the image. We further assume that the first approximation above is verified, i.e., there are two pixels A and B whose absorption spectra correspond to the vectors $\vec{a}$ and $\vec{b}$, respectively. If the second assumption mentioned above is further accurate, the pixels lie in a hyperplane defined by equation 2.22, represent as a dashed line in Figure 2.8.

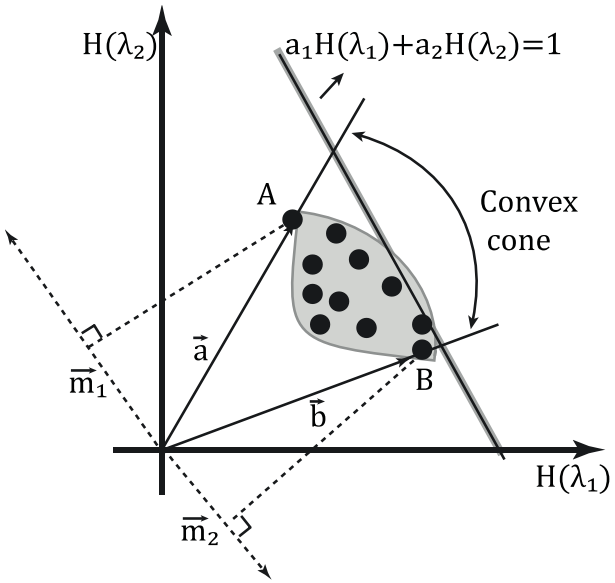

Figure 2.8: Illustration of two-dimensional vertex component analysis algorithm.

The procedure to obtain the spectra signatures works as follows. First a random direction is considered (m_1). The vectors representing the absorption of the different pixels are projected onto this direction while the pixels corresponding to the maximum value of the projection are considered. The direction defined by this point is assigned to the spectral signature of the first component. Subsequently, a random direction normal to the spectra of the predetermined components is taken, such that the new

component is obtained by projecting the absorption of each pixel on to the new direction, as described above.

This information can be then included in the VCA algorithm by taking advantage of the fact that spectral signatures are separately determined. Thus, one can fix the first l components and use the VCA algorithm to only determine the spectral signatures of the other $l - m$ components, so that the matrix ε_{VCA} is given by

$$\varepsilon_{VCA} = \begin{pmatrix} \varepsilon_1(\lambda_1) & \cdots & \varepsilon_l(\lambda_1) & \varepsilon_{VCA,l+1}(\lambda_1) & \cdots & \varepsilon_{VCA,m}(\lambda_1) \\ \varepsilon_1(\lambda_2) & \cdots & \varepsilon_l(\lambda_2) & \varepsilon_{VCA,l+1}(\lambda_2) & \cdots & \varepsilon_{VCA,m}(\lambda_2) \\ \vdots & \vdots & \vdots & \vdots & \ddots & \vdots \\ \varepsilon_1(\lambda_n) & \cdots & \varepsilon_l(\lambda_n) & \varepsilon_{VCA,l+1}(\lambda_n) & \cdots & \varepsilon_{VCA,m}(\lambda_n) \end{pmatrix} \quad 2.23$$

In general, this hypothesis may become inaccurate in cases where the light fluence variation is strong. The advantage of the VCA algorithm is that computational complexity is one or two orders magnitude lower than blind methods.

Chapter 3 Contrast agents for optoacoustic imaging

3.1 Introduction

From the prospective of signal generation, OA image reconstruction essentially is retrieving the distribution of the optical absorption of the imaged object. The image can be interpreted as a quantification mapping of the absorber. Hence, contrast agents with high absorption can be used to increase the sensitivity of OA imaging. In this chapter, the commonly available contrast agents and their application will be listed. It will be followed by an overview of intrinsic and exogenous contrast agents for OA imaging with a special focus on the state-of-the-art reporter gene development. The main requirements and challenges for contrast agent development are briefly discussed. Proposed novel pathways to develop or utilize new types of reporter genes are introduced.

3.2 Overview of contrast agents

Considering signal generating for OA imaging, a wide range of tissue-intrinsic chromophores and exogenous agents can be adapted for *ex vivo* and *in vivo* applications. Table 3.1 provides representative characteristics and possible applications of common contrast agents for OA molecular imaging. These contrast agents can generally be divided into intrinsic and exogenous contrast agents. The table lists the reporter gene (iRFP, mCherry, X-gal) and synthetic dyes (fluorescent dyes, plasmonic nanoparticles). It is important to note that the physical and chemical parameters vary among different types of compounds and environments (pH, temperature, size, etc.). Therefore, the molar extinction coefficient ($cm^{-1}M^{-1}$) normalized by concentration presents the overall efficiency estimation for OA signal generation. For fluorescent chromophores, the quantum yield is particularly important for signal generation (lower quantum yields may induce higher absorption). In addition, other parameters such as the photobleaching resistance, binding efficiency, delivery or targeting capacity, and safety/toxicity have to be taken into account.

Table 3.1: Optical characteristics of major tissue chromophores and some optoacoustic molecular contrast Agents

Chromophore	**Type**	**Absorption peak (nm)**	**Molar extinction coefficient ($cm^{-1}M^{-1}$)**	**Typical size or molecular weight**	**Application**	**Ref**
Oxyhemoglobin HbO_2	Intrinsic agent	550 750	58×10^3 520	6.8 nm	Functional OA brain imaging, cardiovascular	[51]
Melanin	Intrinsic agent	550 750	1200 470	~1 nm	Tumor imaging, multimodal imaging	[52]
Lipids	Intrinsic agent	930 1220	13.1 2.5	>100 Da	Atherosclerosis	[53] [54]
iRFP	NIR fluorescent protein	692	10.5×10^3	~190 kDa	Tumor imaging	[55] [56]
mCherry	Red-shift fluorescent protein	587	7.2×10^4	~5 nm	Transgenic zebrafish	[19] [57]
X-gal	Activated chromogenic assay	650	1×10^4	408Da	Gliosarcoma tumor	[58]
Indocyanine-green	NIR fluorescent dye	810 (in plasma)	1.9×10^5	775Da	Metabolism, pharmacokinetics	[59]
AlexaFluor750	NIR fluorescent dye	750	2.5×10^5	~2 nm	Multispectral OA, pharmacokinetics	[60]
Gold nanosphere	Plasmonic noble metal nanoparticle	520-900	1×10^8	1-100 nm	PEGylated, gastrointestinal, cancers	[61]

3.2.1 Intrinsic contrast agents for OA

In terms of biomedical applications, molecular imaging based on exogenous contrast agents suffers significant limitations when used in living subjects. Many agents are toxic and expensive to synthesis and must be delivered to transfer to the site of interest *in vivo*. Nevertheless, there are several intrinsic agents that can be readily to apply *in vivo*, yielding high sensitivity and that are nontoxic. Depending on the absorption and chemical composition, the common intrinsic OA contrast agents are hemoglobin, melanin, and lipids.

3.2.1.1 Hemoglobin

Hemoglobin, the core element of blood, is a dominant absorber among various intrinsic contrast agents in biological tissue. The main physiological function of blood is to supply oxygen, nutrients and ingredients to all tissues. Blood consists of oxyhemoglobin (HbO_2) and deoxyhemoglobin (Hb). In terms of molecular extinction, the absorption coefficient of hemoglobin is approximately six orders of magnitude higher than the surrounding tissues. Considering the quantity of blood, the concentration is also high in animals. For example, the hemoglobin of domestic pigs is 113 mg/mL [62]. Thus, in both visible and NIR, the hemoglobin would generate a much stronger OA signal than normal tissues.

Figure 3.1 shows that the molar extinction coefficient of HbO_2 and Hb both decay faster in the NIR range, explaining the critical OA NIR imaging window for *in vivo* imaging for deep tissue penetration. Because hemoglobin, bound or unbound, to oxygen has a different spectrum signature, it is possible to assess relative changes in the concentration of both oxyhemoglobin and deoxyhemoglobin, which drives changes in cerebral blood volume (CBV) and total hemoglobin (HbT). Blood oxygen level dependent (BOLD) based functional MRI (fMRI) is now widely exploited by neuroscientists to investigate cerebral vascular responses. The basic mechanism is that there is increasing energy consumption when brain is activated by stimuli. Similarly, the hemoglobin-based OA imaging can also greatly facilitate brain activity research. Compared to MRI, OA imaging is also a noninvasive, and high spatial resolution imaging modality but with higher temporal resolution. OA imaging is suitable for studying functional cerebral hemodynamic changes in cortical blood vessel around the activation cortex and the hemodynamic changes induced by hyperoxia and hypoxia. Thus, the high temporal and spatial resolution, multispectral video rate of volumetric optoacoustic imaging has great potential for *in vivo* whole brain functional neuroimaging and examining cardiovascular dynamics of heart utilizing basic contrast relies on the change of HbO_2 and Hb [32]. On the other hand, the high absorption of hemoglobin also generates undesirable background signals and creates challenges to quantifying the distribution when other contrast agents are administered. To solve this problem, a new strategy to adapt the temporal information of proteins is introduced in the chapter 5.

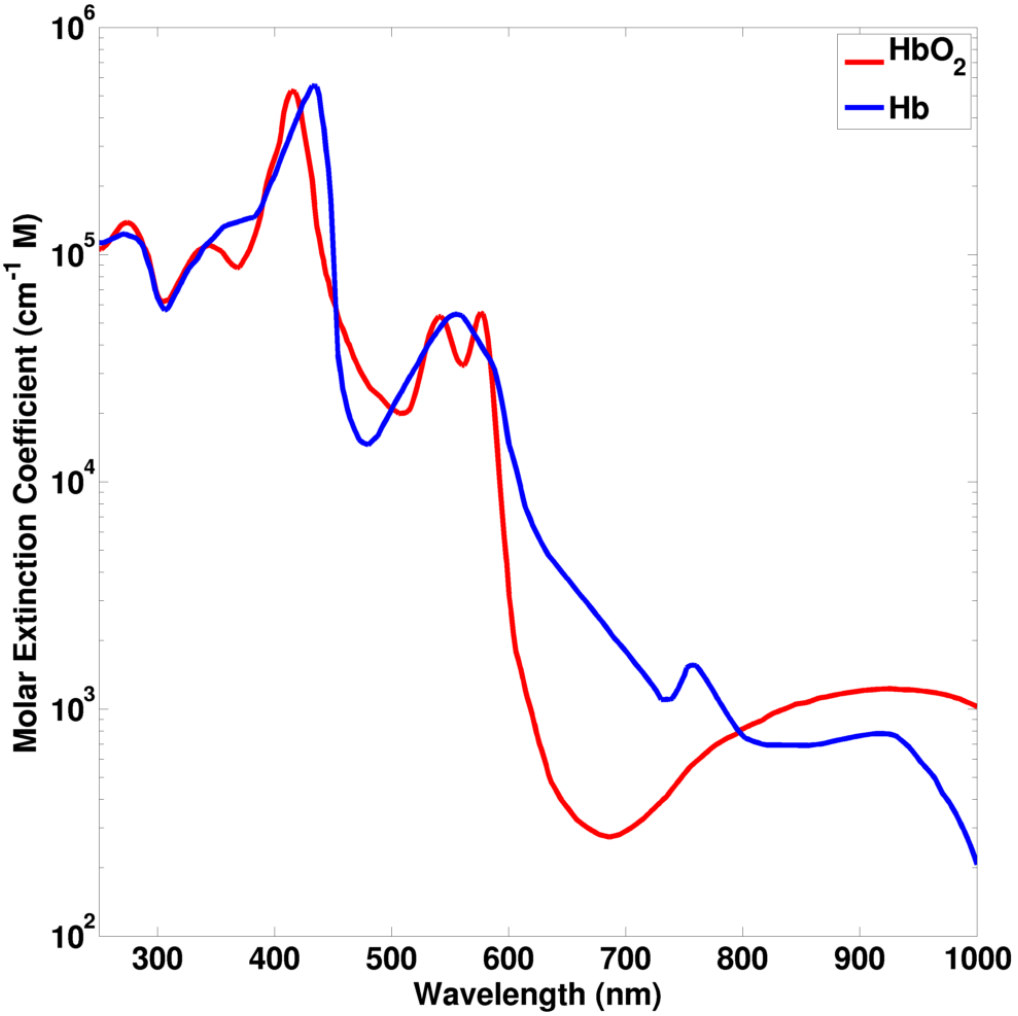

Figure 3.1: Extinction spectra of hemoglobin. Data adapted from Scott Prahl, Oregon Medical Laser Center (http://omlc.ogi.edu/spectra)

3.2.1.2 Melanin

Melanin is one of the primary absorbers in the skin and which exhibits a very broad spectrum. The natural pigment biogenesis in animals occurs through he oxidation of the amino acid tyrosine followed by polymerization. This natural chromophore is presented in most melanoma cells. Tyrosinase is the primary enzyme responsible for melanin production and its introduction into non-manlanogenic tissues results in pigmentation. It is estimated that over 95% all melanomas are pigmented [52][63]. Therefore, the OA imaging modality is capable of achieving a high resolution and high contrast to noise ratio for *in vivo* detection and evaluation of melanoma in melanin-rich tumor [64].

3.2.1.3 Lipids

Lipids are the generic names for a group of naturally fat-soluble compounds, including fats, sterols, phospholipids, and sphingomyelins. Fat lipids are common constituents to make up of plaques in atherosclerotic and cardiovascular disease. Various imaging modalities such as MRI and optical coherence tomography (OCT) have been used to visualize lipids in inside arterial walls, but have all suffered from low spatial resolution or penetration depth. Intravascular OA imaging is a promising tool to differentiate lipids in atherosclerosis due to distinct absorption spectrum in the near-infrared wavelength range with sufficient penetration depth and high sensitivity [53].

3.2.2 Exogenous contrast agents for optoacoustic imaging

However, intrinsic contrast agents have disadvantage of their own. The intrinsic agents are limited in most case of disease detection and *in vivo* applications because of their low specificity. In many scenarios, an endogenous contrast agent alone is not sufficient to provide functional information, such as distinguishing early stage tumor cells *in vivo*. This issue can be addressed by introducing genetically encoded molecules or marker proteins or synthetic chromophores. With versatile optical molecules, the power of OA imaging can be substantially extended with exogenous contrast agents.

For successful, non-invasive *in vivo* OA imaging applications, the ideal exogenous contrast agent should possess the following properties:

- High extinction coefficient and low quantum yield
- NIR spectrum
- Photobleaching resistance
- High efficiency for delivery
- Nontoxicity

As seen in Table 3.1, there are several synthetic dyes are effective OA contrast agents and most of them are nanometer scale fluorescent molecules. These NIR dyes possess relatively much higher molar extinction coefficients compared to natural gene reporters. ICG, for example, an FDA approved fluorescent dye has been widely used for various experiments such as pharmacokinetics and quantitative measurement with OA imaging. This is due to its high absorption and sensitivity. Organic dyes like AF750 exhibits distinctly sharp resonances in the vicinity of their peak excitation and can therefore achieve 25 fmol sensitivity in small animals [60]. Metallic nanoparticles shows high optical absorption with much higher molar extinction coefficient than other agents. These include gold nano-constructs such as gold nanospheres, gold nanorods, nanoshells, nanocages, and nanoprisms that are based on the localized surface plasmon resonance. Table 3.1 only lists one example of gold

nanospheres, which indicate the variable size distribution, causing the absorption peak shifts and the capability of conjugating other target receptors, such as with anti-HER2 and anti-EFGR [65].

Generally, synthetic dyes have the advantages because of their optical absorption spectra, molecular extinctions, variable size dimensions, functionality designs, and surface modifications. However, the disadvantages of synthetic dyes include lower targeting effectiveness, slower clearance, and relatively larger size, biodegradability, and safety problems for *in vivo* applications. Therefore, the development of gene reporters for OA imaging is the main focus of this dissertation. Further details about the chemical dye molecules development and applications in OA imaging can be found in [65][66][67][68].

3.3 Genetically controlled agents for optoacoustic imaging

3.3.1 Reporter gene

The reporter gene has become a powerful and rapidly expanding tool in molecular imaging over the last several years. In general, a reporter gene consists of a reporter gene and corresponding probes for visualization. By attaching a reporter gene to another gene of interest under the same promoter, cells that express the gene of interest also proportionally express the products of the reporter gene (e.g., receptors or enzyme). The gene products are the expression of proteins or enzymes that can be imaged and the amount of expression is dynamically under the control of a specific promoter. The most common approaches currently exploited in reporter gene imaging studies include enzymes and cell-surfaces receptors. The benefit of the enzyme approach is that one enzyme can interact with contrast agent molecules, leading to the amplification of the reporter expression, whereas the protein of interest expression level is limited (although not necessarily a 1:1 relationship).

For *in vivo* imaging, biological components (e.g., tumor cells, enzyme, or bacteria) are tagged with the encoded reporter gene. Hence, a specific gene inserted or fused with reporter gene in transgenic animal models can be used to study the signaling pathways, gene expression, cell apoptosis, and therapeutic drug developments. Common strategies are to develop targeted compounds that labeled with fluorescent molecules for optical imaging, paramagnetic ion for MRI, or radionuclides for nuclear imaging, or alternatively to use small particles that enable detectable signals by those imaging modalities. In principle, the OA imaging is technology based on sensing the color of molecules. The color of a molecule is a selective absorption of certain wavelengths of visible light and the transmission or reflection others. Thus, for OA imaging, light-sensing fluorescence proteins and enzymatic approaches are preferably employed, Moreover, biosynthetic pigments, selective color

pigments extracted from living organisms, can be beneficial for OA imaging as gene reporters (see an example in chapter 4).

3.3.2 Light-sensing proteins

Given the full richness of nature, it is no surprise that genetically encoded light-sensing proteins are optimal for studying dynamical processes *in vivo*. Several ways of utilizing reporter genes have been explored for fluorescence imaging, OA imaging, and optogenetic tools. One approach is to directly make use of genetically expressed light-active biological photoreceptors for optical imaging. Phototrophic organisms make use of light energy, thus, those light-sensing proteins can be triggered with specific wavelength illumination and offer excellent time-resolution relevant to signaling function and dynamical structural transitions. A great diversity of photosensory protein characteristics can be classified in to six families based on the structure of the chromophore. These are rhodopsins, phytochromes, xanthopsins, phototropins, cryptochromes and blue-light sensing proteins [69]. Athe last three can be further grouped into the flavoproteins as they have a different flavin-based photochemistry. Rhodopsin mostly absorbs green light and also exists in cells of vertebrate retina. Phytochrome is a red and far-red light photoreceptor found in the bacteria and plants. Xanthopsins (also termed photoactive yellow proteins) are the family of eubacteria blue-light photoreceptors with maximum absorption at 466 nm. Conventional and novel development based on green fluorescent proteins (GFP), blue, yellow, cyan, and red FPs result in a GFP-like protein family. The first FP working above 650 nm is the near-infrared fluorescent (iRFP) family with an absorption peak in the 680-720 nm range [55][70]. Figure 3.2 lists the major spectral properties of available groups of photo sensing proteins and their key chromophore structures.

3.3.2.1 GFP-like protein

A conventional and most widely used reporter gene is the straightforward introduction of FPs for OA applications. Fluorescent proteins, like the GFP family, such as eGFP, mCherry, and DsRed have been visualized by OA imaging in relatively transparent zebrafish and small scale Drosophila (fruit fly) pupa [19]. The advantages of using fluorescence proteins in OA imaging are twofold. First, the well-studied spectra and temporal excitation/illumination properties of these FPs can lead to robust OA signal generations as long as the sensitivity is sufficient. Furthermore, these reporter gene constructs are already available for specific biological processes, such as gene expression and signaling at a cellular level or surface tissue imaging (<1 mm) in living animal models. The use of these proteins is more difficult for deep tissues or whole body OA imaging. This is because of photon diffusion in which multiple scatterings contributes to the OA signal without degrading the signal quality. Moreover, the use of protein cDNA as a reporter gene for OA imaging is still not optimal. The small quantum

yield (Φ_F) of FPs is a more favorable candidate because the OA signal is in proportion to the nonradioactive quantum yield ($1 - \Phi_F$). Therefore, non-fluorescent chromoprotein mutants such as aeCp597 and cjBlue exhibit greater OA signal efficiency and better photostability [71].

3.3.2.2 iRFP family

The bacteriophytochrome photoreceptor (BphP) utilizes biliverdin as a chromophore as is ubiquitous in mammalian tissue. Bacteriophytochrome photoreceptors can also exist in two stable conformational forms, termed Pr and Pfr states. It undergoes Pr to Pfr conversion upon 630–690 nm light illumination and Pfr to Pr conversion upon 730–790 nm light illumination. Bacteriophytochrome photoreceptor variant engineering (iRFP, iRFP, Wi-Phy) makes it greatly promising for becoming templates for red-shifted NIR gene reporter, as with the GFP-like family. Its unique photochemical features make it a good reporter gene for deep tissue imaging at NIR for OA imaging. However, its biosynthesis requires the pigment biliverdin (not naturally occurring in lower animals) as the chromophore, a by-product of heme degradation. Thus, it can be complicated by the need for systemically administration biliverdin to induce fluorescence and OA signal *in vivo* imaging [72].

3.3.2.3 Biosynthesis pigments

Given the enormous number of biological, pigmented substances of living organisms that have color absorption, a gene reporter based on biological pigments could open extensive windows for OA imaging gene reporter strategies rather than FPs. Biological pigments are compounds produced by living organisms with color, resulting in wavelength selective reflection and absorption. These pigment molecules provide a wide range of colors ranging from yellow to red and are widely distributed in living subjects. Pigments in plants including chlorophyll, carotenoid, flavonoid/anthocyanin, and batalains absorb light for photosynthesis or flower coloration [73]. Naturally derived pigments such as carotenoids, carotenoproteins, tetrapyrroles (chlorophylls and phycobiliproteins), and melanin are used for signal communication or protection in animals. Carotenoid, porphyrin, heme, and melanin pigments have been exploited for quantitative measurements via OA spectroscopy [74][75]. However, the further excavation of the expression of these existing pigments in animal model to provide molecular contrast is meaningful and essential for *in vivo* imaging.

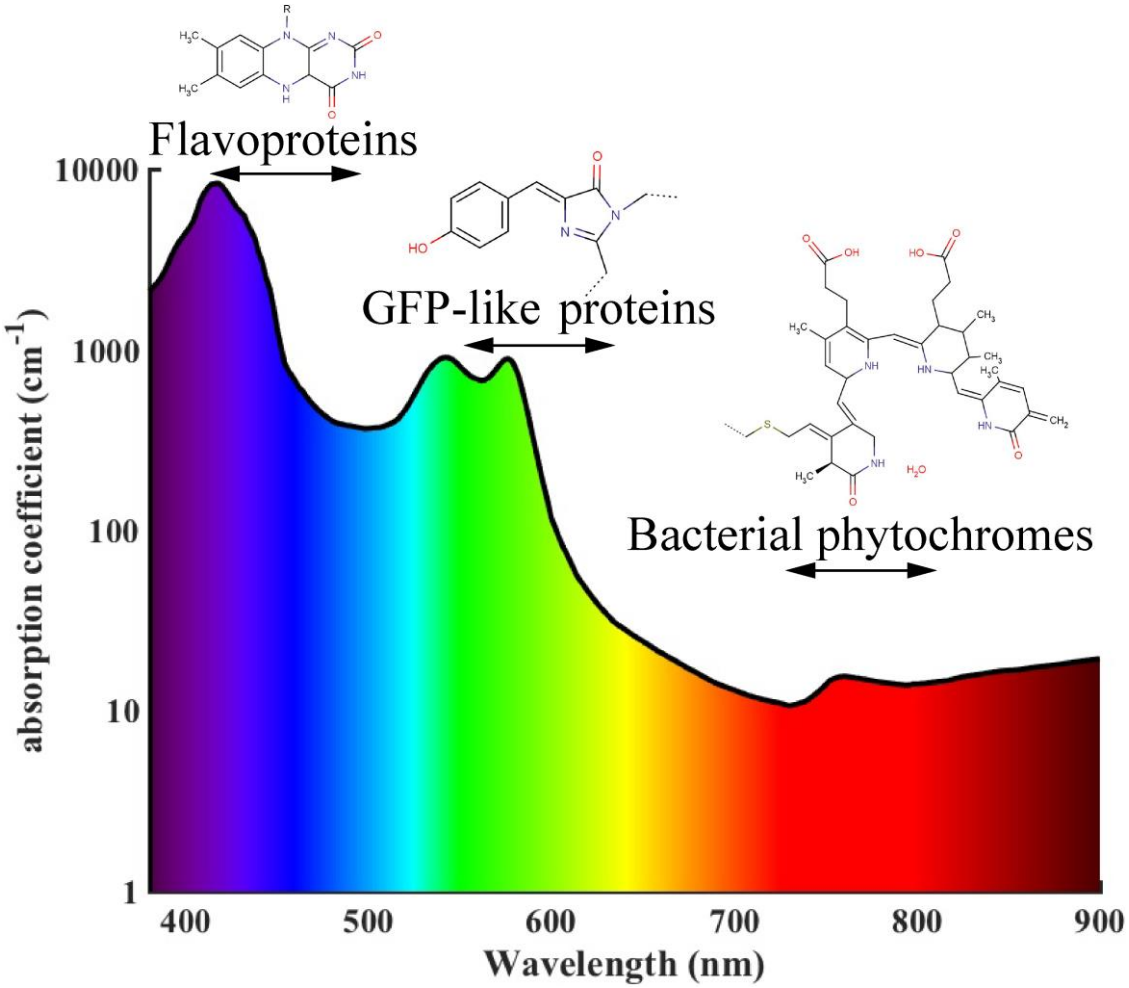

Figure 3.2: A diversity of the chromophores in their major groups of currently available proteins developed for OA applications is shown. The graph is calculated with following assuming for normal tissue (hemoglobin concentration of 50 mM, 70% oxygenated saturation, 50% composition of water, 15% lipids), absorption data obtained from http://omlc.org/spectra/ and Ref. [76])

3.3.3 Genetically controlled contrast agents

In general, fully genetic and semi-genetic mechanisms involve biosynthesis controlled endogenous contrast agents. In fully genetic terms, the gene expression of a single gene directly generates contrast in transfected cells or tissue. A semi-genetic labeling approach involves expression of receptors as an interface to bind at least one exogenous component. A number of fully genetic or semi-genetic controlled strategies can be grouped with OA contrast agent development.

3.3.3.1 Fully genetic genetically encoded approach

As discussed, melanin is a strong intrinsic absorber in mammalian tissue. This pigment has strong broadband optical absorption, extending to the NIR wavelength range so that it can avoid strong absorption from hemoglobin. Genetically encoded enzymatic approaches to express tyrosinase (TYR) offer the most promising applications to make use of the strong absorption of melanin. Tyrosinase catalyzes the formation of the pigment melanin from tyrosine precursors. Thus, the enzymatic gene reporter as a TYR protein holds the amplification potential to make many melanin sub-units. For example, a TYR reporter can be simply introduced into cells through gene transfer. Melanin is then produced in the cell while TYR catalyzes the oxidation of tyrosine precursors [77]. However, the expression of TYR shows low-level toxicity in mammalian cells and could cause significant cell death. In one inducible system (Figure 3.3), the TYR can be turned on by an inducer doxycycline (DOX) through drinking water [78]. In addition, insertion of key enzymes in melanogeneset
ais to vaccine virus can serve as a theranostic agent for MRI and OA imaging [79]. Amit Jathoul et al. first showed the transgenic expressing of TYR in mammalian cells *in vivo.* A retroviral vector approach was introduced, allowing for the co-expression of TYR and a convenient surface marker gene permanently biosynthesize melanin. With this strategy, it is possible to synthesize the pigment melanin with human cell lines and genetically labelled xenografts in mice for longitudinal visualization of expanding cell population was achieved [80].

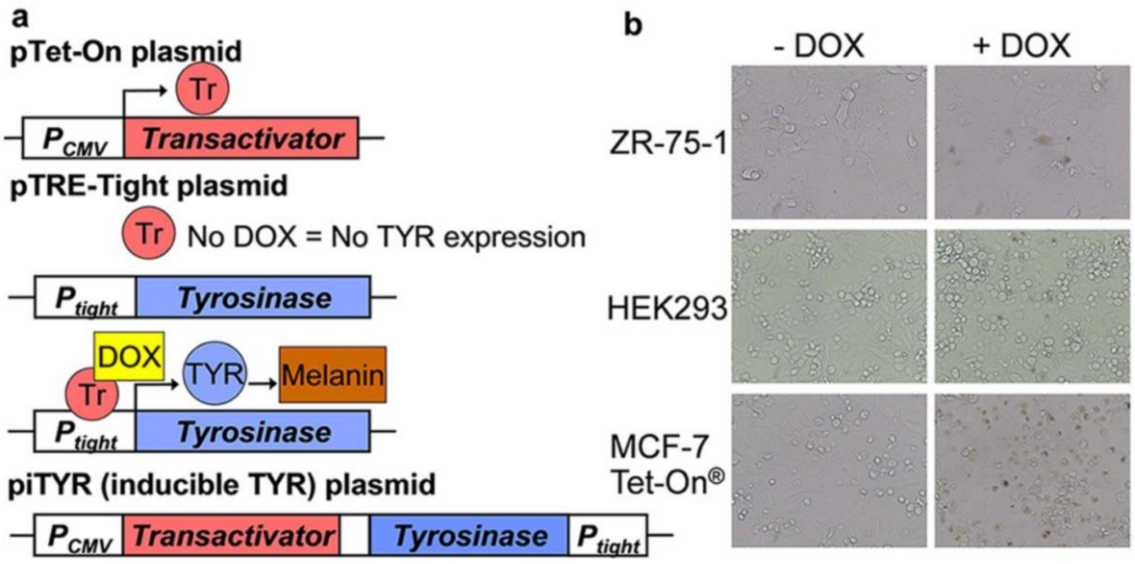

Figure 3.3: Fully genetic expression of tyrosinase can be turned on/off by adding the inducer doxycycline (DOX). Reproduced from [78].

3.3.3.2 Semi-genetics reporter genes

One of the most widely used semi-genetic reporter genes, lacZ, also has been demonstrated with *in vivo* OA tomography. The lacZ gene encodes an *E.coli* enzyme β-galactodsidase, which is responsible for lactose metabolism. By locally injecting X-gal (Figure 3.4), an optically transparent lactose-like substrate, insoluble blue compounds will yield the cleavage of the glycosidic linkage with encoded β-galactodsidase [58][81]. A β-galactodsidase molecule can cleave multiple X-gal molecules thus produce a large amount of blue compounds. This semi-genetically encoded enzymatic approach and thus possesses the potential of signal-amplification. However, the limitation of this semi-genetic approach is the requirement of a local injection of the exogenous chormogeneic substance (X-gal) into the region of interest to visualize the distribution of β-galactodsidase. For *in vivo* application in rats, this semi-genetic approach shows a low efficiency X-gal metabolism in tumors if delivered through the tail vein and occasionally causes skin irritation [58].

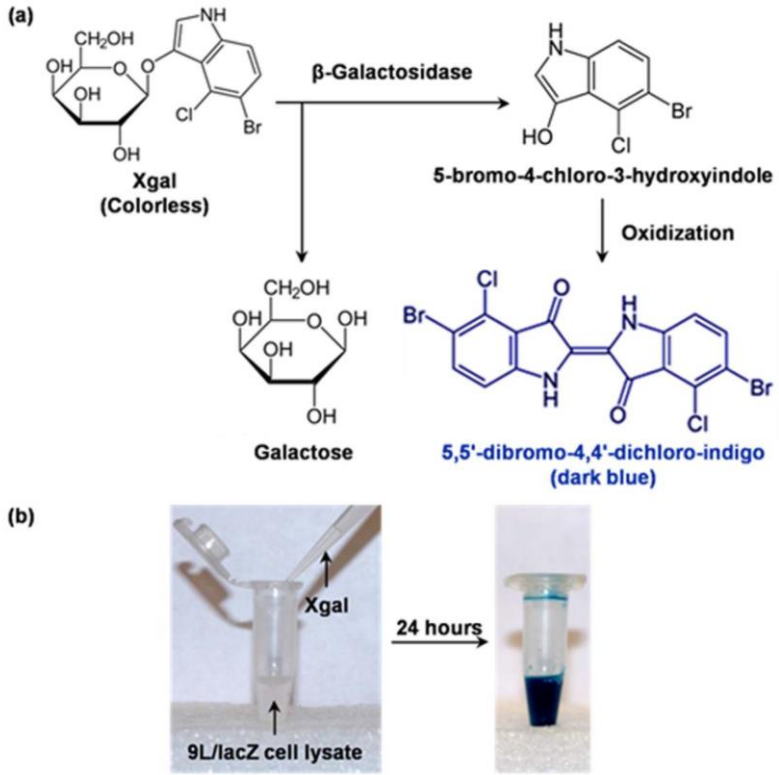

Figure 3.4: Semi-genetic expression of LacZ gene by injecting colorless X-gal and produce blue product molecules can be detected by optoacoustic imaging. Reproduced from [81].

3.3.4 Smart reporter genes

One exciting aspect of molecular imaging is the activatable reporter genes or smart agents. These agents can be switched ‘on’ and ‘off’ when the contrast agent meets specific targets or external excited source such as light or magnet. Compared to conventional probes, these agents show a unique specificity for targeting and superior control of the activation. These activatable agents have been extensively applied in optical and MRI imaging modality, but have rarely been implemented in OA imaging. One example of an activatable approach is a relatively indirect methodology, i.e., the subtraction of chromophore signals through cleavage strategy [82]. For example, an activatable cell-penetrating peptide consists of two chromophores (with similar OA signal intensity at different absorption peaks), but only one chromophore in the cell-penetrating peptide portion accumulates in the targeted cell (metalloprotease 2) while the other one diffuses away after the probe is cleaved by the appropriate enzyme. Thus the subtraction of OA signal at dual wavelengths could reveal the location of the activated probe. This indirect cleavage strategy hinders its accuracy and effectiveness of *in vivo* implementation. This dissertation discusses the possibility of introducing directly activatable reporter genes.

3.4 Challenges of OA gene reporter

For *in vivo* molecular imaging, efficient reporter genes are essential because diseased tissues or activated neurons cannot easily be distinguished *in vivo* using endogenous chromophores. Considering the gene synthesis mechanism, the fully genetic approach allows for a more effective visualization, as the complex semi-genetic system involves genetic expression of a protein that indirectly generates absorption through interaction with exogenous agents. In a fully genetic method, the expression of a single gene is able to produce OA contrast in transfected cells or animal. For OA imaging, high absorption in the NIR with high absorption coefficients is desired. High contrast and sensitivity *in vivo* re not only the consequences of favorable optical and optoacoustic signal efficiencies, they are also related to expression level in targeted tissues, delivery, photobleaching resistance, the ability to amplify signals, as well as optimizing instruments, reconstruction algorithms, and multiplexed information processing techniques.

However, most FPs are not ideal contrast agents for OA imaging. Many fluorescent labeling agents have relatively low molar extinction coefficients and high quantum yields, meaning OA optoacoustic signal from thermal energy conversion is relatively lower than the low quantum yield species. Second, FPs are prone to laser-induced absorption bleaching, complicating photoacoustic imaging, lack photostability, and cannot provide sufficient OA efficiency above 650 nm to avoid the high absorption

of the intrinsic absorber hemoglobin. Finally, compared to enzymatic reporter gene, most FPs do not have the amplification potential. For an enzymatic reporter gene, one molecule of the enzyme can interact with many substrate molecules, thus providing signal amplification, increasing the sensitivity of detection. Thus, the strategy is to find chromophores with high extinction coefficients in the visible or NIR. Nevertheless, it also worthwhile to make use of small pigments which may have greater signal generation efficiency because there is less photoemission after excitation/illumination.

Finally, optimal molecules are introduced. Most are administrated intravenously (*i.v.)* for rapid distribution throughout the body. Thus, those agents (with exception of intravascular agents) must be able to target to the tissue through bloodstream. The hurdles of specific targeting may be particularly severe for neuroimaging applications, which must cross the BBB. This barrier is formidable for the delivery of most contrast agents.

The ideal contrast agent could lead to significant OA signal improvement, image depth, and improvements in accuracy. To address current common genetic labeling issues in OA imaging modality, here we propose the development of a new strategy with greater OA signal efficiency and sensitivity for *in vivo* application:

- Signal amplification: ‘no dilution’ of the contrast agent due to genetic encoding that is being passed on.
- FPs: ‘optimized’ chromoproteins in the NIR and contain photobleaching resistance and high absorption.
- A new segway for special proteins with temporal information to be adapted for OA application.
- Non-invasive and efficient techniques to deliver contrast agents across the BBB.

Chapter 4 A genetically-controlled, chromophore for optoacoustic bacterial imaging

4.1 Introduction

This chapter discusses an improved genetic biosynthesis pigment violacein (Vio) for OA bacterial imaging. To empower noninvasive, high-resolution bacterial tracking with deep penetration, we introduce the genetically controlled biosynthesis of the deep-violet pigment Vio as a photobleaching resistant chromophore label for *in vivo* OA tomography imaging. First, a brief introduction is given concerning biological properties and potential applications of Vio. The focus then turns to its genetic reporter constructs and production in *E.coli*. The spectra measurements from an OA spectrometer demonstrate its broad spectra in the NIR and photobleaching-resistant characteristics. Finally, reporter genes are imaged with Vio with high contrast-to-noise in strongly vascularized xenografted murine tumors and it is further observed that Vio shows anti-tumoral activity. The contents of this section have been submitted for publication to *Scientific Reports* [83].

4.2 Violacein as a genetic reporter for bacterial imaging

4.2.1 Introduction of bacterial imaging *in vivo*

Bacterial populations *in vivo* imaging has become an area of growing interest for study of infectious disease research and microbiome [84][85], as well as for bacterial tumor targeting in theranostic applications [86][87]. Reporter gene expression in targeted bacteria is widely used for the detection bacterial localization and tumor colonization. Molecules such as the luciferin-luciferase system ferritin [86][88], magnetotactic bacteria [89], or thymidine kinase [90] have been used as reporter genes for detection of bacterial colonization *in vivo*. Compared to bioluminescence, MRI, and PET imaging techniques used in these studies, OA imaging provides high temporal and spatial resolution with scalable image depths. Optoacoustic spectrometer measurements tagged with nanoparticle-conjugated antibodies have been performed within blood vessels [91]. However, the robust detection of genetically labeled bacteria *in vivo* via OA imaging has, so far, not been accomplished.

Due to their poor photostability for generating robust OA signals [71], the applications of conventional FPs or chromoproteins are hindered in deep tissue bacterial imaging. In contrast, biosynthetic pigments such as melanin have the advantage of favorable optical absorption and signal amplification because of their high expression level by rapid bacterial growth. Natural products have long been explored in biologically active structures and as sources of new drugs [92][93]. Melanin produced in tyrosinase-overexpressing eukaryotic cells have been exploited in OA imaging [79][94]. This approach has not yet been successfully transferred to bacterial OA imaging. In addition, biosynthetic pigments such as riboflavin, canthaxanthin, porphyrin, carotenoids or violacein have been expressed in bacterial hosts but only the visual inspection or OA spectroscopy measurements were performed [74].

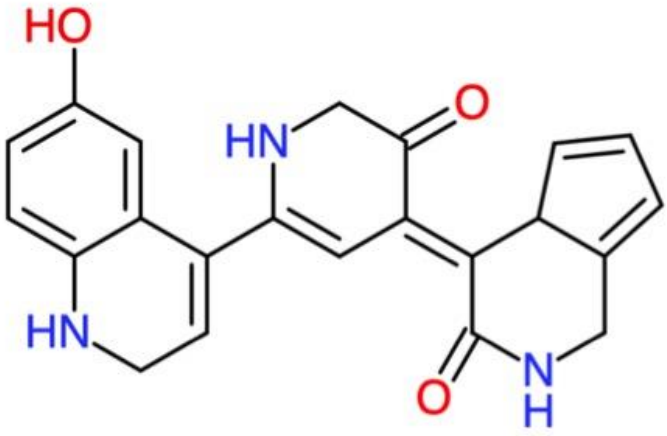

Figure 4.1: Chemical structure of violacein. The structures were prepared using ChemDoodle 2D sketcher (http://web.chemdoodle.com/demos/sketcher).

4.2.2 The violacein pigment

Violacein is one of the nature's violet pigments (molecular mass 343.3 Dalton) and is produced by diverse Gram-nagative bacteria strains, such as Chromobacterium violaceum, Janthinobacterium, and Psedudoalteromonas. In general, the genus chromobacterium violaceum has attracted most attention and is the most well studied in terms of violacein-production [95]. Violacein consists of three structural units, a 5-hydroxylindole, an oxindole, and a 2-pyrrolidone (Figure 4.1). Because the structure has two indole rings therefore it is also called a bisindole compound. The bisindole vio is formed thourgh the condensation of two tryptophan molecules through the action of five proteins. The genes *vio*ABCED are required for its production. As a compound, Vio exhibits anticancer,

antimicrobial and antiparasitary effects, making it a promising candidate as an antibiotic [96], which will be demonstrated later in the chapter.

4.2.3 Genetic reporter constructs and bacterial expression

Five genes *vio*ABCDE, are essential for the Vio production. They are transcribed in the same direction (Figure 4.2). Sánchez et al. [95] reports that the Vio locus can be isolated from the genomic DNA of *C.violaceum*(ATCC12472) as a Mlul-Xhol fragment(8.9 kb).

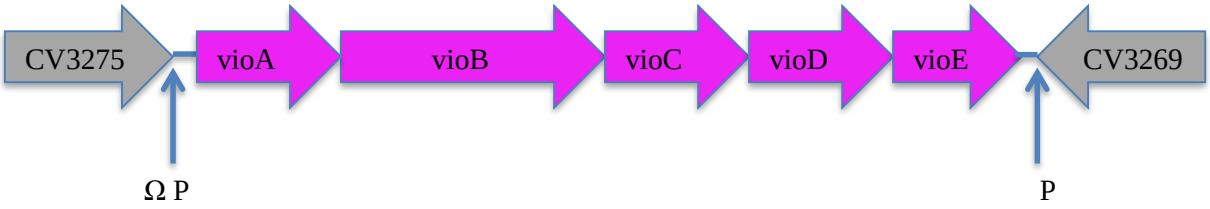

Figure 4.2: Biosynthesis from Chromobacterium violaceum encoding DNA region, violacein (vio) ATCC12472 including putative transcriptional terminator (Ω) and promoter (P) regions.

The expression of the vio gene in *E. coli* and the control protein took place in the following steps. Cultures of *E. coli* expressing the vio operon encoding the essential set of five enzymes (*vio*ABCDE) were grown in the biosynthetic pathway for the production of vio. The common fluorescent protein mCherry was selected as a reference because of its comparable absorbance spectra and its prior use in OA imaging [71]. By isolating the vio locus (*vio*ABCDE) from the genomic DNA of Chromobacterium violaceum (ATCC12472) as an 8.9 kb MluI-XhoI fragment and subcloning the DNA into lac promoter driven by LITMUS 38 with MluI and SalI, a plasmid pVIO1-2 was created. MelA from Rhizobium etli was amplified from pTrc MelA (kindly provided by Dr. Guillermo Gosset Lagarda) and subcloned into pmCherry with AgeI and NotI. pVIO1-2 (kindly provided by Dr. José A. Salas), pmCherry (the kind gift from Dr. Arie Geerlof, Helmholtz Zentrum München), pMelA and pUC19 (control bacteria) were transformed into TOP10 Chemically Competent *E. coli* (Invitrogen Carlsbad, CA, USA) according to the protocol of the manufacturer. Figure 4.3 shows the photograph of flow chips filled with bacterial suspensions producing the pigment (Vio chemical structure shown), mCherry (protein structure shown), or control bacteria.

Plasmid retention was tested *in vitro* and showed that the bacteria retains the plasmid without selection pressure for at least 7 days without any significant loss of violacein production. To yield bacterial suspensions, cultures were spun down at 4000 rpm for 15 min at 4 °C and resuspended in 25% (weight

PBS/wet weight bacteria) in PBS. As no substantial melanin formation was observed from MelA expressing bacteria in liquid culture, MelA expressing bacteria were grown on LB agar plates supplemented with 2 mM L-tyrosine and 400 µM CuSO4 for 48 hr. For photobleaching experiments, MelA expressing bacteria were scraped off the plates and resuspended in 50% (weight PBS/wet weight).

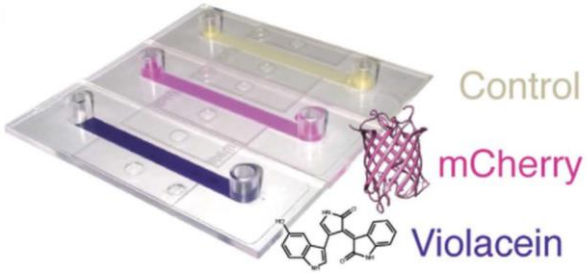

Figure 4.3: Photograph of flow chips filled with bacterial suspensions producing the pigment Vio (chemical structure shown), mCherry (protein structure shown), or control bacteria. Reproduced from [83].

4.2.4 Assessing chromophore maturation times

In comparison with cells overexpressing TYR, the rate-limiting enzymatic step for melanin synthesis, Vio pigment was measured. Whereas the absorbance of mCherry plateaued around 16 hours after inoculation, Vio expressing cells reached a 1.6 fold higher value in absorbance with a continuing upward trend (Figure 4.4). In comparison, no substantial absorbance increase could be measured from the TYR overexpressing cells grown in a shaking incubator. Only when bacteria were grown on agar plates supplemented with copper and L-tyrosine for a minimum of 48 hours, could melanin production be observed (data not shown).

To assess the pigment formation kinetics, culture flasks of *E.coli* expressing chromophore absorbance at 590 nm were measured. Single colonies of *E. coli* TOP10 cells transformed with pVIO1–2 or pmCherry were picked at 12, 14 and 16 hrs of growth time, and 50 mL of the bacterial cultures were spun down at 4000 rpm for 15 min at 4 °C and resuspended in 25% PBS (weight PBS/wet weight bacteria) in PBS. For absorbance measurements, bacterial suspensions were diluted 1:5 in PBS and absorbance was measured at 590 nm on a SpectraMax M5 (Molecular Devices, Sunnyvale, USA).

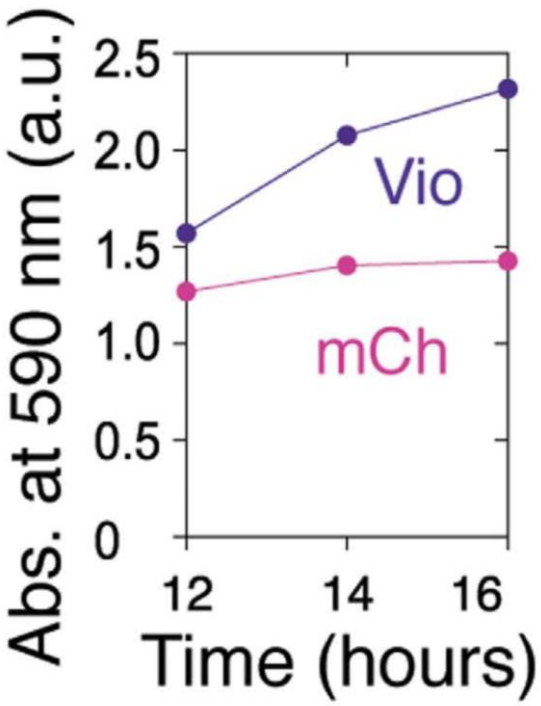

Figure 4.4: Time profile of chromophore production as measured by the absorbance (590 nm) at 12, 14 and 16 hrs. Reproduced from Ref. [83].

4.2.5 Assessing anti-tumoral activity

With respect to possible future theranostic applications, the anti-tumoral activity of purified Vio in a cell viability assay (MTT) on 4T1 tumor cells in culture was tested (Figure 4.5 a). 4T1 cells were grown in 96 well plates, treated with different concentrations of pure Vio. A significant reduction in tumor cell viability occurs at 5nM concentrations (one-way ANOVA with $p < 0.0001$; multiple comparisons against vehicle control with $p < 0.05$, Bonferroni corrected), whereas much stronger effects were observed during incubation with Vio above 100 nM. Cell viability as compared to control bacteria, Vio released from bacteria via antibiotic treatment also indicated a significant effect (paired t-test, $p < 0.0001$) on 4T1 (Figure 4.5 b).

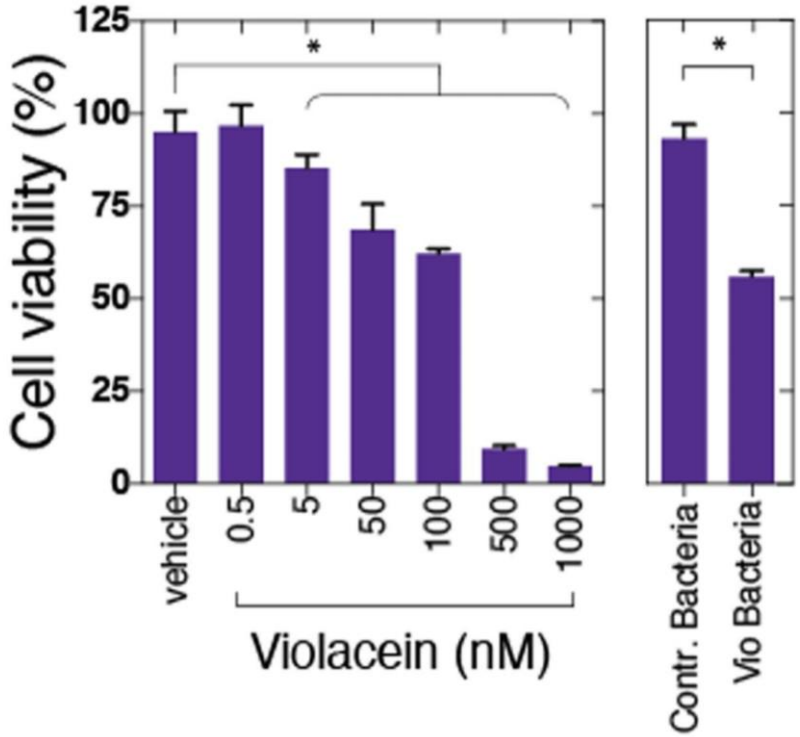

Figure 4.5: Effects of violacein (Vio) on cell viability of cultured 4T1 tumor cells against vehicle-treated cells. (a) Different concentrations of pure Vio. (b) Violacein released from bacteria. Reproduced from Ref. [83].

4.3 Optoacoustic spectra and photobleaching characterization

4.3.1 Optoacoustic spectra measurement

To compare the OA spectra of Vio and mCherry, we loaded cell culture flow chips with bacterial solutions of equal density (Figure 4.3) and placed them into a custom-built OA spectrometer (Figure 2.2) connected to a tunable visible laser. More detailed information about the setup is provided in section 2.4.2 Both Vio-expressing bacteria and mCherry exhibited a peak optoacoustic signal at ~590 nm (Figure 4.6), which corresponding to absorbance peaks and OA signal maxima. Violacein showed a relatively broader spectrum with a substantial signal still measurable above 650 nm, while mCherry-expressing bacteria showed a slightly narrower OA spectrum.

Weight-adjusted densities of *E. coli* suspensions were sequentially injected into the flow channel of the cell culture chip via the tubing. The ibidi flow chip's thin transparent foil was placed in the acoustic focus of the US detector mounted on the device's plexiglas roof. The device was then placed resting on an optical table within a water basin to ensure acoustic coupling between the sample and the

US detector. 10 channel volumes of PBS were injected to wash out the samples and was then pushed out of the channel with injected air to ensure that no dilution or inhomogeneity of subsequent samples would occur. OA spectra are shown as mean values with error bars representing the standard mean of the error.

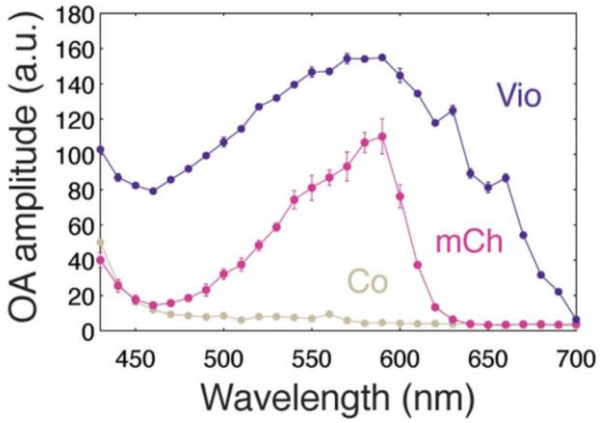

Figure 4.6: Optoacoustic spectra for chromophore-containing bacterial violacein (Vio), mCherry (mCh) strains and control bacteria (Co). Reproduced from Ref. [83].

4.3.2 In vitro photobleaching assessment

The resistance of the chromophores against photobleaching is a critical requirement for obtaining robust signals in OA imaging. Photobleaching resistance was assessed by recording the OA signal amplitude as a function of the number of laser pulses. We first measured photobleaching with the optoacoustic spectrometer at 590 nm (Figure 4.7). Vio-producing bacteria did not show significant bleaching after 25 thousand pulses i.e. over a duration of ~8 minutes, whereas mCherry expressing bacteria photobleached with a time constant of ~2150 pulses (95% confidence interval: 1940 to 2401). Monophasic exponential decay function or linear regression was used for curves plotted and fitting with GraphPad Prism 6 (GraphPad, La Jolla, USA).

4.4 Volumetric multispectral optoacoustic tomography *in vivo* imaging

After characterizing the OA properties of Vio-expressing bacteria *in vitro*, we subsequently studied how well they can be detected in tumor-bearing mice by volumetric multispectral optoacoustic tomography (MSOT). We thus injected Vio-expressing (or non-expressing) bacterial suspensions into

tumors grown from 4T1 mammary carcinoma cells xenografted a week prior to the imaging experiment.

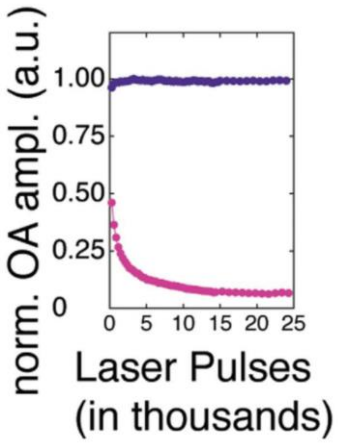

Figure 4.7: Kinetics of photobleaching measurement for chromophore-containing bacterial violacein (Vio), mCherry (mCh) with laser illumination at 590 nm. Reproduced from Ref. [83].

4.4.1 Animal preparation

The following protocol was used to form xenografts and for OA imaging preparation. 4T1 cells (1×10^6 cells in 30 µL of PBS) were inoculated into the subcutis of the neck of 8-10 week-old nude mice (matched pairs of Foxn1 - CD1 (f) and Balb/c (m); Harlan Laboratories, Germany). After 7 days of tumor growth, animals were deeply anesthetized and placed on a heat-blanket. A total 20 µL of Vio-expressing *E. coli* or control bacteria (~0.5×10^9 cfu/µL, 0.3×10^9 cfu/µL for the pair of datasets displayed at the bottom of Figure 4.8) were intratumorally injected at multiple locations within each tumor. All animal experiments were approved by the government of Upper Bavaria and were carried out in accordance to approved guidelines.

4.4.2 In vivo imaging by means of volumetric multispectral optoacoustic tomography (MSOT)

Multispectral OA images from the tumors were acquired with a volumetric three-dimensional OA imaging system (Figure 2.5). A tunable laser in the visible range was used for illumination with 450 to 650 nm wavelengths in 10 nm increments. Animals were subsequently positioned in a supine orientation on a portable volumetric OA imaging system [97] with acoustic matching provided by optically transparent agar.

Optoacoustic image volumes were acquired and rendered in real-time using a model-based three-dimensional reconstruction algorithm, essentially retrieving the volumetric distribution of optical absorption at each wavelength with an isotropic resolution of 200 micrometers [98]. Contrast-to-noise ratios (CNRs) were computed by placing a cubical ROI ($0.027mm^3$) into the tumor, the skin close to the edge of the FOV, and the background outside of the tissue and taking the absolute difference of signals acquired at 650 nm from tumor and skin divided by the standard deviation of the background noise.

Three tumors injected with Vio-containing bacteria and three tumors injected with control bacteria, the reconstructed 3D views of are shown in Figure 4.8. together with inserts of 2D projections and with the corresponding cryomicrotome slices. Anatomical contrast is provided by the data acquired at 490 nm on a color scale ranging from white to red. Vio-expressing bacteria could be clearly localized within the tumor tissue from the imaging data acquired at 650 nm (white-blue color scale), a wavelength at which Vio still generates substantial OA signals while the absorbance from blood is strongly reduced.

Different injection mechanics into the differently shaped subcutaneous tumors may cause the variable distribution of Vio across animals. There is good agreement between the OA imaging and histological section taken from an *ex vivo* axial cryomicrotome. In the distribution of first tumor, Vio was widespread and reached superficial layers. In the second tumor, Vio was located deeper in the tissue (~2.5 mm from the surface). A slightly smaller amount of Vio or control bacteria was injected at multiple positions within the third tumor group. Vio-expressing and control bacteria could also be detected in the immunohistochemistry (Figure 4.10).

This imaging data demonstrates that the strong absorption of Vio-producing bacteria close to the near-infrared window labels tumors with good depth-resolution and high contrast-to-noise ratio (268 ± 59, mean ± standard deviation) as compared to tumors filled with non-expressing controls (21 ± 6).

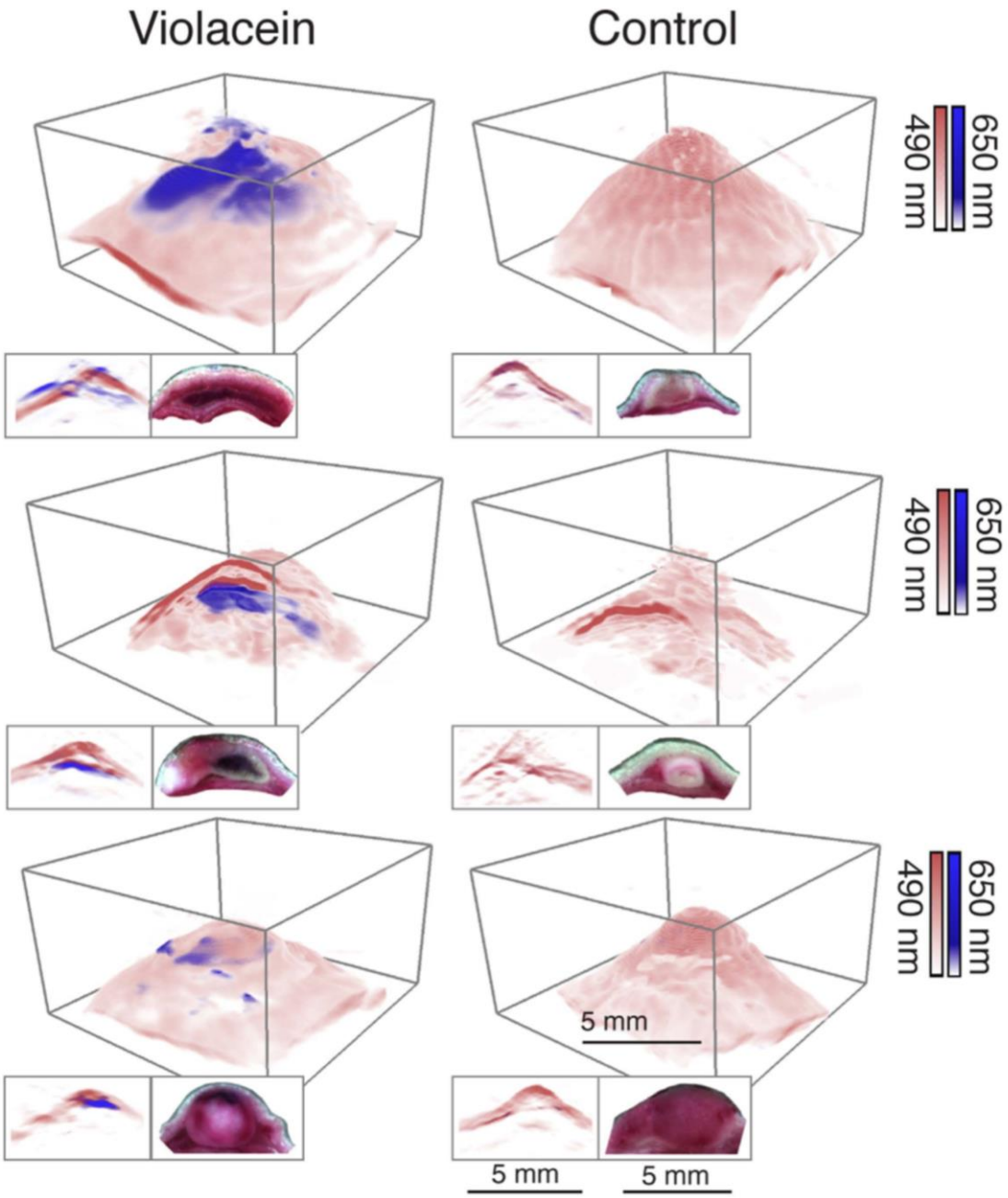

Figure 4.8: Optoacoustic imaging of bacterially labeled 4T1 tumors *in vivo*. 3D multispectral OA data rendering of obtained from grafted mice 4T1 tumors ontaining Violacein-expressing bacteria (first column) or non-expressing controls (second column). The Vio signal (white-to-blue) and anatomical display (white-to-red) indicate the signal amplitudes of data acquired at 650nm and 490nm, respectively. In each row, the 2D axial cross sections through the center of the volume (left) and corresponding color images of cryomicrotome sections through the *ex vivo* tumors (right) were underneath each 3D view OA image. Reproduced from Ref. [83].

4.4.3 Whole body MSOT imaging in near-infrared range

Whole volume multispectral optoacoustic images were acquired from the commercial optoacoustic small animal imaging system (see section 2.4.3) with an NIR range at 680nm and 710nm. In the first tumor, widespread reaching superficial layers distribution of Vio was also detected by the OA imaging system with 100 µm in plane resolution using a near-infrared laser at 680 nm (Figure 4.9). The corresponding RGB slices from vivo sectioning on cyromicrotome showed a good agreement of the MSOT detection of Vio bacterial.

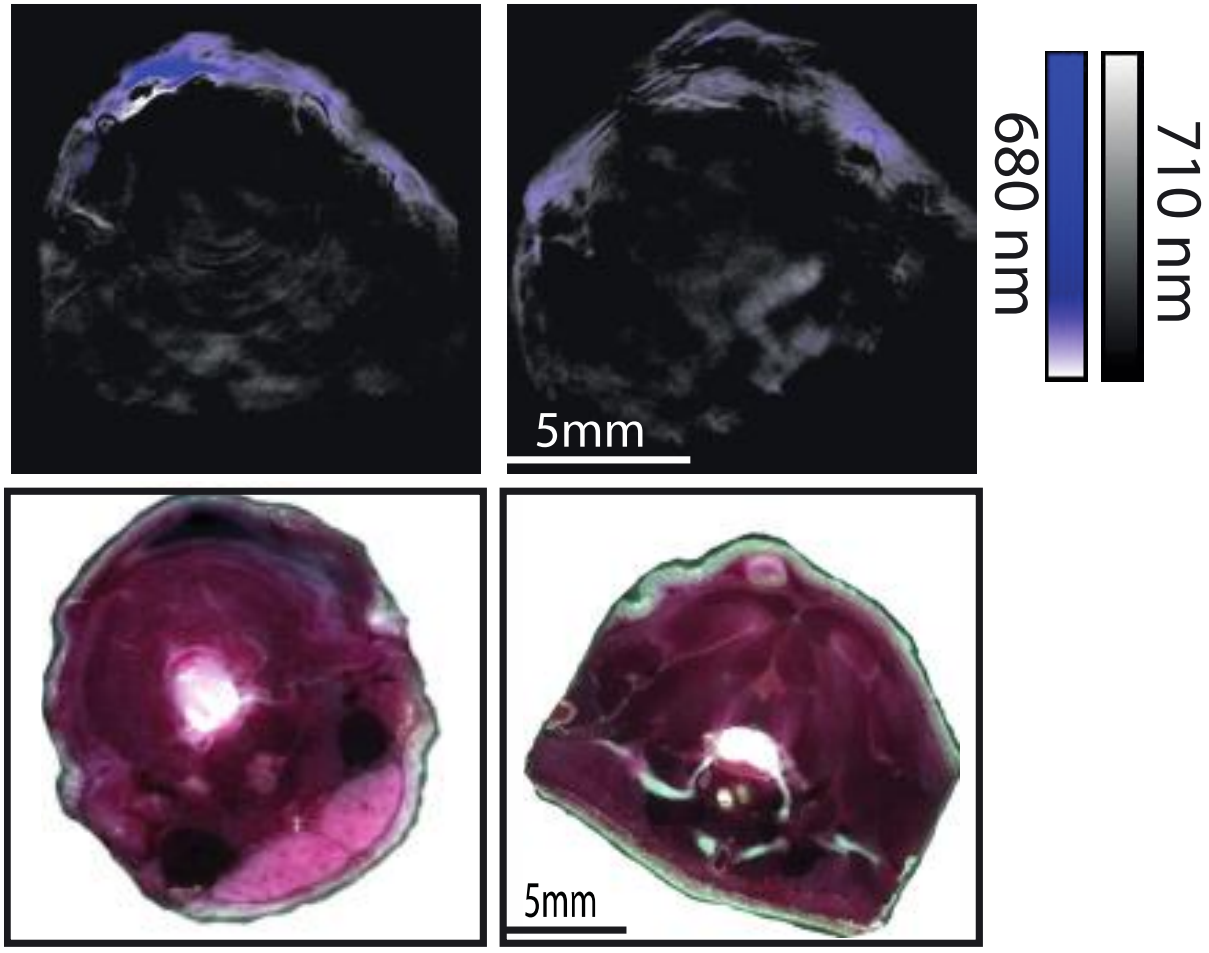

Figure 4.9: Optoacoustic Imaging with NIR laser and cryoslicing detection of Vio bacteria. The tumor seen in the upper left panel of Figure 4.8 was also imaged on the small animal OA scanner but with an NIR laser and corresponding cryomicrotome slices. Reproduced from Ref. [83].

4.4.4 Ex vivo sectioning on cyromicrotome

The mice were euthanized with a lethal dose of ketamine/xylazine and frozen to -20 °C after the *in*

vivo imaging. The upper torso including the tumor was embedded in O.C.T (TissueTeck). The embedded tissue was sectioned along the axial planes every 50 µm in a modified Leica cryotome combined with a CCD camera to capture RGB color images from the surface of the bulked remaining sample [99].

For immunohistochemistry bacterial detection, tissue sections were firstly equilibrated to room temperature and rehydrated in PBS (10 min) and blocked in 3% BSA PBS (30 minutes) at room temperature. Sections were then incubated with Escherichia coli BioParticles® Opsonizing Reagent (Molecular Probes) diluted 1:100 in PBS (30 minutes) at room temperature. Slices were then washed with PBS and incubated with 4 µg/mL goat-anti-rabbit DyLight594 (Abcam ab96897) antibody (30 minutes) and then washed with PBS. Microscopy images were acquired from an Olympus IX81 confocal microscope.

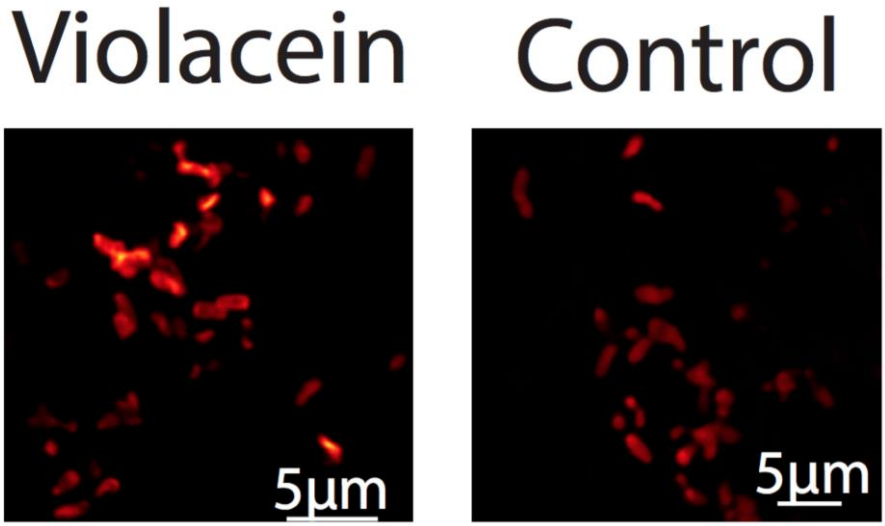

Figure 4.10: Fluorescence microscopy images of Vio-expression and control bacteria visualized after immunohistochemical detection on fixed cryomicrotome slices. Reproduced from Ref. [83].

4.5 Summary and conclusion

Longitudinal and deep tissue *in vivo* imaging of bacterial colonization are essential for determining of the bacterial infections routes and burdens [100][101][102], microbiota [85], as well as bacterial tumor targeting and visualization [86].

In terms of *in vivo* detection, it is crucial that a labeling agent not be diluted upon cellular divisions during rapid bacterial growth. Thus, genetically encoded contrast agents exhibit strong advantages over synthetic dyes as genetic information is copied to progeny. Considering non-invasive monitoring,

the bioluminescent imaging that has mostly been used for bacterial tracking so far is limited by low spatial resolution [88]. Optoacoustic imaging provides real-time, three-dimensional imaging at much higher resolutions and depths unachievable through pure optical imaging. However, conventional reporter genes' low efficiencies for signal generation limits their applicability in mammals. In this chapter, the enzymatically generated, photobleaching-resistant pigment vio showed great potential for bacterial labeling with OA imaging. We were able to robustly detect ~6×10^9 cfu bacteria in tumors in the determined range in tumor-tracking experiments after one week of intratumoral bacterial growth post intravenous injection [87][103].

In terms of alternative common labeling strategies based on FPs for OA bacterial imaging, Vio has a number of advantages. First, Vio is more efficient at converting light-absorbed energy into thermoelastic expansion as a portion of absorbed photons are converted into photoemissions in FPs, compared to the non-fluorescent pigment Vio. Second, many Vio pigments can be synthesized from the abundant substrate tryptophan from each instance of the enzymatic chain, not like in scenarios where each genetically expressed protein harbor only one chromophore, even if it is optimized [104]. Therefore, the sensitivity of bacterial detection increases through this enzymatic amplification, especially if only low protein expression levels can be achieved. Third, Vio provide almost constant signal amplitude upon excitation of lasers in the absence of the photobleaching-resistant characteristics of common FPs like mCherry. In this regard, it is interesting to investigate the maximum photostability that can be achieved with chromophores built from cyclized amino acids (as in, e.g., proteins derived from GFP), compared to chromophores bound to the protein backbones (such as biliverdin and infrared FP (iRFP) [72]) or (bio)synthetic dyes.

To noninvasively track bacterial colonization, the kinetics of cellular contrast agents matched to the fast bacterial growth are desired. Compared to mCherry, bacteria expressing the Vio operon showed rapid production of Vio. The OA signal saturation from the mCherry-expressing bacteria was not detected early. This may be because the pigment Vio has a longer lifetime compared to the FP. In addition, the multi-enzymatic biosynthesis of Vio also outperformed melanin production from TYR overexpressing cells. In our study, cells grown on agar plates produced melanin for a minimum of 48 hrs and only with supplementation of excess tyrosine and the cofactor copper. Even after 24 hrs of incubation, growth could not be achieved in shaking cultures. This indicates another advantage of Vio as a genetic bacterial label, as all steps of its synthesis are enzymatically catalyzed and do not rely on polymerization reactions, as is the case for melanin formation, or spontaneous cyclization as for the maturation of many chromoproteins.

To summary up, Vio is an excellent biosynthetic contrast agent for OA bacterial detection *in vivo* compared to a common FP (mCherry) or the biosynthetic pigment melanin. Violacein shows a strong OA signal close to NIR and exhibits high photobleaching resistance. The distinct spectrum may also

afford multiplexing applications for bacterial detection. Vio-expressing bacterial regions can be well differentiated through 3D multispectral OA imaging from strongly vascularized xenografted tumors in living mice. Moreover, its robust enzymatic amplification and fast pigment formation characteristics also qualify it as an effective output for weaker promoters or genetic circuits. Furthermore, it may be introduced to turn bacterium into a whole-cell sensor for environmental parameters or analytic areas of interest [105]. For bacterial tumor tracking, it may be particularly interesting to quantify Vio production for the sensing of, e.g., vascular growth factors or hypoxic conditions. With respect to future theranostic applications, it is worthwhile to study the anti-cancer activity of Vio-expressing bacteria *in vivo* and investigate whether the release of Vio could be coupled with genetic sensor circuits and/or placed under pharmacogenetic control [106]. Antibiotic drugs, cell-permeabilization by laser illumination or highly focused ultrasound may also take account to be effective ways to non-invasively control over Vio's anti-tumoral activity.

Chapter 5 Reversibly switchable fluorescent proteins for MSOT

5.1 Introduction

In optical imaging, the most promising strategies for addressing the challenges of delivery and targeting involve using genetically encoded molecules (fluorescent or not). Optoacoustic imaging methods are suitable for genetically encoded probes because they use the spectral properties of probes, absorbing pulsed light. Moreover, there are several light-sensing chromophores naturally present in mammalian cells or isolated by fluorescent microscopy applications, which can be adapted for OA imaging. This chapter describes a reversibly switchable FP used in OA imaging. The contents of this section have been published in *Optics Letters* [107][108].

5.2 Characteristic of switchable fluorescent proteins

5.2.1 Introduction of reversibly switchable fluorescent proteins to OA

As discussed in section 3.3.3, two strategies employ reporter genes in OA imaging studies. One approach directly uses the genetic expression of enzymes which forms an optically absorbing chromophore, providing the source of the contrast [109]. Another semi-genetic approach makes use of the expression of colorimetric enzymes or proteins but requires a local injection of an exogenous chromogenic substance. The latter approach makes use of an exogenous contrast agent with physical or chemical properties to visualize reporter genes when placed inside an imaging system. Imaging enzymes are more effective than receptors because enzymes are not altered or destroyed in the interaction. In both cases, however, the imager must wait for some time until the unbound contrast agent is cleared such that the contrast primarily arises from molecules accumulating on cell-surface receptors. Any agent molecules remaining in the circulation routes and unspecific bounding reporters would induce background signal. Minimizing the background is therefore one of the key elements of contrast agent development.

Fluorescent proteins have become the most widely used reporter molecules in noninvasive studies of biological processes at cellular and sub-cellular levels. For fluorescent imaging, dedicated optical filters with the appropriate bandwidth based on the contrast agent's emission spectrum and/or excitation wavelength have been employed to differentiate specific fluorescent contrast agents from background signals. Unlike of conventional microscopy, super-resolution microscopy is able to visualize objects smaller than 200 nm, beyond the light diffraction limit. In recent years, one of the most exciting advances in molecular imaging technology is super-resolution microscopy combined with genetically encoded activatable FPs to visualize object. Compared with conventional receptor-based approached, activatable (smart) contrast agents allow for improved sensitivity and more complex readouts. The image contrast is enhanced when smart molecules are switched on or off with specific biologic targets or irradiation conditions.

Smart fluorescent protein agents can be categorized in three forms: photoactivatable FPs (PAFPs), photoswitchable FPs (PSFPs) and reversibly switchable FPs (RSFPs). Photoactivatable FPs can be activated from a nonfluorescent (dark) state to fluorescent state, whereas PSFPs undergo activation from one fluorescent state to another in response to light. In contrast to PAFPs and PSFPs, which can only undergo photoconversion form once, RSFPs can be switched reversibly between a fluorescent and a nonfluorescent state [110]. These properties are facilitated with a permanent covalent (for PA- and PSFPs) or reversible modifications of the chromophores (for RSFPs) that result in altered fluorescence as well as absorption characteristics.

In general, the CNR of fluorescent contrast agents can be improved through the following strategies: selectively acquiring a larger portion of the spectrum with multiple filters, CCD detectors, and spectral unmixing algorithms with information. Strategies to increase the CNR with reversibly activatable FPs (smart agents) for OA imaging are presented in this chapter.

5.2.2 Switchable fluorescent protein Dronpa and the fast switching variants

A photoswitching probe, Dronpa, was introduced for OA applications in the current study. Its fast-switching variant Dronpa-M159T was used for comparison as this variant exhibits a far superior fatigue resistance compared to wildtype Dronpa. Traditionally, photoresponsive chromo-/fluorophores have been used in tracking schemes [111] and single molecule studies [112], as well as for so-called super-resolution microscopy techniques that enable fluorescence imaging well beyond the diffraction limit [113][114][115][116]. It has furthermore been shown that the photocontrol of their fluorescence

signal can be used in an optical lock-in method or Fourier domain scheme to enhance signal detection [117][118].

Dronpa is one of the most prominent RSFPs in cell biology applications as it has excellent switching properties and a favorable high quantum yield (0.85). It is a GFP-like FP cloned from coral Pectiniidae with a *ß*-barrel surrounding a central *α*-helix containing an autocatalytically formed chromophore [119]. This GFP-like FP can be reversibly switched between a fluorescent on-state and a nonfluorescent off-state by irradiation with light [119]. Dronpa and its fast-switching fatigue resistant variant Dronpa-M159T molecules exhibit fast switching kinetics over many switching cycle without fatigue (more than 100 times) [120]. The ability to be repeatedly switched on and off of the variant has a distinct advantage of RSFPs over the established reversibly switchable FPs.

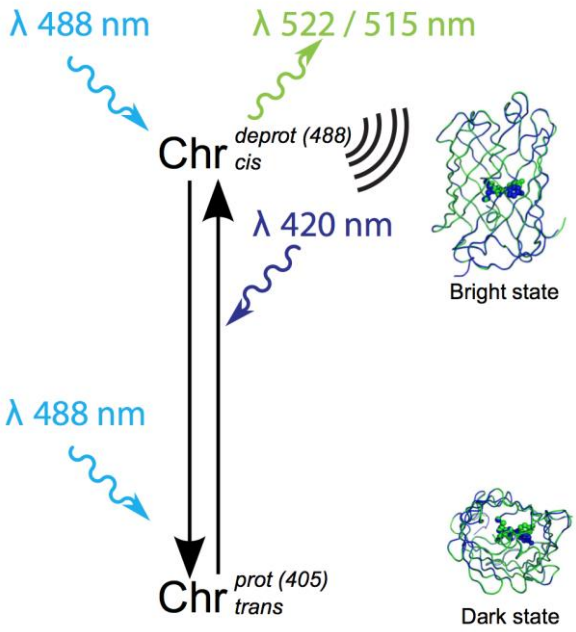

Figure 5.1: Photophysical properties of Dronpa and its mutation Dronpa-M159T. Reversible switching is realized by irradiation with (488 nm) light to dark state and UV (405nm) light to a bright state (420 nm was used due to the limitations of the laser system). The on- and off-structure in orthogonal views are inserted.

For excitation, intense light of the 488 nm laser light (conveniently used due to a laser, but not necessary in OA applications due to the application of an OPO laser) transfers the protein to a non-fluorescent off state (adopting a *trans* conformation, dark state). Subsequent minimal irradiation with UV light (around 400 nm) transfers the chromophore back to the on-state (corresponds to the *cis* conformation, bright state) and restores fluorescence (Figure 5.1) [121]. At equilibrium, Dronpa

displays bright green fluorescent with an emission maximum at 522 nm. The variant exhibits absorption maximum at 489 nm, and corresponding to emission at 515 nm.

For both types of RSFPs, green fluorescence can be excited by illumination with blue light which also switches them from their fluorescent equilibrium state to a nonfluorescent dark-state. This is accompanied by a change in the absorption spectrum and features a hypsochromic shift of the absorption maximum. Subsequent irradiation with violet light results in the reactivation of the fluorescent state, with the process being fully reversible for a number of cycles. The proteins differ in their kinetics for their off- switching. Under identical illumination intensities, the variant Dronpa-M159T is several times faster as compared to the wildtype Dronpa depending on the exact experimental conditions ([120] ~1100×, [122] ~59×). The on-switching is only slightly affected by this acceleration with an approximately twofold faster rate for the variant.

The absorbance measured for this study is shown in Figure 5.2. The concentration of Dronpa is 15mg/ml, Dronpa and variant Dronpa-M159T shows the equal absorption at the 488 nm.

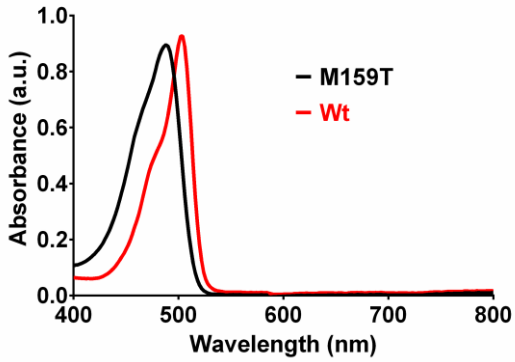

Figure 5.2: Absorption spectra of Dronpa and Dronpa-M159T.

5.3 Materials and methods

5.3.1 Imaging instruments

In the current study, we demonstrate how the photoresponsive signal of Dronpa and Dronpa-M159T can be used for enhancing their contrast for OA imaging. This is achieved by photoswitching the compounds according to defined schedules which elicit programmed time-varying OA signal time courses, which can be temporally unmixed to enhance the localization of a specific contrast. We termed this temporally unmixed MSOT (tuMSOT), a strategy to well-differentiate between Dronpa

variants despite their highly similar OA spectra and clearly distinguish them from strong background absorbers such as blood. To generate photocontrolled OA signal time courses, proteins from Dronpa and its fast-switching fatigue-resistant variant Dronpa-M159T (purified from *E. coli*) were injected into an acoustically coupled flow chip. The sample was illuminated from two sides via fiber optic light guides (section 2.4.2) coupled to a pulsed laser source delivering pulses of a 10 ns duration with a pulse repetition rate of 50 Hz. The OA images displayed were measured with a volumetric three-dimensional OA imaging system (section 2.4.4).

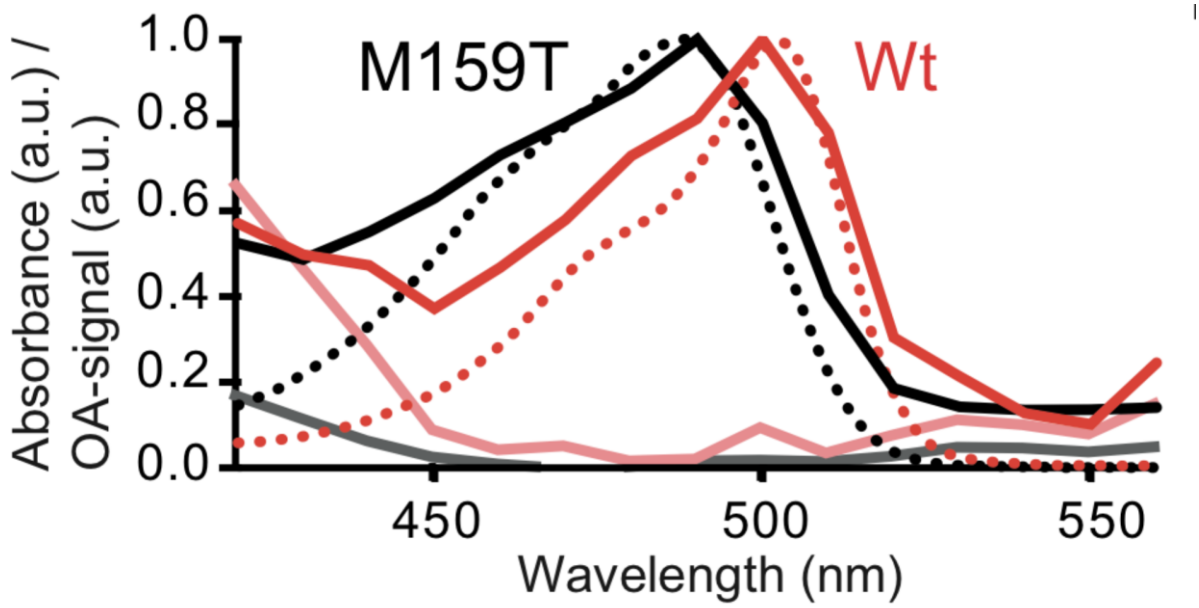

Figure 5.3: Optoacoustic spectra (solid lines) of Dronpa (red) and Dropna-M159T (black) in the equilibrium state and after prolonged illumination with 488 nm (light red and), as well as absorption spectra in the equilibrium state (dotted lines) as shown. Reproduced from Ref. [107].

5.3.2 Switching on and off optoacoustic spectra for RSFPs

To return the Dronpa completely back to dark state of absorption, the samples were continuously illuminated with 488 nm light for 5 minutes at a repetition rate of 50 Hz. The on-state spectra were measured started from 700 nm to 420 nm with each laser beam for 1 second of laser repetition at 50Hz, to avoid switching effect due to the light close to the UV range.

Figure 5.3 shows the absorbance and OA spectra of Dronpa and Dronpa-M159T in their equilibrium states (on-state), the observed good agreement between the modalities for both proteins and a spectral

shift between wildtype and variant of ~10 nm. Upon switching the proteins to the off-state using prolonged irradiation at 488 nm, the bathochrome peak, corresponding to the deprotonated chromophore, shows a reduced OA signal in agreement with previous fluorescence measurements [123]. With this OA imaging approach, synchronized OA spectra measurements between switching on and off were established, a technique challenging for fluorescent microscopy with very selectively filters/lasers and infeasible for conventional optical spectrometry.

5.3.3 Photocontrolled switching optoacoustic signal trajectories.

We next evaluated if defined OA signal time courses could be observed from photoswitching Dronpa with different photoswitching schedules. The 488 nm wavelength measurements were used as a readout/switch-off wavelength and 420 nm light was used to return proteins to their on-state (420 nm is the lowest available wavelength of the study's tunable Spitlight laser, though the optimal wavelength for on-switching would have been 405 nm). Here, we proposed three switching time courses for the on-off switching cycles, named 100-50, 200-50, 300-100. The first number indicates pulses for the off wavelength (488 nm) and the second the pulse number for the on wavelength (420 nm). Thus, in the 300-100 switching cycle trajectory, the illumination of laser was switched with a program between 300 pulses of 488 nm and 100 pulses of 420 nm.

Figure 5.4 displays raw photocontrolled OA signal trajectories with three photoswitching schedules of Dronpa-M159T. The signal for Dronpa-M159T increases to only 0.6% of that observed after 100 pulses of illumination at 420 nm, indicating that dark relaxation was negligible for the chosen photocontrol schedules. Thus, the on-switch cycle signals were recorded but neglected as they displayed no influence upon readout. The raw data showed that all off-switching cycles were able to switch back with 50 or 100 on-switching pulses, but longer illumination times created a stronger OA signal when it is switched back to 488 nm as a readout.

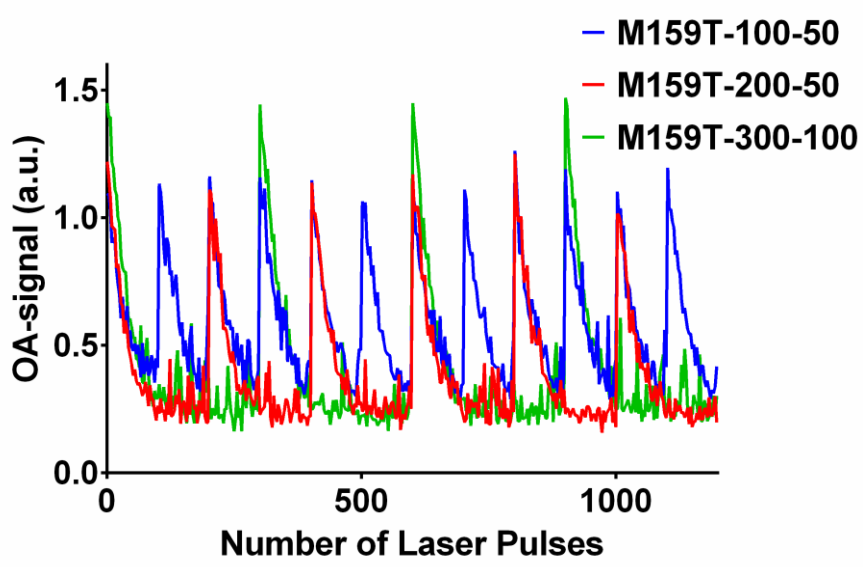

Figure 5.4: Raw switching cycles with photocontrolled OA signal trajectories of Dronpa-M159T with on-off cycles (100-50 200-50, 300-100 on-off switching cycles).

A more detailed comparison of the switching kinetics of the two types of proteins is shown in In Figure 5.5. Under the applied switching schedule, all OA signals were normalized to the peak of the first readout signal when illuminated with 488 nm light. The photocontrol schedule is visualized with light blue bars, indicating illumination with off-switching/read-out light at 488 nm, and violet bars denoting the number of laser pulses delivered at 420 nm to switch the proteins back on. The signal detected during illumination with 420 nm light was determined from the time courses.

As seen in Figure 5.5 (A), Dronpa-M159T showed a much faster signal decay with an approximately four-fold larger change in signal amplitude upon switching than the wild type Dronpa. Control over the switching behavior of the fast-switching Dronpa-M159T can be further exemplified by applying different photoswitching schedules varying in the number of laser pulses at the on- and off-switching wavelengths (Figure 5.5 (B) and 2(C)), as well as a more complex on-switching/readout scheme (Figure 5.5 (D)), which showcases flexibility in programming specific time profiles for the OA signals. In a control experiment, proteins were switched off completely with 488 nm illumination and left in the dark for approximately 30 sec to estimate the fraction of spontaneous relaxation to the equilibrium on-state. No signal increase was detected for wildtype Dronpa, consistent with its slow dark relaxation of $t_{1/2}$~840 min [120]. The recorded profiles of Dronpa-M159T showed no photobleaching or switching fatigue, a result that is in line with the published robustness of the protein.

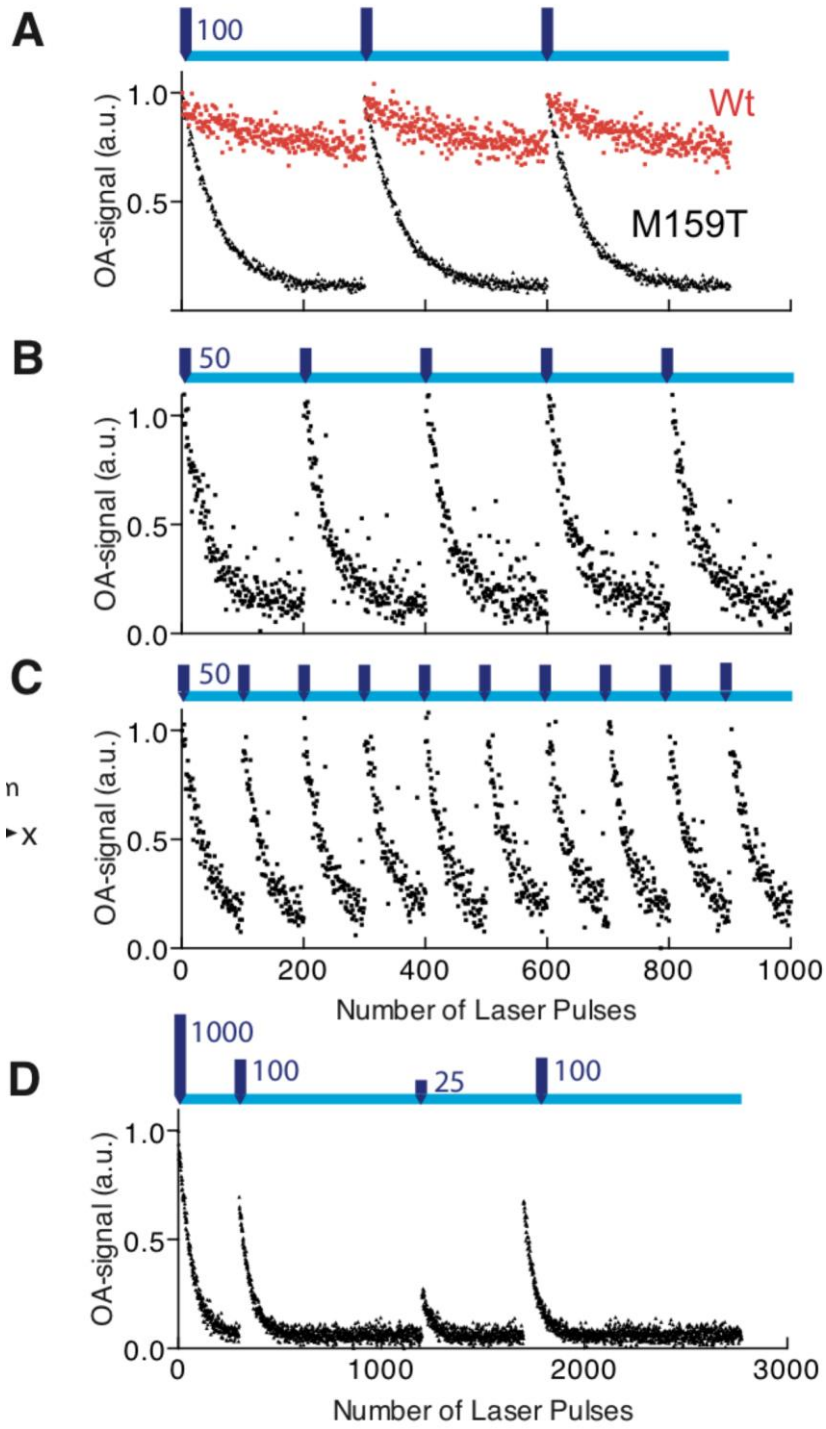

Figure 5.5: Normalized photocontrolled OA signal trajectories. (A) Comparison of signal time courses (60 averages) from Dronpa-Wt (red) and Dronpa-M159T (black). (B/C) Dronpa- M159T derived signal time courses (50 averages) under two periodic photocontrol schedules. (D) Example of a more complex switching schedule with Dronpa-M159T (20 averages). Laser pulse repetition frequency was 50 Hz for all experiments. Reproduced from Ref. [107].

5.3.4 Temporally unmixed multispectral optoacoustic tomography

Given the fact that the photocontrolled temporal signal profiles, we further investigated that profiles could be imaged with optoacoustic tomography system. First, only purified Dronpa-M159T (Mt), Dronpa-Wt (Wt)) were filled in tubings and positioned filled in tubes immersed in a water phantom positioned in a portable three-dimensional OA imaging system containing a transducer array with 256 ultrasonic elements [28].

We used 488 nm as readout/switch-off wavelength and 420 nm to switch the proteins back to their on-state. The reconstruction images were shown with maximum intensity projections (MIP) of Dornpa-M159T and Dronpa-Wt off-states with 1 pulse, 50 pulses, 100 pulses, and 200 pulses of illumination at 488 nm (Figure 5.6).

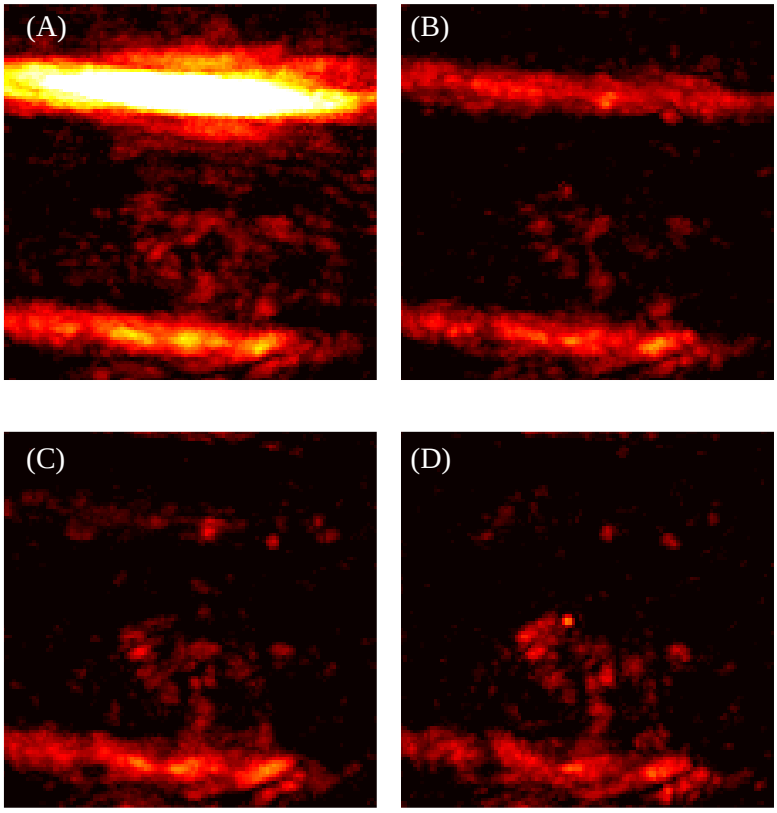

Figure 5.6: Maximum intensity projections (MIP) of three-dimensional reconstructions display Dronpa-M159T (upper) and Dronpa-Wt tubing when off switching was prolonged with (A) 1 pulse, (B) 50 pulses, (C) 100 pulses, and (D) 200 pulses of illumination at 488 nm. Notice that the noise in the center area comes from the ink in deeper layer. The ink was used here as the energy normalization reference of pulsed laser.

Furthermore, we were interested in how a temporal profile could be used to differentiate two Dronpa variants from the dominant absorber in the biological tissue. To this end, we imaged pure Dronpa proteins together with undiluted pig blood (~120 g/L of hemoglobin) filled in the middle tube. The photocontrol schedule contained 100 on-switching laser pulses at 420 nm (dark blue) followed by 300 nm readout/off switching.

The MIP display of reconstructed images is shown in Figure 5.7 A. Only the signal from the blood tubing was observed, an approximately 10-fold higher signal than the two Dronpa proteins (~70 μM) whose signal was only barely distinguishable from the background. However, with the temporal information contained in the photocontrolled OA signal time courses via temporal unmixing, proteins could be distinguished from one another and blood. Here, temporal unmixing was performed with the VCA algorithm (section 2.6.5). The corresponding SNRs were calculated from the indicated regions of interest (ROIs) with regions not containing sample (top and bottom ROIs) defined as background (Figure 5.7 C, black and red bars). The CNR for each Dronpa variant with respect to blood was computed by the absolute value of the differences in the averaged OA signals in ROIs containing the Dronpa proteins or blood, respectively. The resulting negative CNR values for the Dronpa variants with respect to blood are due to the fact that the blood signal was an order of magnitude higher than that of the proteins, with high CNRs in the resulting unmixed image (Figure 5.7 C).

Moreover, the robustness and applicability of temporal unmixing of photocontrolled OA signal trajectories were demonstrated with whole bacterial suspensions of *E. coli* expressing fast-switching Dronpa-M159T. Both suspensions were filled into tubes embedded in an agar phantom (Figure 5.7 B). The resulting temporally unmixed images also provided a clear contrast for Dronpa expressing *E. coli* with respect to blood.

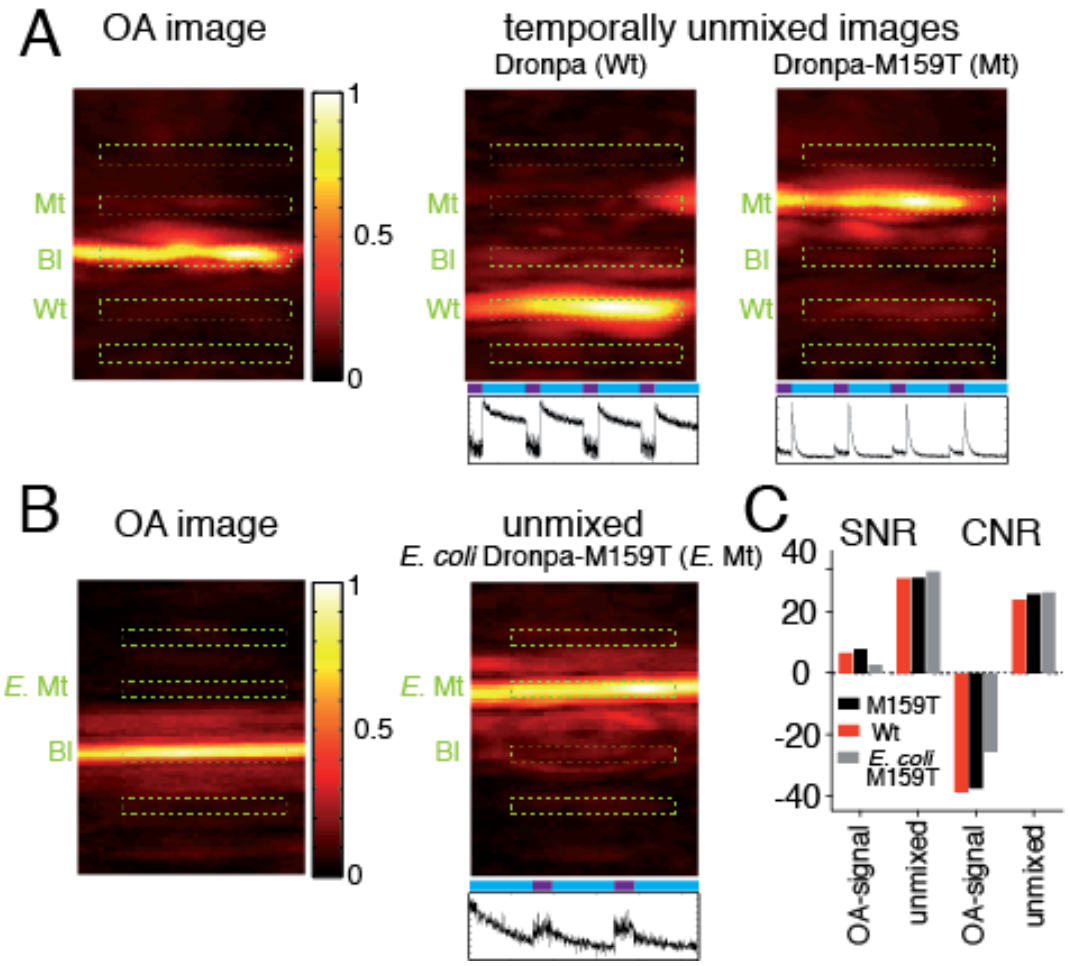

Figure 5.7: Temporal unmixing of Dronpa and its variant from background blood absorbers in optoacoustic images. (**A**) Purified Dronpa-M159T (Mt), Dronpa-Wt (Wt), as well as Blood (Bl) were filled in tubings and positioned on the imaging device. Maximum intensity projections of three-dimensional reconstructions are shown for the signals acquired at 488 nm (left panel). The unmixed images of the purified Wt (central panel) and Mt (right panel) are displayed together with the time profiles (containing signals recorded at both wavelengths) identified in the unmixing results. **(B)** *E. coli* suspension expressing Dronpa-M159T (*E.* Mt) were filled in tubings, embedded in an agar phantom and imaged together with blood in an analogous experiment. **(C)** Signal-to-noise ratio and contrast-to-noise ratio values for purified proteins (red and black bars) and *E. coli* suspension (gray bars) were calculated from the region of interest (ROIs) indicated in (A) and (B); the top and bottom ROI are defined as the background. The same photocontrol schedule as for the purified protein was used. Reproduced from [107].

5.4 Quantitative OA imaging with RSFP

Although we carefully investigated the potential photoswitching for OA imaging with the main absorber of blood in tissue, there are several aspects to be taken into account for *in vivo* applications. First, the time constants of the switching kinetics between the fluorescent and nonfluorescent states of a photoswitchable probes are a function of the incident photon numbers, hence, dependent on the light fluence distribution and irradiation power of the light source. Secondly, the photoswitching rates of FPs are significantly dependent the photophysics effects such as the pH, viscosity, and temperature of the cellular environment [123]. These environmental conditions are crucial for the sensitivity and efficiency of FPs, which may change fluorescent energy transfer, spectra shift, quantum yield, and the isomerization rates of the donor or acceptor. Therefore, understanding how photoswitching kinetics behave in different tissue conditions is important for the use of reversibly switchable FPs *in vivo*.

5.4.1 pH dependence of the photoswitching kinetics

Physiological and pathological processes are associated with a variety of intracellular or extracellular pH levels. A number of pathologies, such as metabolic disorders, inflammation, and solid rumors infections induce significant differences in the pH of surrounding tissues. Therefore, *in vivo* imaging applications are likely to prove useful for quantitative analysis and diagnosis given a knowledge of photoswitching kinetics at different pH levels.

One milliliter of 1.8 mg/mL Dronpa in solution was adjusted with acid buffer (pH 3), phosphate buffer (pH 9), and PBS (pH 7.4), to produce pH 5, pH 7.5, and pH 9 samples. The samples were prepared in the same concentrations and imaged with the same photocontrolled protocols, that is 500 pulses of 488 nm (off-switching) and 100 of 420 nm (on-switching). Each sample was imaged in the same tube of agar phantom and subsequently cleaned with flow channel which was washed in between measurements with 10 channel volumes of PBS such that no sample remained and the laser influence remained the same.

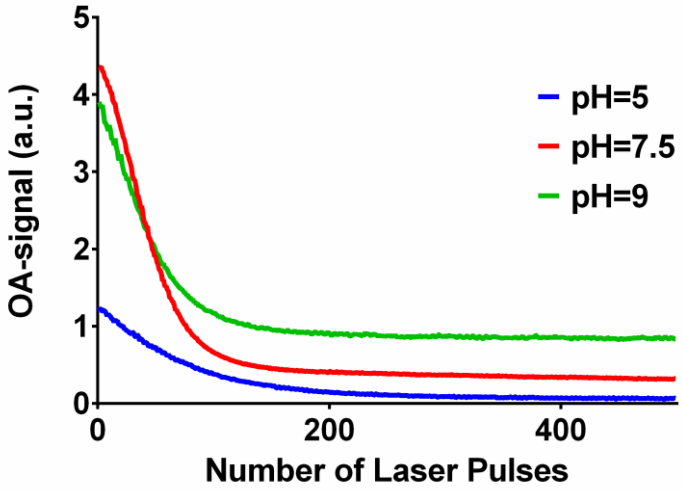

Figure 5.8: pH dependence of the photoswitching kinetics of Dronpa-M159T r at pH=5, pH 7.5 ,and pH9 with of the same concentration upon irradiation with 488 nm laser.

The temporal decay at different pH level is shown in Figure 5.8. Dronpa at neural pH levels not only exhibits the fast decay rate but also a strongest absorption at 488 nm. In contrast, the protein molecule at pH 5 shows a much slower decay and a smaller OA signal. This is in good agreement with the OA signal and the previous absorption spectra [123].

Different temporal decay behavior at different pH levels maybe explained by the three-state model in the previous research [123][124]. The distinct photoswitching properties of Dronpa might be related to the nature of the photoswitched protonated form (A_2) and the deprotonated form B, while the acid-induced (A_1) protonated form has no contribution (Figure 5.9). The appearance and disappearance of fluorescence and absorbance is the switch between the A_2 form and B form. This is a pure photo-induced reaction and not related to the acid-base equilibrium form A_1. Irradiation of the Dronpa solution at 488 nm causes a decrease in the absorption band of the protonated form (B) and an increase of A_2. This is reversed through irradiation with UV light. It is clear that photoswitched (A_2) and acid-induced (A_1) protonated forms are not interconvertible. However, the population of the A_1 and A_2 protonated form ratio is determined by the solution pH. Under neutral conditions, the A_1 form is negligible (only 0.4% of Dronpa molecules have A_1 form). Therefore, almost all molecules can be switched on and off, while the A_1 population is larger at pH 5. Such OA photoswitching kinetics of RSFPs in relation to pH shows the potential of pH contrast agents for *in vitro* and *in vivo* OA imaging.

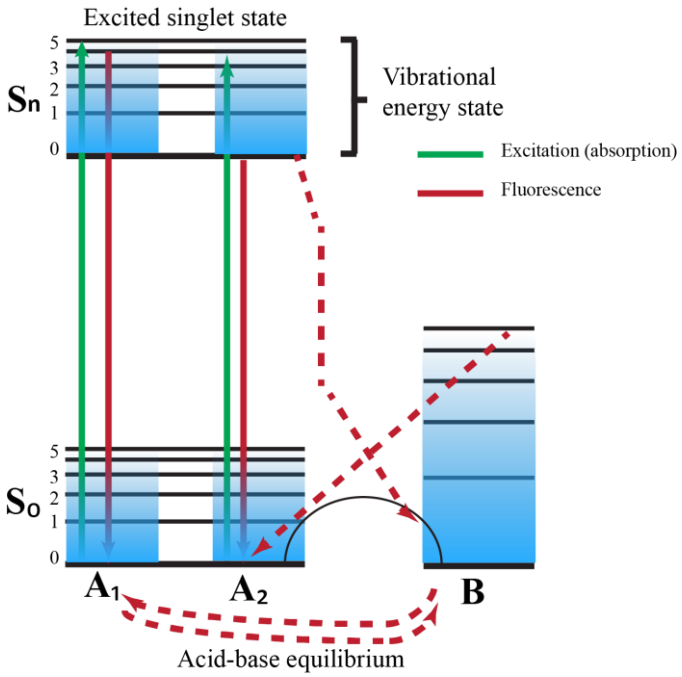

Figure 5.9: Schematic diagram of three-state photoswitching model of Dronpa: A1, the protonated form that originally exists in the sample; A2, the protonated form photoswitching; B, the deprotonated form.

5.4.2 Viscosity dependence

Though there are several different theories regarding the on-off photoswitching FPs [125], the general photoswitching mechanism is thought to arise from the *cis-trans* isomerization and/or protonation-deprotonating states of the chromophore and surrounding residue. To increase selectivity and sensitivity, environmental effects on the kinetics model through photochemical reactivity are a worthwhile venue of exploration. In addition to the pH of a biological environment, the surrounding viscosity may confine the flexibility of chromophores and affect the photoswitching abilities of RSFPs. A variety of functions and diseases are linked to variations in the fluid viscosity of solvent microenvironment. At a cellular level, for example, membrane and cytoplasmic viscosity changes in cell signaling modulation. On a macroscopic scale, diseases such as diabetes, hypertension, infarction, and aging are correlated to fluid viscosity changes in blood, plasma, or the lymphatic system [126].

Y. T. Kao et al. [127] first reported that increases in the viscosity of the solvent of the proteins can lead to a significant slowing down of fluorescent photoswitching kinetics. The study shows atha the fluorescence photoswitching decay rate is apparently viscosity dependent. To our knowledge, however, the viscosity effects on OA signal is still largely unexplored area.

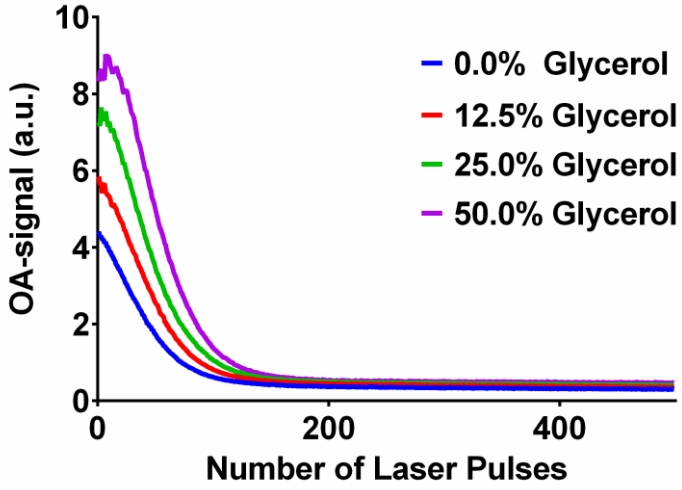

Figure 5.10: Viscosity dependence of the photoswitching kinetics of Dronpa.

One milliliter of 1.8 mg/mL Dronpa (pH=7.4) solution was prepared and mixed wtih 0%, 12.5%, 25%, 50% glycerol (vol/vol), the final concentration of protein maintained by adding PBS (pH 7.4). The samples were prepared with the same concentration and imaged with the same photocontrolled protocol, that is 500 pulses of 488 nm (off-switching) and 100 of 420 nm (on-switching). Each sample was imaged in the same tube of agar phantom and subsequently cleaned with flow channel and washed in between measurements with 10 channel volumes of PBS such that no sample remained and the laser influence remained the same. Figure 5.10 shows the decay trajectories of Dronpa at various viscosities (0 to 50%). The decay rate decreases with increasing solvent viscosity. Moreover, the OA signal peak of on switching cycles also indicates stronger OA intensity at higher viscosities.

5.4.3 Light fluence correction

As the described in chapter 2, reconstructed OA images are the products of light fluence, the wavelength-dependent molar extinction coefficient, and the concentration (equation 3.7). The goal of all the techniques implemented is to attain the quantitative mapping distribution of contrast agents. The absorption of chromophores in the tissue can be extracted with multispectral illumination acquisition, model-based reconstructions, and an unmixing processing. Yet, the quantitative discrimination of biological observation depends on the accurate intensity of possible spatial variations of illuminations and light attenuations. Thus photon penetration and deposited energy within an optically absorbing object must be accurately interpreted or measured. The light influences may, however, vary considerably for object depths and further depend on nondeterministic experimental factors, the heterogeneity of the object, excitation wavelengths, and illumination geometry. Light fluence correction is used in these cases, either with the help of light propagation models or processing

algorithms, e.g., by Monte Carlo simulation [128], finite-element solver [129], iterative inversion algorithm [130], or unmixing of multispectral datasets [49]. Alternatively, it can be estimated by introducing incorporating an OA setup with other optical image modalities, such as fluorescence and diffuse optics. While these techniques improve quantitative chromophore concentration information, the practical performance remains limited due to the unknown optical properties of heterogeneous living tissue [131].

The The RSFP Dronpa shows another promising potential for light fluence correction. The time constants for transitions between the fluorescent (high absorption) and nonfluorescent (low absorption) states of the photoswitching kinetics are a function of the number of incident photons. Hence, the photoswitching decay of the OA signal depends on the light fluence distribution, but not on the concentration of the protein. Therefore, the spatial dependence of the signal decay rate can potentially be exploited to correct for light fluence distribution. This can be clearly seen from Figure 5.6. The spatial distribution of the OA signal intensity is not homogenous though the same concentration of proteins is in the tubing. This further indicates that the temporal signal decay might imply spatial light fluence. The correlation between fluence distribution and photoswitching rate was first investigated. The exponential-like fitting decay rate of different positions was extracted, thus the light fluence of different location/depth could be corrected with this normalization of decay rate. For more details concerning the experiments and mathematical processing, see Ref [108].

To prove this concept, two tubings containing Dronpa-M159T at an identical concentration of 1.8 mg/mL were embedded in an agar phantom with a 6% intralipid solution to mimic a representative scattering coefficient in biological tissues and imaged with a volumetric three-dimensional OA imaging system.

A cross section of the three-dimensional reconstruction obtained at 488 nm after fully switching on the proteins is shown in Figure 5.11(a). Despite the same concentration of Dronpa M159T contained in the two tubes (labeled T1 and T2), the signal from the deeper position is strongly reduced due to the different illumination conditions. An additional mirrored structure (labeled R) can be further identified in the original image in Figure 5.11 (a), which most likely represents an artifact from acoustic reflections on the surface of the plastic tubing. The actual OA temporal profiles at different location in the volume were then used to fit. The decay rate of the entire imaged volume was subsequently fitted with a median filter over 3×3×3 voxels. Figure 5.11 (c) displays the corresponding filtered decay rate for the image of the cross section. The fitted decay rate is only representative of fluence inside the tubes where the probe is located. Figure 5.11 (b) shows the fluence correction for the image of the cross section, normalizing Figure 5.11 (c). Three-dimensional views of the OA images for the fully activated protein before and after normalization are shown in Figure 5.11 (d) and (e), respectively.

Note, a threshold mask, corresponding to points for which both the decay rate and the normalized image are higher, was applied for a better visualization of the normalized three-dimensional image.

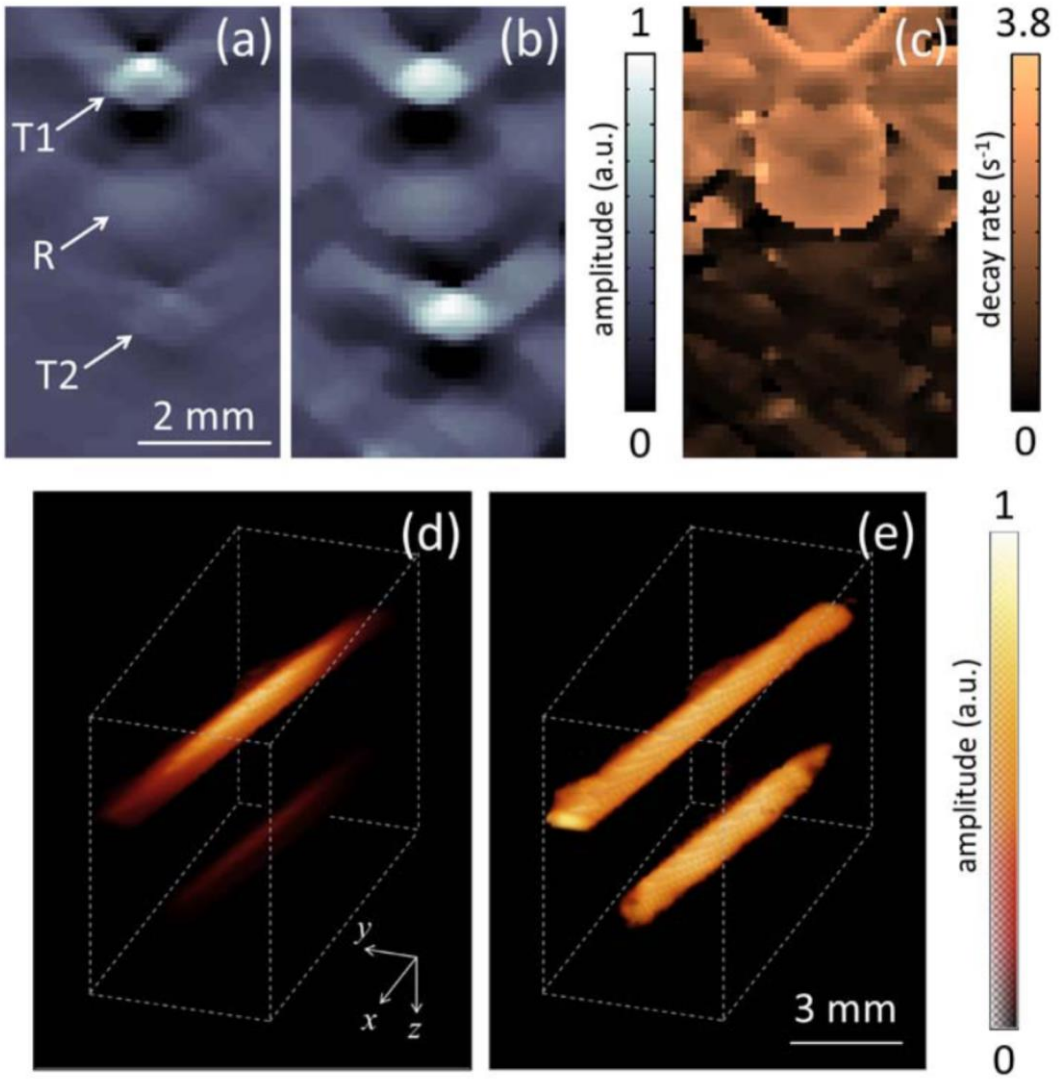

Figure 5.11: Cross section display of the three-dimensional reconstruction for the fully activated protein (a) before and (b) after light fluence correction. The result of normalization is corrected by the estimated light fluence distribution is displayed in (c). The samples were filled in two tubings, labeled with T1 and T2 in the image, while an artifact structure (R) was identified. Three-dimensional optoacoustic image views of the fully activated protein (d) before and (e) after normalizing with the estimated light fluence. Reproduced from Ref. [108].

In this example, we showed that both in two-dimensional and three-dimensional view, the deeper tubing thus was able to recover approximately the same OA intensity based on temporally unmixed multispectral OA tomography. Thus the proposed new light compensation approach is promising for light fluence correction in the scattering biological tissue.

5.4.4 Other aspects

From these preliminary phantom measurements, quantifying photoswitching rates can be corrected by incorporating pH, viscosity, and light influence changes in the microenvironment of a biological system. On the other hand, the RSFP Dronpa shows potential for achieving quantitative visualization of pH and viscosity in *in vivo* deep tissue due to a rapid response time and the high spatial resolution of OA imaging. There are additional aspects to consider for *in vivo* OA imaging.

5.4.4.1 Motion correction

In terms of *in vivo* imaging, the expressing cells with FP application would be limited by the low concentration and relatively weak absorption of a protein compared to background. As the previous results showed temporal unmixing proteins could be used to distinguish them from one another with increase CNR from blood sample, which generates an order of magnitude higher OA signal. However, animal breathing and heartbeats may induce periodic patterns into the background signal if the animal maintains such a state. Thus, motion correction is necessary if the sensitivity of RSFPs is not high enough.

Animal motion can be measured by monitoring physiological parameters and motion eliminating correction algorithms can be used in conventional imaging modalities. The tuMSOT method provides several solutions to decrease motion artifacts. First, animal motion is less statistically related or irrelevant to the switching cycles of laser wavelengths. Hence, multispectral measurements can minimize motion with temporal patterns. Second, the photocontrolled programing of switching photons in different regions can identify noise patterns regardless of switching kinetics. Moreover, averaging images over multiple switching cycles for measurements can directly reduce animal motion.

5.4.4.2 Nonlinear light fluence dependence

The OA signal amplitude of a molecular absorber is correlated to laser fluence, the absorption coefficient, temperature, and medium parameters. Most quantitative OA studies assume a linear dependence between the OA signal and the light fluence. This is true only at incident photon intensities much smaller than the saturation intensity [132]. Absorbing chromophores first exhibit gradual linear increases when the light fluence is low, and nonlinear signal amplification and absorption saturation or even decreasing as energy intensity increases [133]. The energy barrier for photochromic switching of Dronpa and variants is in the range of 1-100 mJ/cm^2, while the laser pulse fluence on the surface used in the current MSOT system is relatively low (under 20 mJ/cm^2). However, in the case of OA microscopy system, it would induce nonlinear behavior of this absorber as

the laser fluence can reach much higher laser fluence ~2J/cm^2. The nonlinear light fluence dependence in this case has to be investigated both for fluorescence and absorption signal changes. Multi-photon excitation or two-photon photoswitching processes with NIR range wavelength is also feasible for Dronpa proteins. As a consequence of nonlinear excitation by two (or more) simultaneous incident photons, the probability of nonlinear intensity dependence of absorption and fluorescence is high. The integration of nonlinear/saturated OA and fluorescent responses could be exploited to further increase resolution [134]. Therefore, for OA imaging technique combined with RSFPs, the nonlinear fluence effects can be easily extended to increase the sensitivity of OA detection.

5.4.4.3 Modulation of lifetime

Besides the pulse photon energy, the OA signal generation may vary with different pulse widths. For example, instead of a nanosecond, the oxyhaemoglobin is shown to be saturated to half the absorption when excited with a picosecond pulse [135]. As described by the Jablonski Diagram (Figure 2.1), the photon absorption process of a fluorophore is in the time scale of a femtosecond (10^{-15} s) and the timescale of fluorescence from an excited state to a ground state is roughly a nanosecond (10^{-9} to 10^{-7} s). The OA signal generation of a fluorescent molecule is significantly lower than chromoproteins. A portion of excited state proteins would not absorb photons, thus exhibiting no OA signal during long relaxation times (nanoseconds). In contrast, the vibrational relaxations of chromoproteins that do not fluoresce are more likely to operate on a picosecond timescale, leading to less depopulation of the ground state and more efficient thermalization for OA signal generation.

The energy transfer mechanism of switchable fluorescent protein could possibly be measured by the modulation of lifetime, rather than time-dependent photoswitching kinetics for absorption and emission. The amplitude of optoacoustic response and fluorescence emission are related to time delay of excitation pulses [136]. By selecting double-pulse illumination, one pulse to excite the fluorescence emission, and a second pulse with a wavelength that coincides with the spectral region of maximum absorption, stimulated emission can be induced. The difference in the OA signal amplitude measured using simultaneous and time-delayed pump-probe pulse provides a contrast mechanism that is unique to fluorophores because contributions from non-fluorescent chromophores are removed.

5.4.4.4 Synthetic dye

In addition to reversibly switchable FPs, synthetic dyes can also be alternative agents in OA imaging. For example, rhodamine NN dyes can be in a nonfluorescent state with the incorporation of a photochemical labile group, while a photosensitive masking group or molecular cage can be cleaved through irradiation with near-UV light, thereby rendering the dye fluorescent [137]. Similar to the photoactivatable FPs, the commercial Abberior dye CAGE 552 dye is in the caged state (absorption

peak 300 nm) in resting state and can be activated with UV light (360-440 nm) to the uncaged state (absorption peak 552 nm), becoming fluorescent (Figure 5.12 a).

(a) (b)

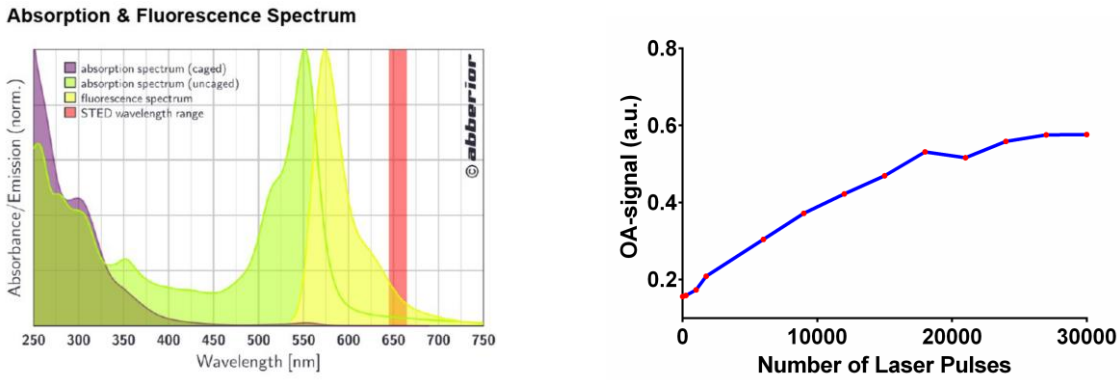

Figure 5.12: (a) Abberior CAGE 552 specification. (b) Optoacoustic signal with 420 nm illumination pulses. The red dot is the OA signal readout when switched to 552 nm for 50 pulses and then switched to 420 nm illuminations. For more details, see http://www.abberior.com/shop/Labels-by-Application/Confocal-Epi-SIM/Abberior-CAGE-552::13.html

The OA spectrometer system was used to measure CAGE 552 dye (Abberior GmbH, Göttingen, Germany) filled in the flow chip. The photoactivatable OA signal increased with the cage state illumination (420 nm) time. The red dot indicates the OA signal readout when the laser was switched to 50 pulses of 552 nm illumination for the uncaged state. The increasing OA signal indicates a promising application with the implementation of synthetic dyes (Figure 5.12 b). However, this fluorescent rhodamine dye and its derivatives are not reversibly switchable contrast agents, limiting its applications in OA imaging.

5.5 Summary and conclusion

In general, tuMSOT requires a photoabsorbing contrast agent whose photophysical properties can be controlled with external control commands, such as photons, to program temporal signal profiles of the OA contrast agent which can be differentiated from time-varying background signals. Instead, the reversibility of photochromic molecules such as RSFPs allows for more complex programmed signal trajectories with many switching cycles.

We demonstrated that the photoresponsive, photophysical properties of certain RSFPs are suitable for obtaining programmed, time-varying OA signals. With the RSFP Dronpa and its variant Dronpa-M159T, we showed that temporal unmixing of their simultaneously switched OA signal trajectories

could discriminate well between the proteins despite their similar spectral properties. Both RSFPs could also be unmixed with high CNR from strongly absorbing blood which generates a much larger OA signal. These switchable proteins and their (far) red-shifted variants can thus serve as high-contrast OA reporter genes for future *in vivo* imaging of *e.g.* zebrafish or mouse models via tuMSOT. In addition to common spectral unmixing of OA signals, exploiting temporal information makes great use of the high frame rate of MSOT systems and expands the additional detection and differentiation capabilities to OA imaging.

Furthermore, photophysics effects such as pH and viscosity were studied. The photoswitching kinetics of OA signal behavior in different tissue conditions provides valuable information for quantitative reversibly switchable FPs in *in vivo* environments. The distribution of light fluence in biological tissues can be effectively corrected by exploiting the fluence-dependent transition times of photoswitchable probes. In addition, temporal unmixing further enables determinations of the spatial distribution of photoswitchable agents on a temporal resolution scale, limited by the time required for the activation-deactivation cycle [107]. Furthermore, other possible effects such as motion correction, nonlinear light fluence dependence, modulation of lifetime, and synthetic dyes were briefly discussed. Exploring and optimizing the large class of synthetic and genetically encoded photochromic molecules, especially in the NIR, in conjunction with optimized photocontrol command schedules, could make tuMSOT a new standard for high contrast molecular OA imaging.

Chapter 6 Ultrasound-mediated blood-brain barrier (BBB) opening for contrast agent delivery for brain imaging

6.1 Introduction

The motivation of this research is to develop new types of contrast agents for high spatial resolution and noninvasive imaging, in particularly in a mouse model. As briefly discussed, contrast agent-based molecular imaging strategies have several limitations. First, many agents are laborious or expensive to synthesize and modify. Second, the expression level of ligands must reach an adequate concentration for a sufficient length of time required for imaging methods. Finally, but most importantly, these compounds must be delivered to the intended targets, especially to cell or compartment-specific targets. Overcoming delivery barriers (vascular, interstitial, cell membranes) is a challenging task. Even agents with low molecular weight may not cross barriers and reach cellular compartments [138][139]. Contrast agent delivery is particularly difficult for neuroimaging research due to the limited permeability of the BBB. Therefore, it is essential to study techniques to open the BBB for the delivery of exogenous contrast agents.

The unfocused US-mediated BBB opening strategy, which is capable of delivering various sizes of molecules in a large volume to the brain, is introduced in this chapter. A brief introduction to conventional BBB opening approaches and an explanation of our US-mediated BBB opening method is provided. Several types of agents were administered to determine factors of molecular size, volume and distribution homogeneity with this BBB opening technology. The potential applications in brain labeling, functional brain mapping, and drug delivery with MRI and OA imaging are presented and further technological optimizations are discussed.

6.2 The blood-brain barrier

From the perspective of neuroscience, molecular contrast agents are essential tools to extract information about neural physiology that goes beyond structural neuroimaging or hemodynamics imaging. Moreover, there is a growing interest in studying neurovascular units, composed of neurons,

glia cells, and micro-vessels. However, the delivery of synthetic/biosynthetic molecules over the BBB into brain tissue is a major challenge as most molecules cannot get across the BBB to the activated neuron units. On the other hand, despite advances and breakthroughs in drug development, efforts towards targeting and treating central nervous system (CNS) diseases are inhibited by the BBB. Global pharmaceutical companies are pursuing drugs for the brain that cross the BBB, as the great majority of drugs do not cross the brain capillary walls of the brain [140]. The BBB (Figure 6.) is a selective barrier formed by endothelial cells, astrocyte end-feet, and pericytes. The complex, tight junction between adjacent endothelial cells impedes the influx of most molecules.

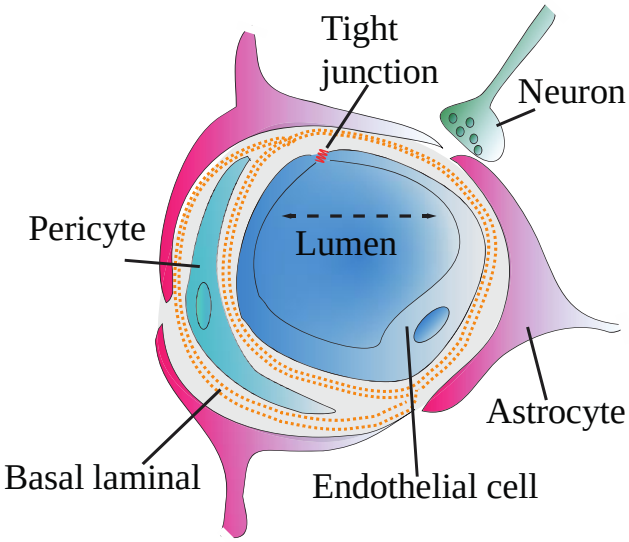

Figure 6.1 Schematic lateral cross-section drawing of the blood-brain barrier (BBB). The BBB is formed by endothelial cells surrounding cerebral capillaries. Cerebral endothelial cells form complex, tight junctions produced from the interaction of several trans-membrane proteins effectively seal the paracellular pathway. These tight junctions make the brain inaccessible for hydrophilic molecules unless transport pathways of the BBB that regulate the microenvironment of the brain transfer them. In addition to endothelial cells, the BBB is composed of capillary, basal lamina, astrocyte end-feet, and pericytes embedded in the basement membrane. Astrocytes provide the cellular link to the neurons.

In terms of molecules types, only small lipophilic gases such as O_2 and CO_2 can diffuse freely through the lipid membranes, and nutrients such as glucose and amino acids can enter the brain via active transport. While the BBB maintains a precisely regulated microenvironment by excluding potentially harmful compounds, it also prevents the passage of the most contrast agents used for *in vivo* brain imaging. In terms of molecule size, almost 98% small molecules (Molecular mass, M_r <400-500 Dalton) and 100% of large-molecule drugs cannot cross the BBB [140]. To better understand

neuroimaging and neurological diseases in a mouse model, it is beneficial to develop a technique to open the BBB quickly and noninvasively for various imaging methods.

6.3 Trans-BBB delivery strategies

6.3.1 Traditional approaches for BBB opening

A successful agent-delivery system to the brain should consider efficacy, safety, non-invasiveness, cost, and implementation time. Much effort has been made to develop agent-delivery approaches with maximum agent targeting and minimal side effects. These approaches can be categorized in three basic forms. One alters the chemical properties of molecules with suitable lipid solubility, hydrogen bonding, and molecular weight. The second strategy utilizes the function of transporters such as receptor-mediated transporter, active efflux transporter for small water-soluble nutrients, and carrier-mediated transporter for larger molecules. The third focuses on the mechanical and/or chemical disruption of the BBB.

The chemical modification-based strategy is problematic due to the fact that the BBB consistently responds to lipid-soluble small molecules and the molecular lipidization and may bring undesirable pharmacokinetic effects such as nonspecific plasma protein binding. The biology-based strategy takes advantage of the endogenous BBB transporter which acts a molecular 'Trojan horse' to ferry molecules [140][141]. Hence, advanced knowledge that combing drug discovery and drug targeting must be undertaken in order to develop genetically engineered fusion proteins or antibodies to endogenous carrier.

Alternatively, the BBB can be disrupted temporally and reversibly by chemical or physical means to allow agents to penetrate the brain. The chemical disruptions method is based on intra-arterial infusion of hyperosmotic solution like mannitol [142], vasoactive agents [143], or other solutions [144] to break the tight junctions. The dilation and contraction of the vessels will increase uptake of plasma albumin and other proteins which are harmful to neurons [145]. Moreover, this time consuming technique is very difficult to be performed in mice and still technically challenging in rats or rabbits [146].

Besides modifying or packaging the compounds themselves, US-mediated techniques can achieve transient trans-BBB delivery of unmodified CAs based on actuating *i.v.* injected microbubbles with resonant pressure waves [147][148]. This method also holds great potential for clinical applications in targeted drug delivery to the nonhuman primates brains [149] once its physiological effects on cells is sufficiently be understood to avoid side effects.

6.3.2 Ultrasound technology for the BBB opening

Ultrasound technology is now widespread and used as a safe, noninvasive diagnostic imaging method. By selecting US parameters, spatiotemporal control of US energy can induce local biological effects in deep tissue by delivery acoustical energy to a focal spot in the body. Instead of acquiring echoes generated from tissue interfaces, US based BBB opening strategies utilize the same idea begind ultrasonic waves propagation but deposits acoustic power to induce physical effects, i.e., mechanical and thermal effects, which increase the BBB permeability. In 1955, Barnard et al. proved BBB permeability with acoustic waves in a cat brain [150] with negligible damage to the parenchyma. Since then, scientist have attempted several US parameters to produce targeted and consistent BBB disruption without visible damage of the brain parenchyma [151][152]. However, the US energy needed is at or near ablation intensities as the result of strong skull attenuation. Compared to the attenuation coefficient of tissue in brain (~ 0.5 dB/cm/MHz), the skull bone attenuation is at least one order higher [153]. Therefore, removing part of the skull (craniotomy) to create an acoustic window to avoid US beam distortion and overheating is a common technique in practice.

6.4 BBB opening with ultrasound and microbubbles

6.4.1 Introduction

Instead of using the US technology described above to generate bubbles in brain blood vessels, in 2001 Hynynen et al. suggested the use of focused US in combination with commercially available US contrast agents to encapsulate gas-filled microbubbles [154]. This landmark study demonstrated the opening the BBB with much lower acoustic energy and an intact skull without the risk of overheating. The details of this technique are introduced in the following section.

6.4.2 The interaction between focused ultrasound and microbubbles

With a focused US, the BBB has been viably opened in various animal models including mice, rats, rabbits, pigs, and monkey [149][154][155][156][157]. This combination has been shown to be the most promising strategy to deliver agents to the brain without brain tissue damage.

Although the exact mechanisms of the US-mediated microbubble interaction for opening the BBB remain unknown, the cavitation of microbubbles and mechanical effects are believed to play the most important roles [159]. When alternating positive and negative pressure from the acoustic field is applied in the liquid medium, gaseous bubbles undergo rapid volume oscillation, growth, and collapse. Both stable and inertial cavitation in medium can produce significant mechanical and chemical effects which increase the permeability to the surrounding endothelial cells [158][159]. Those endothelium

cells response to shear stress plays a critical role in BBB vascular homeostasis and pathophysiology [160]. The stable oscillation (stable cavitation) of bubbles can generate shears stress on nearby cells by microstreaming (Figure 6.1). In addition, stretch-sensitive or mechanosensitive ions channels may also open when bubbles make contact with endothelium cells. Under high acoustic pressure amplitudes that surpass the threshold, the bubbles grow rapidly and collapse (inertial cavitation), thus inducing localized temperature increases, strong shock waves, high-velocity micro-jets, and chemical effects. Compared to stable cavitation, inertial cavitation shows a more significant bio-effect due to bubble collapse. However, it is reported that these effects may be necessary for BBB openings with smaller diameter (1-2 μm) and not necessary for BBB disruptions with microbubbles for larger diameter (4-5 and 6-8 μm) [161][162].

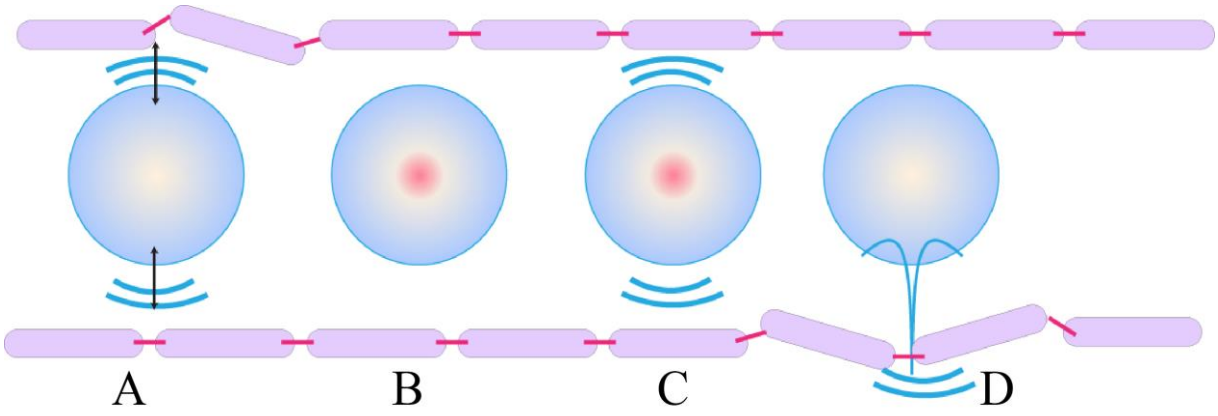

Figure 6.1: Possible mechanisms for ultrasound-mediated microbubbles BBB opening. A) Acoustic streaming: oscillations of bubble volume from acoustic pulsation around a medium generate small-scale microstreaming that will induce shear stress on the membrane. B) Sonochemistry: the collapse of hot bubbles induces chemical changes in the microenvironment. C) Shock waves: shock waves formed by the sudden collapse of cavitation bubble are able to increase the permeability of cell membranes. D) Liquid micro-jets: formation of high-velocity fluid micro-jets result from collapsed bubble near surface.

On a cellular level, evidence from immunocytochemistry indicates an increased number of vesicle, fenestration, channel formation, and tight junction openings of microvascular endothelia after US-mediated microbubble sonication [163][164]. Distinct acoustic pressure and microbubble diameter combinations have also been found to increase BBB permeability by at least 100% [165].

6.4.3 Ultrasound system

The interaction between microbubbles and US exposure is strongly affected by several sonication and microbubble parameters. The BBB opening is strongly dependent on acoustic parameters, including US frequency, peak rarefactional pressure, pulse length (PL), pulse repetition frequency (PRF), and treatment time. The effects of microbubble, such as bubble size, concentration, total volume, and injection duration, as well as the lifetime of microbubbles, should also be considered.

6.4.3.1 Center frequency selection

Center frequency selection is one of the key elements for microbubble oscillation in the vessels. Regardless of the shell property, the resonance frequency is inversely proportional to the bubble diameter when the other parameters remain the same. However, the bubbles are confined to compliable vessels and strongly affected by their boundaries and rigidity. The resonant frequency of a bubble is significantly determined by the vessel diameter and length [166]. Table 6.1 lists the natural frequency of nonlinear oscillation when a microbubble is in a confined compliant vessel with 10 μm diameter [167]. This diameter is chosen as the average vessel diameter in a mouse brain cortex microvascular network is 10.5 ± 3.4 μm [168] and the morphometric analysis indicates that cerebral capillaries are 4-8 μm in diameter [169]. Generally speaking, skull attenuation and aberration are less sensitive to lower frequency US waves. Thus, employing low frequencies can alleviate skull attenuation and enhance the effect of cavitation [170]. To generate efficient cavitation while avoiding thermal damage to brain tissue, minimal sonication energy (lower acoustic intensity, pulse duration, and treatment time) have to be empirically determined once a frequency is determined.

Based on microbubble size (mean diameter of 2-4 μm), we selected the corresponding resonance frequency (Table 6.1) with a customized unfocused transducer with a center frequency of 2MHz (Sonic Concepts. Inc., Bothell WA, USA). This one element flat transducer has an active diameter of 20 mm with a bandwidth of 1.4–2.6 MHz and a focal depth from 125–135 mm. The maximum-pulsed power can reach 300 W (10% duty cycle). The large diameter unfocused transducer was chosen to cover a large extent of the mouse brain with minimal influence on brain physiology.

Table 6.1: The natural resonance frequency of different size microbubble when the bubble is confined in the compliable 10 μm diameter vessels.

Diameter (μm)	Resonance frequency (MHz)
2	3.92
4	1.93
6	1.41
8	1.26

6.4.3.2 Acoustic pressure mapping of ultrasound beam

To characterize the unfocused transducer, several instruments are used in acoustic pressure mapping (Figure 6.2). The unfocused transducer was connected to a 53dB RF amplifier (NP-2519, NP Technologies, Inc. Newbury Park, Canada) driven by a function generator (Rigol DG1022, Beaverton, USA). An external 50-Ohm impedance matching network was used for transducer impedance matching with the amplifier. The unfocused transducer was positioned through a polycarbonate-made coupling cone filled with degassed water. Peak-rarefaction acoustic pressures were detected with a 0.5 mm diameter hydrophone needle (Precision Acoustics, Dorchester, UK) connected to a digitizer via a preamplifier and DC coupler. The hydrophone was held by a 3D positioning system which consists of three linear translation stages (MTS50/M- Z8, Thorlabs GmbH, Karlsfeld, Germany) for the X-Y-Z planes and a rotary stepper motor (PRM1/MZ8, Thorlabs GmbH, Karlsfeld, Germany). The stages were suspended from an optical platform above the water tank (Figure 6.3). The designed coupling cone was filled with degassed water for acoustic coupling between the transducer and the exit plane, where the head of the animal is placed for sonication. The exit plane of the cone was kept flat with plastic wrap and the distance to transduce plane was the focal length of transducer. All data was acquired and processed with custom-written MATLAB routines (Mathworks Inc., Natick, MA, USA).

In our case, we examined the maximize sonication of the whole brain with one element transducer so that the BBB could be opened in a maximally large volume of the brain. Therefore, acoustic pressure distribution is the critical US parameter for the BBB opening.

Figure 6.4 shows different acoustic beam pressure pattern mapping (a) without and (b) with the coupling cone at the exit plane. The acoustic pressure profile of x-axis was plotted (y = 0 cm). Notice the inhomogeneous distribution of the US beam caused by the coupling cone.

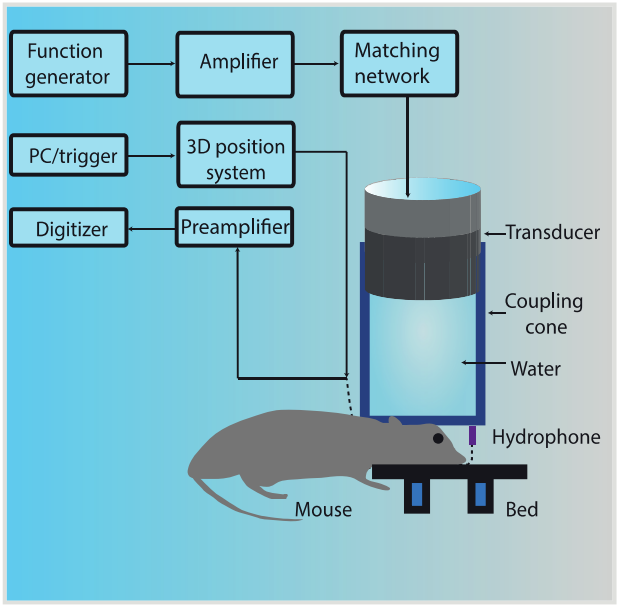

Figure 6.2: Illustration of the experimental setup for acoustic pressure measurements and the BBB opening. The unfocused transducer is connected to a 53dB RF amplifier driven by a function generator. An external 50-Ohm impedance matching network is used for transducer impedance matching. The unfocused transducer is positioned through a polycarbonate-made coupling cone filled with degassed water. Acoustic pressures are detected with a 0.5 mm diameter hydrophone needle connected to a digitizer via a preamplifier and DC coupler. A 3D positioning system is used to acquire acoustic pressure mapping. For *in vivo* experiments, the hydrophone unit is removed once US field calibration is complete.

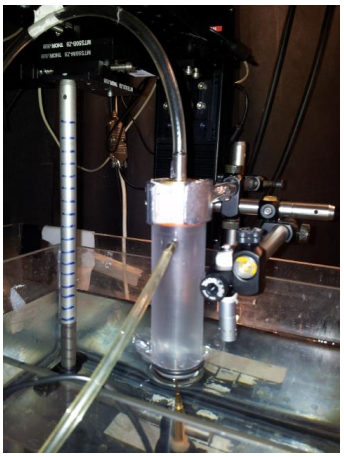

Figure 6.3: Picture of hydrophone immersed in water tank for acoustic pressure measurements. The transducer is placed in a coupling cone, which is filled with degassed water for acoustic coupling.

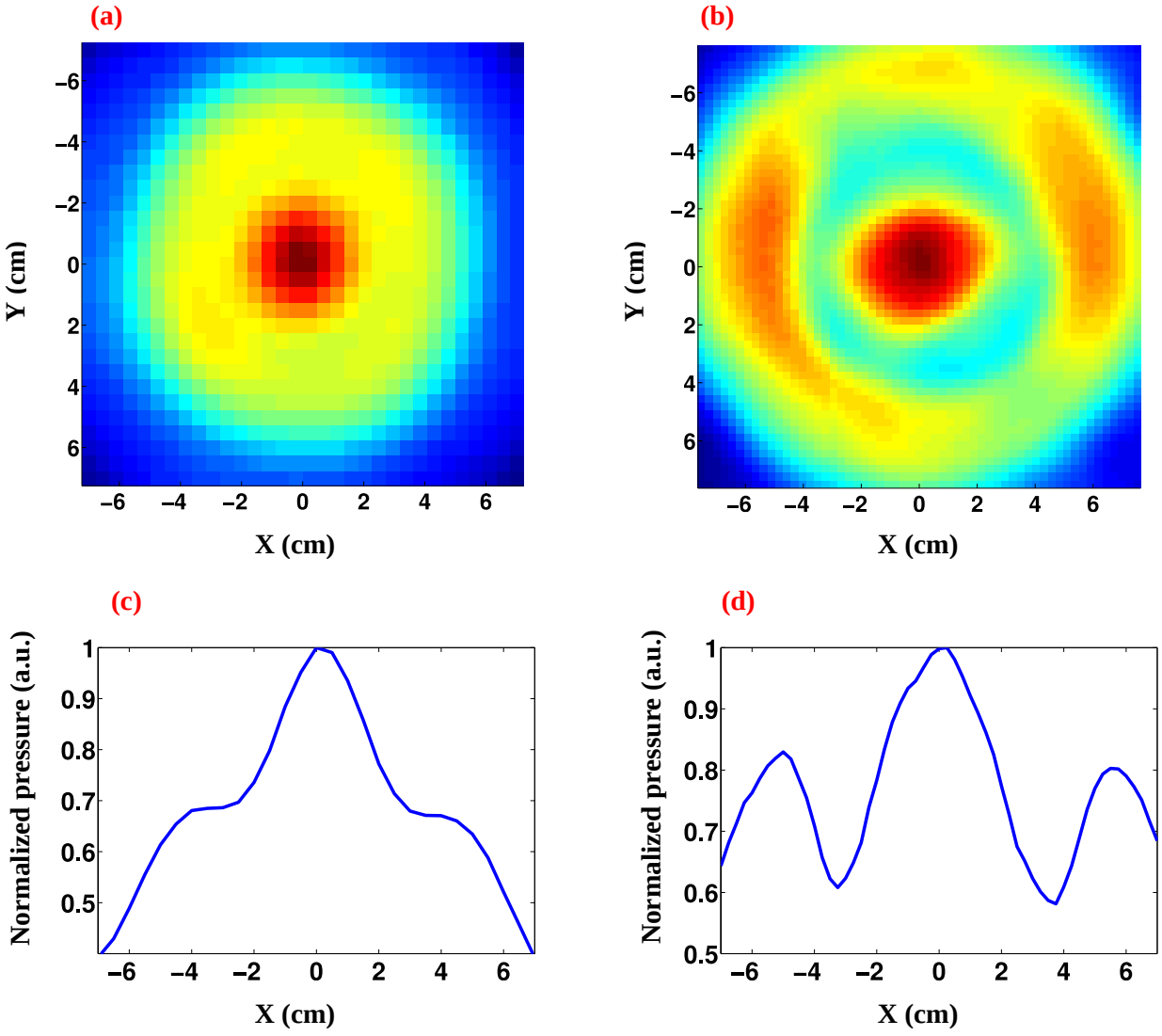

Figure 6.4: Acoustic pressure map distribution (a) without and (b) with the coupling cone. The corresponding pressure profile for the x axis across the center (y=0 cm) are plotted in (c) and (d). Note that the absolute acoustic pressures of different depth are used for normalization.

6.4.4 Pulse sequence parameters for BBB opening

The typical pulse sequence used to drive sonication consists of acoustic pressure at a center frequency and a pulse length repeated at a pulse repetition frequency (PRF). A commonly employed US transducer is in the center frequency in the range of 0.5-5MHz. Figure 6.5 shows a parabolic relationship between the voltage input (mVpp) and the average acoustic power produced by the transducer. This US field calibration is useful for input functional generator setting selection once the desired acoustic pressure output is defined.

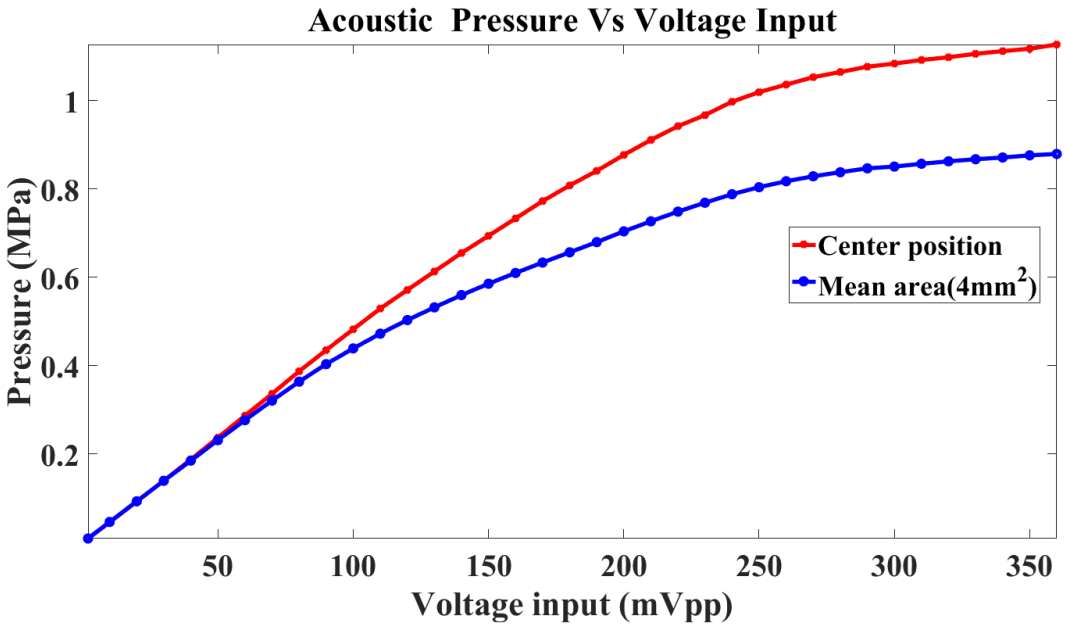

Figure 6.5: The relationship between voltage input and the acoustic pressure output. From acoustic pressure mapping in Figure 6.5 (b), the 4 mm^2 area around the focus center was selected. Here we consider the 2 mm × 2 mm area as the mean acoustic pressure output.

6.4.5 Microbubbles

To achieve reproducible and consistent cavitation environments *in vivo*, not only the correct pressure distribution is important, but also the microbubble size distribution.

Table 6.2 lists all commercial microbubbles that have been studied for the BBB opening. However, only the contrast agent SonoVue is available in Europe. These US contrast agents are composed of a protein (albumin) or lipid shell and a stabilized gas core. SonoVue is a suspension that contains stabilized sulphur hexafluoride (S_3F_6) gas, an extremely stable inert gas that does not interact with other molecules. SonoVue microbubbles are small enough to pass through and avoid be trapped in the capillary vasculature because they have a mean diameter of 2.5 μm and 90% of the bubbles are smaller than 8 μm [172]. It can reconstitute to high bubble concentration (up to 5×10^8 bubbles/mL) with an elimination half-life up to 6 minutes [173].

Microbubbles plays a key component for low acoustic pressure (1 MPa) since there is no BBB opening with the same sonication amplitude without the presence of microbubbles in vasculatures [154]. The US pressure threshold is reported to be microbubble size dependent. The necessary

sonication is relatively higher when the microbubbles are small (0.46 MPa for 1-2 μm) and lower if the bubbles are larger (0.3 MPa for 4-5 μm) [174] [175].

Table 6.2: Specification of commercial microbubbles used for BBB opening studies.

Name	**Shell material**	**Gas**	**Mean size (μm)**	**Concentration (bubbles/mL)**	**Recommended dose**	**Life time (minutes)**
Definity®	Phospholipid	C_3F_8	1.1-3.3	1.2×10^{10}	10 μL/kg	2-10
SonoVue®	Phospholipid	S_3F_6	2-8(2.5)	$1.0 - 5.0\times10^{8}$	2.5-10 μL/kg	3-6
Optison™	Albumin	C_3F_8	2.0-4.5	$5.0 - 8.0\times10^{8}$	0.5 mL	2.5-4.5

6.4.6 BBB opening procedure

The experimental setup scheme of the current study is shown in Figure 6.2. The pulse amplitude (80 mVpp) of a function generator was used to generate peak-negative acoustic pressure (0.364 MPa, mean value of center 4mm^2 area, Figure 6.5). This acoustic pressure was sufficiently low to ensure safety and reversibility of the BBB opening. The transducer was used to generate pulsed sonication with a 1 Hz burst rate of 1 ms burst durations for 3 min (general protocol in Figure 6.6). SonoVue powder (SonoVue TM, Bracco International, Milan, Italy) was mixed with sodium chloride for the injection. A bolus of 50 μL of microbubble was injected intravenously (*i.v.*) with an MRI compatible syringe pump (PHD 2000, Harvard Apparatus, MA, USA) via a catheter before sonication. Subsequently, 200 μL microbubbles were continuously administered with the pump during the 3 min of US sonication. Animals were prepared within a stereotaxic frame (Leica Biosystems, Wetzlar, Germnay) for anesthesia and positioning. The US transducer was filled with degassed water and the acoustic pressure center positioned on the bregma point of skull.

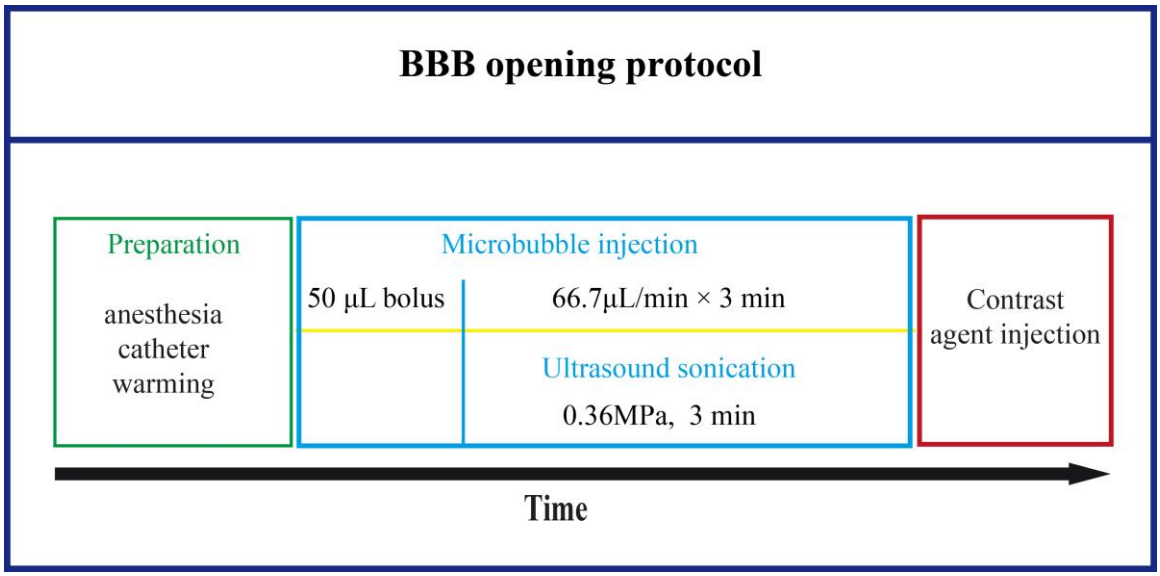

Figure 6.6: The general procedure for for ultrasound-mediated (US-mediated) BBB opening.

6.5 MRI contrast agent delivery

6.5.1 Gadolinium-based MRI contrast agent delivery

We are also interested in brain labeling with MRI contrast agents. Gadolinium (Gd) has been one of the most predominant and revolutionary elements for MRI contrast agent development in medical diagnosis. The paramagnetic lanthanide metal Gd is able to shorten the longitudinal relaxation time T_1 of water protons with its seven unpaired electrons. DOTAREM® is a macrocyle-structured Gd based contrast agent consisting of organic acid DOTA as a chelating agent and Gd^{3+}. It is commonly used to assess the leakiness of the BBB and abnormal vascularity with MRIs.

DOTAREM® (Guerbet GmbH, Sulzbach Germany) was diluted with saline to 0.5 mM after a 6 min baseline scan with MRI compatible syringe pump in 25 min (injection speed of 5.2 µL/min, total volume 110 µL). The mouse was also co-injected with 20 µL (25 mg/mL) near-infrared dye ICG (Pulsion Medical, Feldkichen, Germany) for *ex vivo* assessment of fluorescence distribution in the mouse brain.

All *in vivo* experiments were carried out in strict adherence to regulations from the state government of Bavaria, Germany. C57BL/6 Mice were anesthetized with 1.5-2% isoflurane and underwent the 3 min US sonication BBB protocol. Mouse positioning, transfer to scanner, and scan sequence selection were performed within half an hour. All MRI experiments were carried out with a Bruker Biospin 9.4 T scanner (Bruker, Karlsruhe, Germany). Subsequent MRI image series of T_1 weighted images were acquired with rapid acquisition with relaxation enhancement (RARE) sequences (13 slices, 2 averages,

TR = 625 ms, TE = 8.2 ms, slice thickness = 1 mm, interslice distance = 1 mm, 1 min for each repetition) and repeated 95 min.

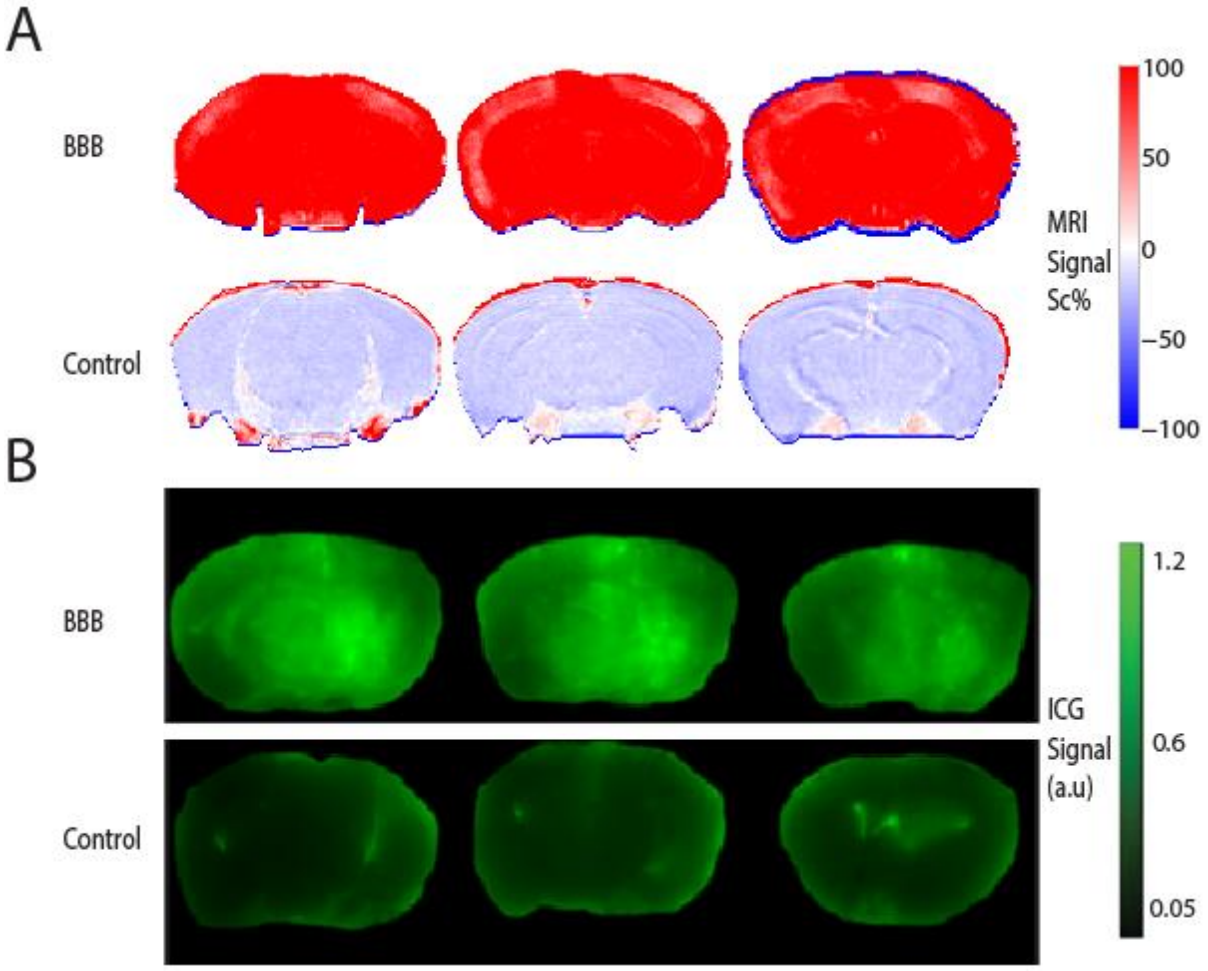

Figure 6.7: Coronal MRI and epifluorescence images showing trans-BBB delivery of DOTAREM® and ICG after US-mediated BBB opening and control group with only microbubble and contrast agent delivery. (A) *In vivo* MRI signal percent increase 1 hr after BBB opening with i.v. injection of MRI contrast agent. (B) Epifluorescence of coronal slices imaged 1.5 hrs after the BBB opening with co-injection of near-infrared dye ICG.

Compared to the control group without US sonication, the MRI signal increased more than 50–100% in almost of the brain 1 hr after the BBB opening (shown in Figure 6.7). Subsequent *ex vivo* histological analysis of the brain via cryosclicing and epifluorescence (Figure 6.7B) was conducted to visualize the distribution of the co-injected near-infrared dye ICG. Moreover, histological analysis was performed to assess any signs of cell death and/or astrogliosis (imaging data not shown). The near-infrared dye ICG was selected for this study due to its well-known characteristics and various applications in OA imaging.

.

The ROI analysis in the cortex, subcortex area, and the third ventricles in 1.5 hrs were used to study the T_1 contrast enhancement dynamics after the BBB opening (Figure 6.8). The first 6 min were the baseline, and then the DOTAREM agent was administered after 25 min and followed by an hour scan.

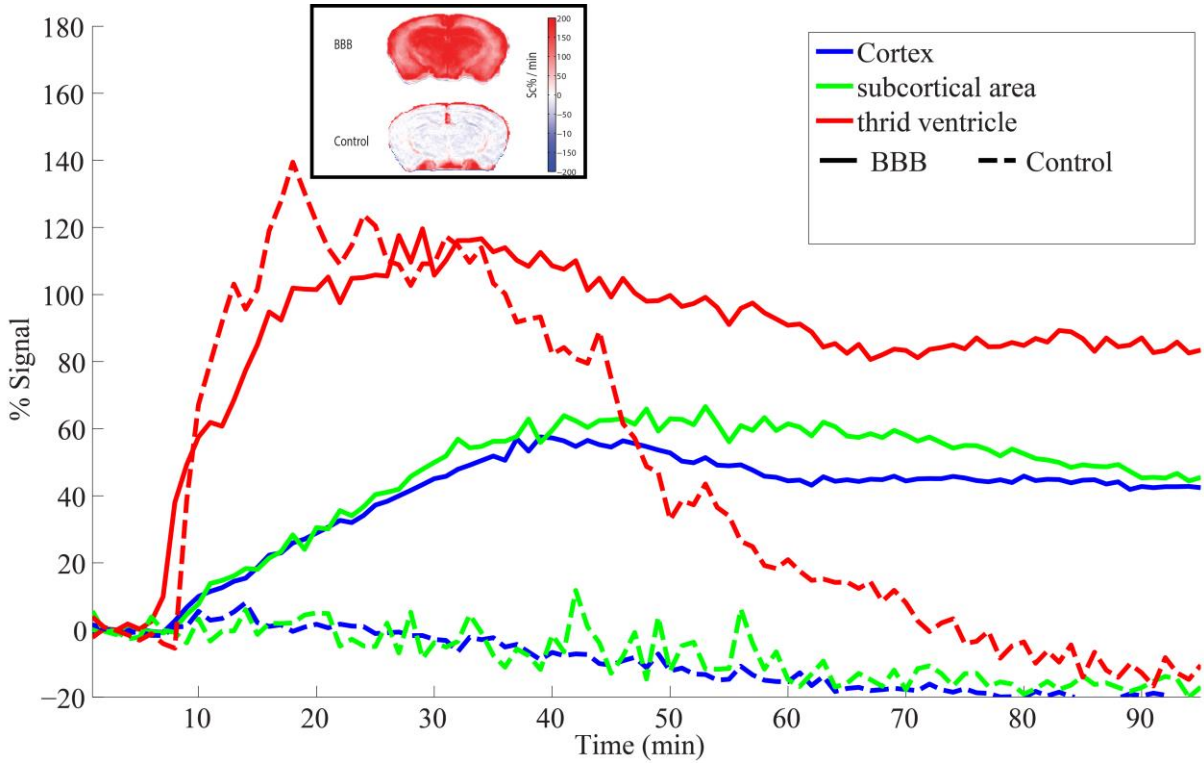

Figure 6.8: Signal changes in different ROIs after BBB opening (solid line) and for the control condition (broken line). The inset shows the spatial distribution of the rate of signal change for representative slices.

6.5.2 Functional MRI contrast agent based on MEMRI method

The previous section demonstrated the unspecific diffusion of Gd-based agents. Hence, the MRI contrast mainly arises from the molecules remaining in the cerebral vasculature of brain after 1.5 hrs of circulation (Figure 6.9). The purpose of this section is to further explore targeting MRI contrast agents' delivery for functional brain research.

Functional magnetic resonance imaging is a MRI technology that detects the hemodynamic changes in signals trigged by elevated neuronal activity. It establishes a correlation between defined stimulation

patterns and the blood oxygen-level dependence (BOLD) effect, the combination of changes of local blood oxygenation, cerebral blood flow (CBV), and cerebral blood volume (CBF) [176] [177]. This indirect and complex dependence on the BOLD effect makes it difficult to quantitatively deconvolve neural signals, and it is still challenging to distinguish more finer neuronal effects such as specific cortical columns [178]. Therefore, there is growing interest in more direct investigation of neural activity using MRI contrast agents that have higher sensitive and specificity to neurons.

One of direct labeling approaches is the use of the second messenger molecular ion, Ca^{2+}, which enters a neuron's pre-synaptic terminal through voltage-gated and ligand-gated Ca^{2+} channels when an action potential is triggered. Calcium sensors have become extremely powerful tools due to dramatically transient Ca^{2+} concentration changes, that is, intracellular concentration increase from ~50–100 nM to 500–1000 nM, while extracellular Ca^{2+} concentrations decrease by up to 30% from a resting state ~1.2 mM [179][180]. The divalent ion Mn^{2+} happens to be a biological analogue calcium for MRI agents because this metal can enter excitable cells via Ca^{2+} channels during nerve action potentials. In T_1-weighted MRI images, this paramagnetic marker causes the specific region to become brighter as a result of ion accumulation in active neurons. The pioneering demonstration using Manganese-enhanced MRI (MEMRI) for brain activity was performed by A. P. Koretsky et al. in 1997 [138].

Even though Mn^{2+} is an essential element for brain development and metabolism, it can be a neurotoxicant when it excessively accumulates. The uptake rate of Mn species through carrier mediated influx and efflux is quite slow [181]. Rapid Mn influx results from choroid plexuses into cerebrospinal fluid (CSF) spaces then into the brain [182]. The MRI can mainly observe the contrast enhancements mainly in larger ventricular spaces and circumventricular organs through blood-CSF barrier within 2 hrs after infusion of Mn^{2+}, but observe no measurable enhancements in the cortical region. The maximum heterogeneous distribution of MRI contrast enhancement, however, can be achieved 24 hrs post-injection. This slow process of sufficient accumulation in the active regions of a mouse brain is only effective for stimuli which are amenable to prolonged administration. Hence, long manganese diffusion by slowly releasing Mn^{2+} allows network pathway mapping which only reflects an integration of long neuronal activity, such as auditory cortex mapping [183]. However, significant care is necessary to exclude non-specific activation Mn^{2+} uptake in long experiments. To obtain acute signal enhancement in rats, the BBB opening is usually achieved with osmotic disruption which requires the infusion of highly concentrated (~25%) hyperosmolar solution mannitol through an intra-carotid injection to avoid blood flow disruption. This procedure is feasible for rats with transient BBB disruptions, but it is difficult in surgically cannulated adult mice through a catheter placed retrograde to the external carotid artery. This rapid BBB opening technique is too invasive for mice models and could lead to serious hypotension and seizures. Moreover, the osmatic technique achieves BBB openings only in a portion of one hemisphere with relatively inhomogeneous distribution.

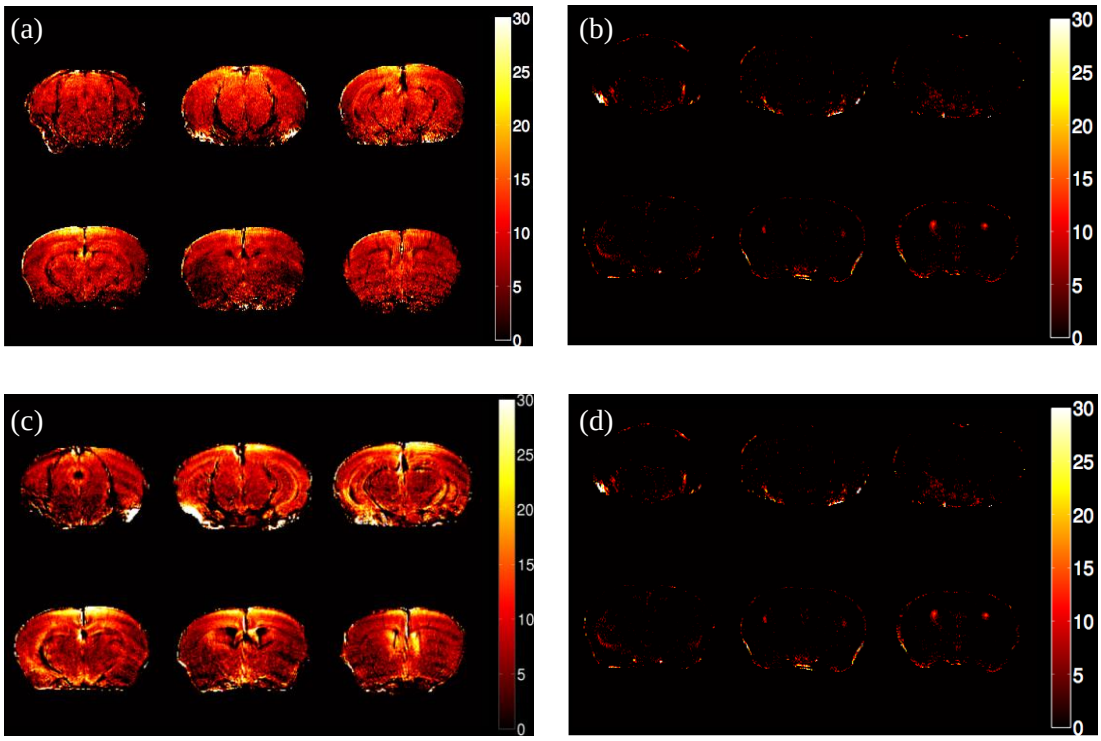

Figure 6.9: Magnetic resonance imaging signal increase after Mn^{2+} injection in (a) 30 minutes and (c) 80 minutes of the BBB opening and the corresponding control group (b) and(d).

Recently, a combination of US and gas microbubbles technique has been shown to open the BBB transcranially and noninvasively in mice. However, most of these studies only used focused US transducers for the focal region of the BBB opening due to the fact that the active diameter of a focus transducer is around ~1-2 mm and focal energy deposition. Thus, a focused transducer is not ideal for large volume BBB opening studies. The ideal unfocused US-mediated BBB opening has been introduced for Mn^{2+} delivery [184], however, it is still not clear study how to achieve large volume of BBB opening with minimal damage to neurons. Additionally, a temporal kinetic study of Mn^{2+} uptake is necessary to obtain homogeneous and stable distributions after the BBB is opened.

In this work, manganese chloride ($MnCl_2$-$(H_2O_2)_4$, Sigma) was dissolved in a bicine solution (100 mM) and adjusted pH to 7.4 using NaOH to a 100 mM concentration. $MnCl_2$ was intraperitoneally (*i.p.*) administered with a 0.4 mmol/kg dose and 10 minutes prior the sonication according to the BBB opening protocol. Mice were transferred to the MRI scanner and the right sequence selection was performed within half an hour. Subsequently, the MR image series of T_1 weighted RARE images was acquired (13 slices, 2 averages, TR = 625 ms, TE = 8.2 ms, slice thickness = 1 mm, interslice distance = 1 mm, 1 minute for each repetition) and repeated for 90 min. A transceiver cryogenic quadrature RF surface probe (Bruker MRI CryoProbe, Karlsruhe, Germany) was used to acquire the Mn^{2+} contrast

kinetics over the entire mouse brain. The MRI signal increases by up to 20%, even after 80 min of the BBB opening in the mice and there was no signal in the brain region except the ventricular system. The relatively homogenous enhancement of the brain was observed at a later point in time. Compared to a Gd-based agent, Mn^{2+} exhibited a much slower diffusion into the brain as the signal incensement from the ventricle system was stronger after 80 min. This indicates more stabilized Mn^{2+} distribution could be achieved after 80 min (*i.p.*) injection. To distinguish the subtle enhancement due to specific stimulation applied in MEMRI studies, this temporal comparison implies that maybe a longer Mn^{2+} diffusion time is needed once the BBB is opened (Figure 6.8). Therefore, longer systemic administration of Mn^{2+} would bring benefits for cortical mapping studies as the MRI contrast enhancement comes primarily from the brain tissue itself rather than remains in cerebral vasculature after a long period of circulation.

6.5.3 US-mediated BBB opening for antibody-based therapeutic agents' delivery

Unlike previous work, the aim of this section is to investigate whether larger-size molecules can be delivered. Antibodies are interesting as antibody-based agents are promising chemotherapeutic agents for neurodegenerative diseases of the central nervous system. In this section, the potential for unfocused US-mediated BBB opening for fast and therapeutic application in brain disease treatment is explored.

We injected the same amount of Cy3-conjugated α-chicken antibody (20 µL) to US sonication or control treatment mouse. Half an hour after administration, mice were euthanized and frozen intact for epifluorescence images. Cy3-conjugated α-chicken antibody has an excitation and emission peak of 550 nm and 570 nm, respectively. The *ex vivo* fluorescent spatial distribution images were acquired through multispectral epi-illumination cryoslicing imaging systems retrofitted with a custom-made cryotome [99]. This setup allows the user to acquire RGB and fluorescence images with adjustable filters. The excitation filter of the R component (D535/40 m, Chroma Technology GmbH, Olching, Germany) and emission filter at 590 nm (band width of 40 nm) were employed to capture the fluorescent signal.

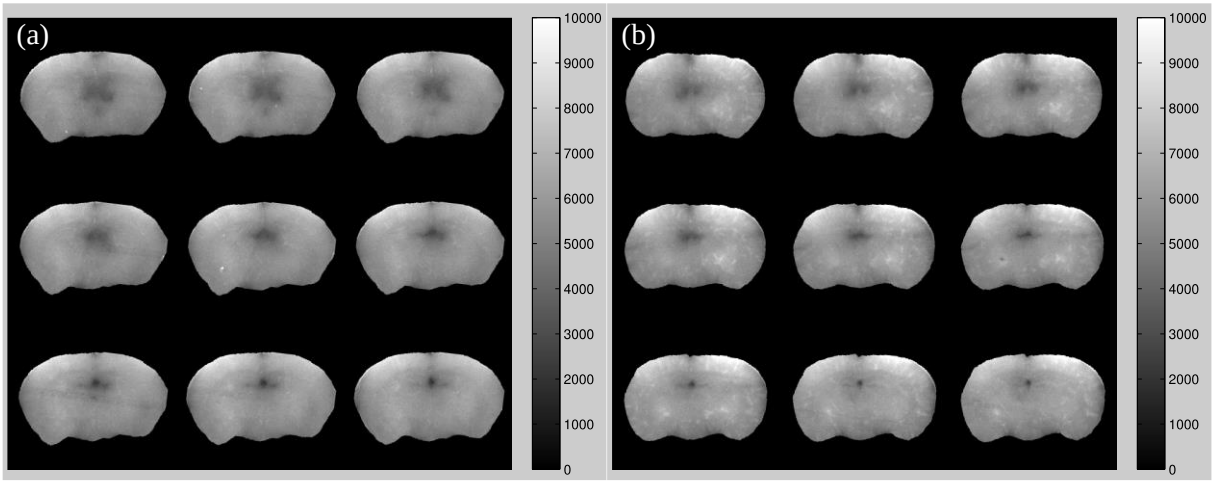

Figure 6.10: Montage display of spatial fluorescent signal distribution after the same amount of antibody was injected for (a) control and (b) US-mediated BBB opening treatment mouse brain.

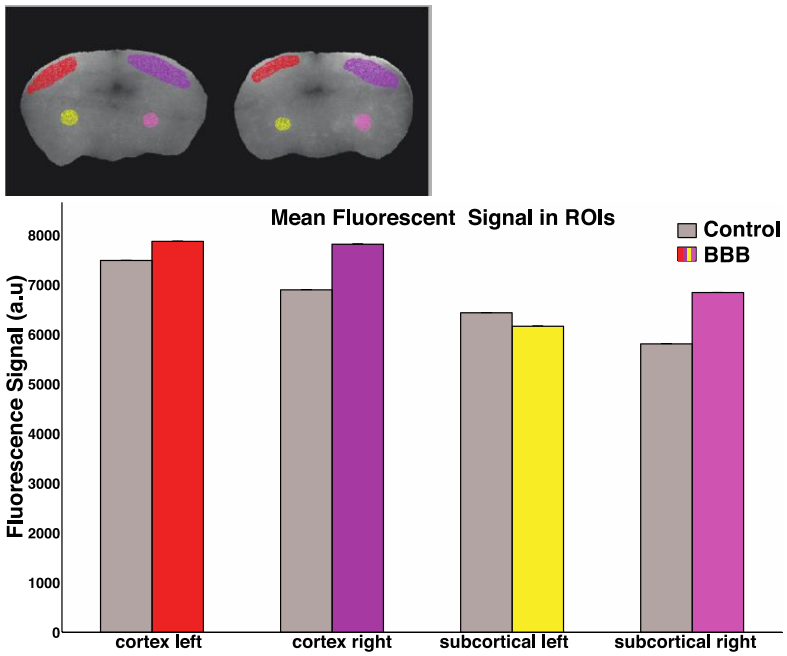

Figure 6.11: Quantification ROI fluorescent signal on the representative coronal brain slice. The color bars are corresponding to with ROI selections as the inset showed.

Figure 6.10 shows the montage display of spatial fluorescent signal distribution half an hour after an intravenous injection of the same amount of antibody into a control and US sonication treated mouse brain. Brighter fluorescent distributions were found in coronal images of the BBB opening group, although scattered and punctuated patterns throughout the tissue sections were also observe. The ROI quantification fluorescent signal of cortex and sub-cortex regions (indicated by color overlapping)

from the typical slices are shown in Figure 6.11. In most of the brain regions, the fluorescent signals of the BBB opening group are stronger than in the control group, indicating the accumulation of Cy3-conjugated α-chicken antibody. This study shows the feasibility of delivering nanometer size antibodies but with a heterogeneous overall distribution. This is likelyy due to fact that large compounds are more likely be deposited at proximal ends of larger, vessel branches in the brain.

6.6 Conclusion and Discussion

To date, a majority of studies using microbubbles administration focus on US sonication to achieve the BBB opening in a local and precise anatomic region. The unfocused US approach opens the BBB in a large area of whole brain for the good penetration and homogenously distribution of small molecules to most of the brain. When the agent molecules are in the nanometer range, the corresponding pressure needs to be increased. Protocol variations of US parameters (amplitude, pulse repetition frequency, pulse length, and treatment time) and microbubble properties (fresh microbubbles amount, bubble size, and lifetime) could lead to delivery differences in terms of molecule size, volume, and tissue damage. It is difficult to extrapolate the existing parameters of focused US approach and unfocused US methods due to the inhomogeneous distribution of both skull attenuation and transducer beams in a whole brain volume. Protocol refinement and further evaluation of these effects can reduce the neuron damage and increase the BBB opening efficacy in the brain. Based on the different size molecules delivery results we acquired, the different aspects are disused in the following.

6.6.1 Molecular delivery through ultrasound-mediated BBB opening

A variety of contrast agents and therapeutic compounds using focused US approach have been demonstrated in several setting for MRI contrast agents. Examples include Mn^{2+} (54 Da), Gd-DTPA (573-928 Da), Magnevist® (938 Da) [155], gold-nanorods (size of 40 nm by 10 nm) [185], and superparamagnetic iron nanoparticles (SPIO, 60 nm) [186] have been shown. Targeting agents such as doxorubicin (544 Da) [175], Trypan Blue (872 Da) [187], Evans blue (960 Da), horseradish peroxidase (49 kDa) [164], Texas-Red-tagged dextran (3-70 kDa) [191], Herceptin (148 kDa) [189], therapeutic anti-amyloid β antibodies (150 kDa) [187], and liposomes (80 nm) [190] have been reported as well.

In this study we showed that several types of molecules could be delivered through unfocused ultrasound-mediated BBB opening in a large portion of the brain. This established protocol shows a promising application for agent delivery in a large volume of brain for noninvasive neuroimaging and CNS diseases treatment research.

Molecules used in our study indicate that this BBB opening approach can be used for agent delivery from 54 Da (Mn^{2+}) to 2000 kDa (~20 nm, Cy3-conjugated α-chicken antibody). The result indicate promise for large-size molecular compounds compared to focused BBB opening approaches, reported to deliver to tens of kDa compounds with transient BBB opening [191]. The molecular weight threshold was identified to lie between 70 and 2000 kDa, as no significant fluorescent signal of the target hippocampus could be observed with 2000 kDa dextran (mostly outside the hippocampus) and it provided a diffuse signal for smaller molecular (3 kDa and 70 kDa) [188][191]. The MRI contrast can be increased by at least 50% and 20% in the cortex and sub-cortex region with the administration of Gd-based and M^{2+} agents, respectively. This study shows the potential for delivering molecules of various sizes, such as enzymes (100 - 1,000 Da) and proteins (30 - 3,000 kDa), in a large volume of the brain.

6.6.2 Unfocused transducer and focused transducer

Although both focused and unfocused US in combination with gas microbubbles have been used for noninvasive and transcranial BBB openings in mice, the technique has been primarily investigated for the hippocampus and is associated with neurodegenerative diseases studies. A Single-element focus transducer is sufficient to induce a well-formed focal spot for BBB openings in mice and non-human primates *in vivo*. However, the unfocused US approaches demonstrated here show several advantages for functional brain imaging and drug delivery for brain diseases.

(a) With an unfocused transducer, small molecules that label neuronal activity can be immediately administered for functional brain imaging with acute stimulation. The focused transducer could only generate small regional agent uptake in the brain. For example, with 0.45 MPa sonication and 1-2 µm bubbles, a focused transducer was able to cover a BBB opening volume on the order of a few cubic millimeters (2.3 ± 1 mm^3) [165]. For the acute stimulation paradigm study, the contrast agents had to reach large portion of the brain noninvasively, efficiently, and homogeneously. The other options are either too expensive, such as the modification of contrast agents, or too invasive to perform, such as intra-arterial injection of hyperosmotic mannitol solution in mice. Moreover, opening the entire brain's BBB could permit longitudinal simulation studies because the BBB can be repeatedly and efficiently opened.

(b) On the other hand, drug delivery for neurodegenerative disorders is also restricted by focal volume. In Alzheimer's disease, for example, the mature plaques could disperse in the cortex, hippocampus, and thalamus rather than a specific focal region due to aggregation of more diffused amyloid-β peptides [187]. This could potentially be optimized by repeated scanning focused ultrasound treatment reported Jürgen Götz group and others [194]. A focused US has been shown to cover the whole brain by scanning the transducer with 3D motorized scanning system. This

approach allows for the removal of amyloid-β plaques deposits and memory improvement in mice brains with 6 seconds sonication for each position (0.7 MPa peak rarefactional pressure, 10Hz pulse repetition frequency, 10% duty cycle). However, the earliest extravasation evidence was only achieved 30 min after treatment. This can be compared to the unfocused system we demonstrated here which only takes 3 min to open the BBB of whole brain. Therefore, this unfocused US BBB opening approach is more suitable for pre-clinical drug screenings and targeting probe development with the cost of beam accuracy required by clinical treatment [192].

In utilizing an unfocused transducer for the BBB opening, the following aspects should also be considered:

(a) To quantitatively establish the acoustic pressure amplitude for the BBB opening, an acoustic pressure mapping of the transducer has to be measured with a calibrated hydrophone. To achieve the minimum neuron damage and maximum coverage with the threshold pressure, the peak-to-peak voltage input current provided by the function generator and the resulting acoustic pressure has to be determined for large diameter unfocused transducers. This procedure is more convenient and feasible for focused transducers because researchers can easily get the value form the product specification.

(b) The positioning of an unfocused transducer is more challenging for reproducible BBB openings. The center of the transducer has to be accurately matched with the anatomic landmark for targeting, such as the bregma point of skull. Thus, more precise acoustic pressure mapping and stereotactic systems are necessary for positioning.

(c) Generally speaking, opening the BBB of the entire brain is not always necessary for functional brain research. The unilateral response to stimuli is already quite known. A contrast agent can be administered to only one hemisphere and the control response can be readily obtained from the untreated hemisphere. In theory, this unfocused transducer BBB opening approach could be optimized by adding a half circle material that causes a strong acoustic attenuation to the exit plane of the transducer so that only one hemisphere will be treated with US. Moreover, it is also feasible to achieve a more specific portion, such as only the forebrain brain region, with an acoustic attenuator with more quantitative and specially designed geometry.

(d) To obtain quantitative and reproducible unfocused US beams, inconsistent and complex skull attenuation at different locations of brain has to be considered. Furthermore, the vascular characteristics, i.e., vascular density and vessel size, which could vary in different brain regions,

may influence the efficiency of the resulting agent distribution and BBB opening. To reduce uncertainties or instabilities in whole brain, acoustic coupling should consider this aspect.

6.6.3 BBB opening optimization and direction for the contrast agent delivery

To date, a combination of US and microbubbles have shown the most promising results for opening the BBB. Though the exact mechanism of US induced BBB opening is still not fully understood, preliminary studies indicate the feasibility of acoustic parameters that could enable a safe BBB opening with the absence of cell or tissue damage. The majority of molecules that cross the BBB have been shown to be on the order of 0.5–70 kDa. To extend the use of US-mediated BBB opening techniques to various sizes of molecules in neuroscience, a comprehensive knowledge of each specific molecule and its spatial/temporal distribution after the BBB opening is required. There is still ongoing research as to the optimal settings to achieve sufficient delivery correlated with molecular size. To obtain a satisfactory outcome, technique optimizations can be categorized into two basic strategies. The first focuses on the modification of molecules and the second exploits US BBB parameters. Here, we primarily discuss the US BBB approach itself.

6.6.3.1 Acoustic parameters optimization

Several investigations on US parameter modulations have been studied to achieve noninvasive, transient and safe BBB opening. These acoustic parameters include center frequency, acoustic pressure, pulse repetition frequency, pulse length, and treatment duration.

The center frequency selection is one of the key parameters, which normally a tradeoff of microbubble size, vessel diameters and skull attenuation of animal model used. The optimal frequency of ultrasound should produce a suitable transcranial sonication with microbubbles and incorporate the beam distortion correction due to the skull bone. What's more, it should avoid the overheating due to the absorption of skull. The numerical resonance frequency of microbubble size has already been shown (Table 6.1). The optimal frequency selection further investigations to acquire comprehensives knowledge on the microbubble oscillation/collapse, blood vessel size distribution and viscoelasticity of brain vasculature [167].

A useful metric to estimate the BBB opening threshold is the mechanical index (MI), defined as the peak negative pressure amplitude *in situ* divided by the square root of the center frequency. If the hypothesis that the BBB opening threshold is linearly correlated with the MI holds true [196], lower frequencies with lower pressure will be optimal, as less vasculature damage and less skull attenuation will be induced. For small animals, the center frequency selection has a wider selection range compared to bigger animals such as primates. A center frequency of 0.4 [194], 0.69 [187], 1 [192], 1.5

[148] and 2 MHz [195] were reported to achieve successful BBB opening in mice. For larger animals, a lower frequency (0.2~1 MHz) is typically selected due to less phase aberration and the absorption of the skull bone and enhanced cavitation effects for safety concerns [196].

For a given transducer and specific commercial microbubble size, separate acoustic pressure thresholds exists. For mice with 1.5 MHz transducer sonication, the threshold is in the range of 0.3–0.45 MPa (calibrated on account of 18.1% murine skull attenuation) for 1–2 μm microbubbles, while for microbubbles with a larger diameter (4–5 μm and 6–8 μm), a lower pressure amplitude (0.2–0.3 MPa) was determined to be safe [161] [197] .

In addition to acoustic frequency and pressure, rather than the various pulse repetition frequency or microbubble concentration, the pulse length significantly influence the threshold of the BBB opening [198][199]. A significant increase of contrast agent delivery was found from 0.1 to 10 milliseconds range but no efficacy increase above 10 ms, even though a 2.3 μs pulse length was found to be sufficient A significant increase of contrast agent delivery was found in the 0.1–10 ms range, but there was no increase in efficacy above 10 ms. A 2.3 μs pulse length was found to be sufficient.

Moreover, the total sonication duration for treatment plays an important role. Depending on the microbubble size and acoustic amplitude used, for a focused transducer, a treatment time of around 30 seconds to 1 minute was determined to be sufficient. For whole brain BBB opening, unfocused US excitation is applied for a longer time (~3 min) to achieve efficient microbubble interactions in a large volume of the brain [200].

6.6.3.2 BBB permeability and contrast agent size

The determination of the optimal acoustic parameters for the delivery of various sized agents is an important, ongoing area of research. The optimal parameters for more homogenous distributions of large size molecules therefore need to be careful explored. As shown in the current study, various molecule sizes may induce distinct patterns in the delivery region after the BBB opening, because smaller agents may be delivered at more effective concentrations in smaller vessels, while larger molecules are more likely remained in the region near or along larger vessels and thus deposited in several punctate regions.

Though studies report the molecular weight threshold is less than 2000 kDa, recent developments suggest that 80 nm sized liposomes are feasible with 4 min sonication but with a lower frequency transducer (center frequency 612.5 kHz) [190]. Thus, large sized pharmacological drugs and contrast agents to cross the BBB are expected with more advanced developments in US-mediated BBB opening techniques.

6.6.3.3 Microbubble development for BBB opening

The physical mechanisms of microbubble interactions in brain vasculature and the subsequent cell impacts of this US mediated BBB opening approach remain to be determined. Microbubble size is on critical parameter, as the BBB opening threshold and volume are bubble size-dependent [161]. For mice models, lower acoustic pressure thresholds are required for 4–5 μm bubbles, compared to 1–2 μm bubbles, as 4–5 μm bubbles are more likely to undergo inertial cavitation or fragmentation in comparably sized capillaries.

Although it has been indicated that the overall dose of microbubbles may have no effect on the BBB opening, they may have an effect on the spatial distribution of the delivered contrast agent as a result of BBB opening sites along small capillaries.

To date, the majority of US agents that have been employed for BBB opening are commercial polydispersed microbubbles (Table 6.2). The SonoVue microbubble used in the current study have a mean diameter of 2.5 μm and more than 90% of the bubbles are smaller than 8 μm. However, a portion of the bubbles are still around 15 μm, exceeding the small capillary diameter of 4-8 μm [169]. As a polydispersed microbubble, SonoVue has been shown to microbubbles concentrated at or near large vessels after the BBB is opened [174]. Therefore, more monodispersed microbubbles close to the capillary diameter would be a safer choice for the sufficient induction of nonlinear bubble oscillations, rather than inertial cavitation when an acoustic filed is applied.

Additionally, in-house manufactured and size-isolated microbubbles could also benefit BBB opening applications. The concept of encapsulating microbubbles with a contrast agent on the polymer shell is a promising direction which could increase the concentration of contrast agent delivered in the transient disruption of the BBB. Thus, the guidance and monitoring of a US-mediated BBB becomes feasible with the help of *in vivo* imaging instruments. For example, Gd-based compounds and superparamagnetic iron oxides (SPIO) combined with microbubbles were used for BBB openings and concurrent MRI and US imaging, respectively [201][202].

6.6.3.4 Efficiency of BBB opening protocol

The current study's general protocol for whole brain BBB has been explained (Figure 6.6), however, the protocols efficiency could be further optimized according to specific molecules and application requirements. Compared with agent injection after US sonication, contrast agent administration before the sonication procedure is thought to increase delivery efficiency [156]. Our study demonstrated that both contrast agent injection prior to (Mn^{2+}) and after BBB opening (DOTAREM) are feasible. In both cases, clear MRI signal enhancements were observed for high concentrations of small molecules.

However, the specific effects of contrast agents and microbubbles during US sonication have to be clarified and further pharmacokinetic analysis implemented.

Similarly, most studies assume that it is optimal for microbubbles to be intravenously injected 1 min prior to sonication. Here, we conducted microbubbles injection with a bolus (50 μL) prior to sonication, though continuous injection with a pump while sonication is conducted may be a more efficient method to enhance the availability of microbubbles within brain vessels.

For behavioral tasks related to functional brain imaging, contrast enhancement of image neuronal responses relies on the temporal homogeneity of the agent delivered, that is, the distribution of the contrast agent not changing significantly over time when the stimuli is applied. Both intravenous infusions and intraperitoneal injections have been demonstrated to effectively manage the systematic administration of a contrast agent. However, the BBB opening procedure has to minimize acute toxicity and temporal variation when the contrast agent is toxic, i.e. Mn^{2+}. Intraperitoneal administration in such cases allows for a slower uptake to the bloodstream and thus may produce a more temporally consistent distribution after the BBB is opened.

6.6.3.5 Safety of BBB opening

With US mediated BBB opening approach, both short-term (30 min and 5 hours) [203] and long-term (1-4 weeks) [204] studies report that a safe window exists. An optimal combination with peak-rarefactional pressure is feasible for keeping the endothelial and neurons free of hemorrhages associated with BBB opening. However, a complete safety analysis beyond a gross histologic examination remains to be addressed. The translational potential of this approach should be further explored to minimize any related bioeffects and side effects.

As described, the BBB is comprised of endothelial cells that regulate the central nervous system. Following transient mechanical disruption, BBB tight junction proteins become loose and allow serum proteins to accumulate in the brain parenchyma with increased permeability. Though it has been shown that albumin may assist in amyloid-β peptide engulfment of the brain and facilitate microglia activation, albumin is a neurotoxin and causes neuronal cell death. Other endogenous immunoglobulin (such as IgM, IgG) antibodies, or the activation of glia cells, may benefit neurological disorders [205][206][207]. However, they are unnecessary for most exogenous contrast agent or drug delivery applications. Their potential effects on neurons must be further investigated. In the microenvironment, the intensity of reactive astrogliosis, vasculature morphology/function changes, and neuroinflammation are correlated with BBB disruption. This knowledge is important for researchers in understanding neuron activation during and after the BBB opening, for example, effects on the BOLD signal after opening the BBB.

Chapter 7 Conclusion and outlook

7.1 Summary

Through employing multi-wavelength illumination, multi-element US array detection, multi-channel acquisition, model-based reconstruction, and unmixing processing, MSOT holds a remarkable capacity for the quantitative mapping of optical absorbers with high spatial and temporal resolution in deep tissues.

Despite the versatile sources of FPs, non-fluorescent chromophores available for OA imaging, existing and common genetic labeling agents are not ideal, as they require a high molar extinction coefficient, NIR, and high photostability. In the current study, we proposed three strategies using a spatial domain, a time domain, and molecule delivery to increase the potential applications of MSOT.

The characteristics of the biosynthesis pigment Vio, such as a spectrum close to the NIR, high photobleaching resistance, enzymatic amplification, and a fast and robust optoacoustic signal efficiency, were demonstrated. We demonstrated these advantageous features in the context of bacterial tumor tracking in which we were able to detect Vio-expressing bacteria *in vivo* in tumor tissue.

The current study introduced a new dimension, the time domain, for the specific detection of contrast agents via OA imaging. Specifically, the concept of a controlled OA signal over time as an independent feature adds to the differentiating capacity of MSOT. This temporally unmixed MSOT approach is thus an addition to well-known spectra unmixing. We demonstrated this approach with RSFPs whose signal trajectories can be photocontrolled, such that the particular temporal patterns then can be unmixed from static signals, even if they are strong absorbers. For the first time, to our knowledge, temporally unmixing proteins with low concentration resulted in a high contrast to noise ratio and achieved detection sensitivity.

The introduction of these two types of contrast agents provides new possibilities for high-resolution, high CNR, and quantitative detection. Hence, *in vivo* applications for bacterial tumor tracking, neural network monitoring, and cardiovascular dynamics are expected with MSOT.

Besides the development of a molecular agent, the US mediated BBB opening technique was established to overcome hurdles of molecular agent delivery and targeting in the brain. The systematic characterization of this unfocused US-based approach and the successful examples of contrast agent

delivery in mice brain proved successful. This methodology can be used for various sizes of molecules for fast delivery in a large volume of the brain and with minimal neuronal damage. In the current study, the potential of large volume contrast agent targeting in functional neuroimaging and drug delivery for CNS diseases treatment were demonstrated. The proposed methodology optimization is next discussed.

7.2 Outlook

In general, molecular imaging with OA imaging holds great potential for noninvasive, real-time, volumetric imaging in small animal models. However, further work is required.

In terms of instruments, an upgraded imaging system and processing methodology are necessary for various imaging scenarios. For example, candidate molecular agents for screening and OA spectrum detection would be significantly benefited by a laser that can offer both visible and NIR range. An MSOT system that provides fluorescent signal detection would also enrich understanding and validation of fluorescent agents' optoacoustic efficiency, related to molecular absorbance, quantum yield, and light fluence. The detection sensitivity and absolute concentration quantification of OA systems have not been directly characterized by this research. The inhomogeneous light fluence and tissue scatterings characterizations for *in vivo* imaging scenarios remain a challenge for further research.

The anti-cancer activity of bio-expressing bacteria *in vivo* is of particular interest in addition to Vio to genetic sensor circuits. Furthermore, extensive efforts have made to gain transcriptional control of the Vio biosynthetic pathway using CRISPR RNA scaffolds, a proof-of-principle for metabolic engineering in eukaryotic cells [208]. It would be interesting if the biosynthetic pigments could be produced in eukaryotic cells by expressing the enzymatic machinery for pigment generation

To expand the multiplexing ability of tuMOST, further *in vivo* implementation of reversibly switchable FPs in zebrafish and mouse models is necessary. Compared to recent reports with an NIR photochromic probe [209], our proposed approach is expected to exhibit faster switching kinetics, photocontrollable potentials, and a high CNR with the presence of a strong absorber. Moreover, optimizing the large class of synthetic and genetically encoded photochromic molecules, especially in the NIR, would lead to high contrast and high sensitivity OA imaging.

Furthermore, with the established US-mediated BBB opening technique, further work is being devoted to deliver a variety of molecular agents to the brain for OA imaging systems. For example, a reversible and selective calcium sensor dye at the NIR being developed by the current study's research team could be further implemented with BBB openings for functional OA imaging *in vivo*. The unique

combination is promising for the acceleration of pharmaceutical research, functional brain imaging, and pre-clinical applications.

Acknowledgements

My deepest thanks go to my adviser Prof. Gil Gregor Westmeyer who offered me this opportunity of interesting and promising field. All the work presented benefits substantially from his outstanding scientific guidance, profound insights, and valuable supports.

I am grateful to my adviser Prof. Wolfgang Wurst, my mentor Prof. Daniel Razansky and Prof. Vasilis Ntziachristos with enormous expertise and knowledge for guiding my research work.

This work would not have been done without the support of IBMI colleagues. Especially thanks to Felix Sigmund and Dr. Andre C. Stiel for molecule agents' development, Dr. Xosé Luís Déan Ben for image instrument and measurements, Dr. Anurag Mishra for scientific and personal opinions. Additionally, I would like to thank Hannes Rolbieski, Dr. Josefine Reber, Sarah Glasl, Dr. Moritz Kneipp, Dr. Héctor Estrada, Panagiotis Symvoulidis, Amy Lin, Salichs Juan for their help and collaboration on the projects. To the rest of my group and IBMI coworkers I would like say thanks for their help in completing my PhD work.

Finally, thanks to my beloved parents and family members for their unlimited support.

Bibliography

[1] M. Rudin and R. Weissleder, “Molecular imaging in drug discovery and development.,” *Nat. Rev. Drug Discov.*, vol. 2, no. 2, pp. 123–131, 2003.

[2] M. L. James and S. S. Gambhir, “A molecular imaging primer: modalities, imaging agents, and applications.,” *Physiol. Rev.*, vol. 92, no. 2, pp. 897–965, 2012.

[3] D. A Mankoff, “A definition of molecular imaging.,” *J. Nucl. Med.*, vol. 48, no. 6, pp. 18N-21N, 2007.

[4] C. W. Sensen, and B. Hallgrimsson, *Advanced Imaging in Biology and Medicine*. Springer Science & Business Media, 2008.

[5] H. R. Herschman, “Molecular imaging: looking at problems, seeing solutions.,” *Science*, vol. 302, no. 5645, pp. 605–608, 2003.

[6] K. H. Ashe, “Learning and Memory in Transgenic Mice Modeling Alzheimer’s Disease.,” *Learn. Mem.*, vol. 8, no. 6, pp. 301–308, 2001.

[7] V. Ntziachristos, “Going deeper than microscopy: the optical imaging frontier in biology.,” *Nat. Methods*, vol. 7, no. 8, pp. 603–14, 2010.

[8] L. V Wang and S. Hu, “Photoacoustic Tomography : In Vivo Imaging from Organelles to Organs.,” vol. 33, no. 6075, pp. 1458–1462, 2012.

[9] S. Mukundan, K. B. Ghaghada, C. T. Badea, C. Y. Kao, L. W. Hedlund, J. M. Provenzale, G. A. Johnson, E. Chen, R. V. Bellamkonda, and A. Annapragada, “A liposomal nanoscale contrast agent for preclinical CT in mice.,” *Am. J. Roentgenol.*, vol. 186, no. 2, pp. 300–307, 2006.

[10] Antoch, G., Freudenberg, L. S., Beyer, T., Bockisch, A., & Debatin, J. F., “To Enhance or Not to Enhance ? 18 F-FDG and CT Contrast Agents in dual-modality 18F-FDG PET/CT.,” vol. 45, no. 1, pp. 56S–66S, 2004.

[11] N. Mitchell, T. L. Kalber, M. S. Cooper, K. Sunassee, S. L. Chalker, K. P. Shaw, K. L. Ordidge, A. Badar, S. M. Janes, P. J. Blower, M. F. Lythgoe, H. C. Hailes, and A. B. Tabor, “Incorporation of paramagnetic, fluorescent and PET/SPECT contrast agents into liposomes for multimodal imaging.,” *Biomaterials*, vol. 34, no. 4, pp. 1179–1192, 2013.

[12] R. A. Kruger, “Photoacoustic ultrasound.,” *Med. Phys.*, vol. 21, no. 1, pp. 127–131, 1994.

[13] X. Wang, Y. Pang, G. Ku, X. Xie, G. Stoica, and L. V Wang, “Noninvasive laser-induced photoacoustic tomography for structural and functional in vivo imaging of the brain.,” *Nat. Biotechnol.*, vol. 21, no. 7, pp. 803–806, 2003.

[14] F. F. M. De Hoelen, C G A and Mul, “A new theoretical approach to photoacoustic signal generation.,” vol. 106, no. 2, pp. 695–706, 1999.

[15] E. I. Galanzha, E. V Shashkov, P. M. Spring, J. Y. Suen, and V. P. Zharov, “In vivo, noninvasive, label-free detection and eradication of circulating metastatic melanoma cells using two-color photoacoustic flow cytometry with a diode laser.,” *Cancer Res.*, vol. 69, no. 20, pp. 7926–34, 2009.

[16] E. Zhang, J. Laufer, and P. Beard, “Backward-mode multiwavelength photoacoustic scanner using a planar Fabry-Perot polymer film ultrasound sensor for high-resolution three-dimensional imaging of biological tissues.,” *Appl. Opt.*, vol. 47, no. 4, pp. 561–77, 2008.

[17] A. Rosenthal, D. Razansky, and V. Ntziachristos, “High-sensitivity compact ultrasonic detector based on a pi-phase-shifted fiber Bragg grating.,” *Opt. Lett.*, vol. 36, no. 10, pp. 1833–1835, 2011.

[18] J. Laufer, D. Delpy, C. Elwell, and P. Beard, “Quantitative spatially resolved measurement of tissue chromophore concentrations using photoacoustic spectroscopy: application to the measurement of blood oxygenation and haemoglobin concentration.,” *Phys. Med. Biol.*, vol. 52, no. 1, pp. 141–68, 2007.

[19] D. Razansky, M. Distel, C. Vinegoni, R. Ma, N. Perrimon, R. W. Köster, and V. Ntziachristos, “Multispectral opto-acoustic tomography of deep-seated fluorescent proteins in vivo.,” *Nat. Photonics*, vol. 3, no. 7, pp. 412–417, 2009.

[20] Laser Institue of America, “American National Standard for Safe Use of Lasers ANSI Z136.1—2014.,” *Laser Inst. Am. Orlando*, 2014.

[21] A. Buehler, E. Herzog, D. Razansky, and V. Ntziachristos, “Video rate optoacoustic tomography of mouse kidney perfusion.,” *Opt. Lett.*, vol. 35, no. 14, pp. 2475–7, 2010.

[22] D. Razansky, A. Buehler, and V. Ntziachristos, “Volumetric real-time multispectral optoacoustic tomography of biomarkers.,” *Nat. Protoc.*, vol. 6, no. 8, pp. 1121–9, 2011.

[23] A. Rosenthal, D. Razansky, and V. Ntziachristos, “Multispectral optoacoustic tomography (MSOT) scanner for whole-body small animal imaging.,” *IEEE Trans. Med. Imaging*, vol. 28, no. 12, pp. 1997–2006, 2009.

[24] A. Dima, N. C. Burton, and V. Ntziachristos, “Multispectral optoacoustic tomography at 64, 128, and 256 channels.,” *J. Biomed. Opt.*, vol. 19, no. 3, pp. 36021, 2014.

[25] S. Morscher, W. H. P. Driessen, J. Claussen, and N. C. Burton, “Semi-quantitative multispectral optoacoustic tomography (MSOT) for volumetric PK imaging of gastric emptyingSemi-quantitative multispectral optoacoustic tomography (MSOT) for volumetric PK imaging of gastric emptying.,” *Photoacoustics*, vol. 2, no. 3, pp. 103–110, 2014.

[26] S. Tzoumas, A. Zaremba, U. Klemm, A. Nunes, K. Schaefer, and V. Ntziachristos, “Immune cell imaging using multi-spectral optoacoustic tomography.,” *Opt. Lett.*, vol. 39, no. 12, pp. 3523, 2014.

[27] C. Kim, T. N. Erpelding, L. Jankovic, M. D. Pashley, and L. V. Wang, “Deeply penetrating in vivo photoacoustic imaging using a clinical ultrasound array system.,” *Biomed. Opt. Express*, vol. 1, no. 1, pp. 278, 2010.

[28] P. D. Kumavor, C. Xu, A. Aguirre, J. Gamelin, Y. Ardeshirpour, B. Tavakoli, S. Zanganeh, U. Alqasemi, Y. Yang, and Q. Zhu, “Target detection and quantification using a hybrid hand-held diffuse optical tomography and photoacoustic tomography system.,” *J. Biomed. Opt.*, vol. 16, no. 4, pp. 046010, 2011.

[29] X. L. Deán-Ben and D. Razansky, “Portable spherical array probe for volumetric real-time optoacoustic imaging at centimeter-scale depths.,” *Opt. Express*, vol. 21, no. 23, pp. 28062–71, 2013.

[30] X. L. Deán-Ben and D. Razansky, “Adding fifth dimension to optoacoustic imaging : volumetric time-resolved spectrally enriched tomography.,” *Light Sci. Appl.*, vol. 3, no. e137;, pp. 1–5, 2014.

[31] X. L. Deán-Ben, S. J. Ford, and D. Razansky, “High-frame rate four dimensional optoacoustic tomography enables visualization of cardiovascular dynamics and mouse heart perfusion.,” *Sci. Rep.*, vol. 5, no. November, pp. 1-5, 2015.

[32] S. Gottschalk, T. F. Fehm, X. L. Deán-Ben, and D. Razansky, “Noninvasive real-time visualization of multiple cerebral hemodynamic parameters in whole mouse brains using five-dimensional optoacoustic tomography.,” *J. Cereb. Blood Flow Metab.*, vol. 35, no. 4, pp. 531–535, 2015.

[33] P. Beard, “Biomedical photoacoustic imaging.,” *Interface Focus*, vol. 1, no. 4, pp. 602–31, Aug. 2011.

[34] C. Li and L. V Wang, “Photoacoustic tomography and sensing in biomedicine.,” *Phys. Med. Biol.*, vol. 54, no. 19, pp. R59–97, Oct. 2009.

[35] M. Xu and L. Wang, “Universal back-projection algorithm for photoacoustic computed tomography.,” *Phys. Rev. E*, vol. 71, no. 1, pp. 016706, Jan. 2005.

[36] P. Mohajerani, S. Kellnberger, and V. Ntziachristos, “Fast Fourier backprojection for frequency-domain optoacoustic tomography.,” *Opt. Lett.*, vol. 39, no. 18, pp. 5455, Sep. 2014.

[37] A. Rosenthal, V. Ntziachristos, and D. Razansky, “Model-based optoacoustic inversion with arbitrary-shape detectors.,” *Med. Phys.*, vol. 38, no. 7, pp. 4285, 2011.

[38] A. Rosenthal, D. Razansky, and V. Ntziachristos, “Fast semi-analytical model-based acoustic inversion for quantitative optoacoustic tomography.,” *IEEE Trans. Med. Imaging*, vol. 29, no. 6, pp. 1275–85, 2010.

[39] X. L. Deán-Ben, V. Ntziachristos, and D. Razansky, “Acceleration of optoacoustic model-based reconstruction using angular image discretization.,” *IEEE Trans. Med. Imaging*, vol. 31, no. 5, pp. 1154–1162, 2012.

[40] R. Penrose, “A generalized inverse for matrices.,” *Mathematical proceedings of the Cambridge philosophical society*, vol. 51, no. 03, pp. 406–413, 1955.

[41] A. Buehler, A. Rosenthal, T. Jetzfellner, A. Dima, D. Razansky, and V. Ntziachristos, “Model-based optoacoustic inversions with incomplete projection data.,” *Med. Phys.*, vol. 38, no. 3, pp. 1694, 2011.

[42] S. Kellnberger, N. C. Deliolanis, D. Queirós, G. Sergiadis, and V. Ntziachristos, “In vivo frequency domain optoacoustic tomography.,” *Opt. Lett.*, vol. 37, no. 16, pp. 3423, 2012.

[43] J. Provost and F. Lesage, “The application of compressed sensing for photo-acoustic tomography.,” *Med. Imaging, IEEE Trans.*, vol. 28, no. 4, pp. 585–594, 2009.

[44] A. G. P. Luke and S. Y. Emelianov, “Optimization of in vivo spectroscopic photoacoustic imaging by smart optical wavelength selection.,” *Opt. Lett.*, vol. 39, no. 7, pp. 2214–2217, 2014.

[45] N. Keshava, “A Survey of Spectral Unmixing Algorithms.,” *Lincoln Lab. J.*, vol. 14, no. 1, pp. 55–78, 2003.

[46] D. Razansky, J. Baeten, and V. Ntziachristos, “Sensitivity of molecular target detection by multispectral optoacoustic tomography (MSOT).,” *Med. Phys.*, vol. 36, no. 3, pp. 939, 2009.

[47] I. Jolliffe, *Principal component analysis*. Wiley Online Library, 2002.

[48] A. Hyvärinen, “Fast and Robust Fixed-Point Algorithms for Independent Component Analysis,” vol. 10, no. 3, pp. 626–634, 1999.

[49] J. Glatz, N. C. Deliolanis, A. Buehler, D. Razansky, and V. Ntziachristos, “Blind source unmixing in multi-spectral optoacoustic tomography.,” *Opt. Express*, vol. 19, no. 4, pp. 3175–84, 2011.

[50] J. M. P. Nascimento and J. M. B. Dias, “Vertex component analysis: A fast algorithm to unmix hyperspectral data.,” *IEEE Trans. Geosci. Remote Sens.*, vol. 43, no. 4, pp. 898–910, 2005.

[51] L. D. Liao, M. L. Li, H. Y. Lai, Y. Y. I. Shih, Y. C. Lo, S. Tsang, P. C. P. Chao, C. T. Lin, F.-S. Jaw, and Y. Y. Chen, “Imaging brain hemodynamic changes during rat forepaw electrical stimulation using functional photoacoustic microscopy.,” *Neuroimage*, vol. 52, no. 2, pp. 562–70, 2010.

[52] R. M. Weight, J. A. Viator, P. S. Dale, C. W. Caldwell, and A. E. Lisle, “Photoacoustic detection of metastatic melanoma cells in the human circulatory system.,” *Opt. Lett.*, vol. 31, no. 20, pp. 2998–3000, 2006.

[53] B. Wang, A. Karpiouk, D. Yeager, R. , James Amirian, Silvio Litovsky, and S. E. Smalling, “In vivo intravascular ultrasound-guided photoacoustic imaging of lipid in plaques using an animal model of atherosclerosis.,” *Ultrasound Med Biol.*, vol. 38, no. 23, pp. 2098–2013, 2012.

[54] S. Prahl, “Optical properties spectra compiled by Scott Prahl,” 2001, http://omlc.org/spectra/.

[55] G. S. Filonov, A. Krumholz, J. Xia, J. Yao, L. V Wang, and V. V Verkhusha, “Deep-tissue photoacoustic tomography of a genetically encoded near-infrared fluorescent probe.,” *Angew. Chem. Int. Ed. Engl.*, vol. 51, no. 6, pp. 1448–51, 2012.

[56] K. D. Piatkevich, F. V Subach, and V. V Verkhusha, “Far-red light photoactivatable near-infrared fluorescent proteins engineered from a bacterial phytochrome.,” *Nat. Commun.*, vol. 4, pp. 2153, 2013.

[57] L. V. Wang and S. Hu, “Photoacoustic Tomography: In Vivo Imaging from Organelles to Organs.,” *Science*, vol. 335, no. 6075, pp. 1458–1462, 2012.

[58] L. Li, R. J. Zemp, G. Lungu, G. Stoica, and L. V Wang, “Photoacoustic imaging of lacZ gene expression in vivo.,” *J. Biomed. Opt.*, vol. 12, no. 2, pp. 020504, 2007.

[59] A. Taruttis, S. Morscher, N. C. Burton, D. Razansky, and V. Ntziachristos, “Fast Multispectral Optoacoustic Tomography (MSOT) for Dynamic Imaging of Pharmacokinetics and Biodistribution in Multiple Organs.,” *PLoS One*, vol. 7, no. 1, pp. e30491, 2012.

[60] D. Razansky, C. Vinegoni, and V. Ntziachristos, “Multispectral photoacoustic imaging of fluorochromes in small animals.,” *Opt. Lett.*, vol. 32, no. 19, pp. 2891–2893, 2007.

[61] C. Bao, N. Beziere, P. del Pino, B. Pelaz, G. Estrada, F. Tian, V. Ntziachristos, J. M. de la Fuente, and D. Cui, “Gold nanoprisms as optoacoustic signal nanoamplifiers for in vivo bioimaging of gastrointestinal cancers.,” *Small*, vol. 9, no. 1, pp. 68–74, 2013.

[62] A. C. Rudine, M. A. Sutherland, L. Hulbert, J. L. Morrow and J. J. Mcglone, “Diverse production system and social status effects on pig immunity and behavior.,” *Livest. Sci.*, vol. 111, no. 1–2, pp. 86–95, 2007.

[63] P. A . Riley, “Melanin.,” *Int J Biochem Cell Biol*, vol. 29, no. 11, pp. 1235–1239, 1997.

[64] H. F. Zhang, K. Maslov, G. Stoica, and L. V Wang, “Functional photoacoustic microscopy for high-resolution and noninvasive in vivo imaging.,” *Nat. Biotechnol.*, vol. 24, no. 7, pp. 848–51, Jul. 2006.

[65] L. Nie and X. Chen, “Structural and functional photoacoustic molecular tomography aided by emerging contrast agents.,” *Chem. Soc. Rev.*, vol. 43, pp. 7132–7170, 2014.

[66] V. Ntziachristos and D. Razansky, “Molecular imaging by means of multispectral optoacoustic tomography (MSOT).,” *Chem. Rev.*, vol. 110, no. 5, pp. 2783–94, 2010.

[67] D. Wu, L. Huang, M. Jiang, and H. Jiang, “Contrast Agents for Photoacoustic and Thermoacoustic Imaging: A Review.,” *Int. J. Mol. Sci.*, vol. 15, no. 12, pp. 23616–23639, 2014.

[68] C. Kim, C. Favazza, and L. V. Wang, “In vivo photoacoustic tomography of chemicals: High-resolution functional and molecular optical imaging at new depths.,” *Chem. Rev.*, vol. 110, no. 5, pp. 2756–2782, 2010.

[69] M. A. Van Der Horst and K. J. Hellingwerf, “Photoreceptor Proteins, ‘Star Actors of Modern Times’: A Review of the Functional Dynamics in the Structure of Representative Members of Six Different Photoreceptor Families.,” *Acc. Chem. Res.*, vol. 37, no. 1, pp. 13–20, 2004.

[70] A. Krumholz, D. M. Shcherbakova, J. Xia, L. V Wang, and V. V Verkhusha, “Multicontrast photoacoustic in vivo imaging using near-infrared fluorescent proteins.,” *Sci. Rep.*, vol. 4, p. 3939, 2014.

[71] J. Laufer, A. Jathoul, M. Pule, and P. Beard, “In vitro characterization of genetically expressed absorbing proteins using photoacoustic spectroscopy.,” *Biomed. Opt. Express*, vol. 4, no. 11, pp. 2477–90, 2013.

[72] G. S. Filonov, K. D. Piatkevich, L.-M. Ting, J. Zhang, K. Kim, and V. V Verkhusha, “Bright and stable near-infrared fluorescent protein for in vivo imaging.,” *Nat. Biotechnol.*, vol. 29, no. 8, pp. 757–61, 2011.

[73] Y. Tanaka, N. Sasaki, and A. Ohmiya, “Biosynthesis of plant pigments: Anthocyanins, betalains and carotenoids.,” *Plant J.*, vol. 54, no. 4, pp. 733–749, 2008.

[74] A. Andreoni, U. Bernini, M. Mastrocinque, E. Quarto, and P. Russo, “Quantitative measurements of porphyrin pigments in tissues via photoacoustic spectroscopy.,” *J. Biochem. Biophys. Methods*, vol. 20, no. 3, pp. 195–205, 1990.

[75] M. V Jagannadham, K. Narayanan, C. M. Rao, and S. Shivaji, “In vivo characteristics and localisation of carotenoid pigments in psychrotrophic and mesophilic Micrococcus roseus using photoacoustic spectroscopy.,” *Biochem. Biophys. Res. Commun.*, vol. 227, no. 1, pp. 221–6, Oct. 1996.

[76] R. Weissleder and V. Ntziachristos, “Shedding light onto live molecular targets.,” *Nat. Med.*, vol. 9, no. 1, pp. 123–128, 2003.

[77] C. Qin, K. Cheng, K. Chen, X. Hu, Y. Liu, X. Lan, Y. Zhang, H. Liu, Y. Xu, L. Bu, X. Su, X.

Zhu, S. Meng, and Z. Cheng, “Tyrosinase as a multifunctional reporter gene for Photoacoustic/MRI/PET triple modality molecular imaging.,” *Sci. Rep.*, vol. 3, p. 1490, 2013.

[78] R. J. Paproski, A. Heinmiller, K. Wachowicz, and R. J. Zemp, “Multi-wavelength photoacoustic imaging of inducible tyrosinase reporter gene expression in xenograft tumors.,” *Sci. Rep.*, vol. 4, p. 05329, 2014.

[79] J. Stritzker, L. Kirscher, M. Scadeng, N. C. Deliolanis, S. Morscher, P. Symvoulidis, K. Schaefer, Q. Zhang, L. Buckel, M. Hess, and U. Donat, “Vaccinia virus-mediated melanin production allows MR and optoacoustic deep tissue imaging and laser-induced thermotherapy of cancer.,” *Proc. Natl. Acad. Sci.*, vol. 110, no. 9, pp. 3316–3320, 2013.

[80] A. P. Jathoul, J. Laufer, O. Ogunlade, B. Treeby, B. Cox, E. Zhang, P. Johnson, A. R. Pizzey, B. Philip, T. Marafioti, M. F. Lythgoe, R. B. Pedley, M. A. Pule, and P. Beard, “Deep in vivo photoacoustic imaging of mammalian tissues using a tyrosinase-based genetic reporter.,” *Nat. Photonics*, vol. 9, no. 22, pp. 239–246, 2015.

[81] X. Cai, L. Li, A. Krumholz, Z. Guo, T. N. Erpelding, C. Zhang, Y. Zhang, Y. Xia, and L. V Wang, “Multi-scale molecular photoacoustic tomography of gene expression.,” *PLoS One*, vol. 7, no. 8, pp. e43999, 2012.

[82] J. Levi, S. R. Kothapalli, T.-J. Ma, K. Hartman, B. T. Khuri-Yakub, and S. S. Gambhir, “Design, synthesis, and imaging of an activatable photoacoustic probe.,” *J. Am. Chem. Soc.*, vol. 132, no. 32, pp. 11264–9, 2010.

[83] Y. Y. Jiang, F. Sigmund, J. Reber, X. Luís Deán-Ben, S. Glasl, M. Kneipp, H. Estrada, D. Razansky, V. Ntziachristos, and G. G. Westmeyer, “Violacein as a genetically-controlled, enzymatically amplified and photobleaching-resistant chromophore for optoacoustic bacterial imaging.,” *Sci. Rep.*, vol. 5, pp. 11048, 2015.

[84] K. Melican and A. Richter-Dahlfors, “Real-time live imaging to study bacterial infections in vivo.,” *Curr. Opin. Microbiol.*, vol. 12, no. 1, pp. 31–36, 2009.

[85] J. F. Rawls, M. a Mahowald, A. L. Goodman, C. M. Trent, and J. I. Gordon, “In vivo imaging and genetic analysis link bacterial motility and symbiosis in the zebrafish gut.,” *Proc. Natl. Acad. Sci. U. S. A.*, vol. 104, no. 18, pp. 7622–7627, 2007.

[86] M. Cronin, A. R. Akin, S. a Collins, J. Meganck, J. B. Kim, C. K. Baban, S. A. Joyce, G. M. van Dam, N. Zhang, D. van Sinderen, G. C. O’Sullivan, N. Kasahara, C. G. Gahan, K. P. Francis, and M. Tangney, “High resolution in vivo bioluminescent imaging for the study of bacterial tumour targeting.,” *PLoS One*, vol. 7, no. 1, pp. e30940, 2012.

[87] J. J. Min, V. H. Nguyen, H. J. Kim, Y. Hong, and H. E. Choy, “Quantitative bioluminescence imaging of tumor-targeting bacteria in living animals.,” *Nat. Protoc.*, vol. 3, no. 4, pp. 629–636, 2008.

[88] K. P. Francis, D. Joh, C. Bellinger-kawahara, M. J. Hawkinson, T. F. Purchio, R. Pamela, and P. R. Contag, “Monitoring Bioluminescent Staphylococcus aureus Infections in Living Mice Using a Novel luxABCDE Construct.,” *Infect. Immun.*, vol. 68, no. 6, pp. 3594–3600, 2000.

[89] P. J. Hill, J. Stritzker, M. Scadeng, U. Geissinger, D. Haddad, C. Thomas, U. Gbureck, P. Jakob, and A. A. Szalay, “Magnetic Resonance Imaging of Tumors Colonized with Bacterial Ferritin-Expressing Escherichia coli.,” *PLoS One*, vol. 6, no. 10, 2011.

[90] S. A. Soghomonyan, M. Doubrovin, J. Pike, X. Luo, M. Ittensohn, J. D. Runyan, J. Balatoni, R.

Finn, J. G. Tjuvajev, R. Blasberg, and D. Bermudes, “Positron emission tomography (PET) imaging of tumor-localized Salmonella expressing HSV1-TK.,” *Cancer Gene Ther.*, vol. 12, no. 1, pp. 101–108, 2005.

[91] D. A. Nedosekin, M. A. Juratli, M. Sarimollaoglu, C. L. Moore, N. J. Rusch, M. S. Smeltzer, V. P. Zharov, and E. I. Galanzha, “Photoacoustic and photothermal detection of circulating tumor cells, bacteria and nanoparticles in cerebrospinal fluid in vivo and ex vivo.,” *J. Biophotonics*, vol. 533, no. 6, pp. 523–533, 2013.

[92] C. M. Dobson, “Chemical space and biology.,” *Nature*, vol. 432, no. 7019, pp. 824–828, 2004.

[93] D. J. Newman and G. M. Cragg, “Natural Products as Sources of New Drugs over the Last 25 Years.,” *J. Nat. prof.*, vol. 66, pp. 1022–1037, 2003.

[94] R. J. Paproski, A. E. Forbrich, K. Wachowicz, M. M. Hitt, and R. J. Zemp, “Tyrosinase as a dual reporter gene for both photoacoustic and magnetic resonance imaging.,” *Biomed. Opt. Express*, vol. 2, no. 4, pp. 771–780, 2011.

[95] C. Sánchez, A. F. Braña, C. Méndez, and J. A. Salas, “Reevaluation of the violacein biosynthetic pathway and its relationship to indolocarbazole biosynthesis.,” *ChemBioChem*, vol. 7, no. 8, pp. 1231–1240, 2006.

[96] S. Y. Choi, K. Yoon, J. Il Lee, and R. J. Mitchell, “Violacein : Properties and Production of a Versatile Bacterial Pigment.,” 2014.

[97] J. Turner, M. Kneipp, and D. Razansky, “Real-time optoacoustic brain microscopy with hybrid optical and acoustic resolution.,” vol. 597, no. c, pp. 1–4, 2014.

[98] X. L. Deán-Ben, A. Buehler, V. Ntziachristos, and D. Razansky, “Accurate model-based reconstruction algorithm for three-dimensional optoacoustic tomography.,” *IEEE Trans. Med. Imaging*, vol. 31, no. 10, pp. 1922–8, 2012.

[99] A. Sarantopoulos, G. Themelis, and V. Ntziachristos, “Imaging the bio-distribution of fluorescent probes using multispectral epi-illumination cryoslicing imaging.,” *Mol. Imaging Biol.*, vol. 13, no. 5, pp. 874–85, 2011.

[100] J. S. Cho, J. Zussman, N. P. Donegan, R. I. Ramos, N. C. Garcia, D. Z. Uslan, Y. Iwakura, S. I. Simon, A. L. Cheung, R. L. Modlin, J. Kim, and L. S. Miller, “Noninvasive in vivo imaging to evaluate immune responses and antimicrobial therapy against Staphylococcus aureus and USA300 MRSA skin infections.,” *J. Invest. Dermatol.*, vol. 131, no. 4, pp. 907–915, 2011.

[101] R. J. Gonzalez, E. H. Weening, R. Frothingham, G. D. Sempowski, and V. L. Miller, “Bioluminescence imaging to track bacterial dissemination of Yersinia pestis using different routes of infection in mice.,” *BMC Microbiol.*, vol. 12, no. 1,pp. 147, 2012.

[102] S. L. La Rosa, P. G. Casey, C. Hill, D. B. Diep, I. F. Nes, and D. A. Brede, “In vivo assessment of growth and virulence gene expression during commensal and pathogenic lifestyles of luxABCDE-tagged Enterococcus faecalis strains in murine gastrointestinal and intravenous infection models.,” *Appl. Environ. Microbiol.*, vol. 79, no. 13, pp. 3986–3997, 2013.

[103] Y. A. Yu, S. Shabahang, T. M. Timiryasova, Q. Zhang, R. Beltz, I. Gentschev, W. Goebel, and A. A. Szalay, “Visualization of tumors and metastases in live animals with bacteria and vaccinia virus encoding light-emitting proteins.,” *Nat. Biotechnol.*, vol. 22, no. 3, pp. 313–320, 2004.

[104] J. Laufer, A. Jathoul, M. Pule, and P. Beard, “In vitro characterization of genetically expressed absorbing proteins using photoacoustic spectroscopy.,” *Biomed. Opt. Express*, vol. 4, no. 11, pp. 2477–90, 2013.

[105] S. Belkin, “Microbial whole-cell sensing systems of environmental pollutants.,” *Curr. Opin. Microbiol.*, vol. 6, no. 3, pp. 206–212, 2003.

[106] N. S. Forbes, “Engineering the perfect (bacterial) cancer therapy.,” *Nat. Rev. Cancer*, vol. 10, no. 11, pp. 785–794, 2010.

[107] A. C. Stiel, X. L. Deán-Ben, Y. Y. Jiang, V. Ntziachristos, D. Razansky, and G. G. Westmeyer, “High-contrast imaging of reversibly switchable fluorescent proteins via temporally unmixed multispectral optoacoustic tomography.,” *Opt. Lett.*, vol. 40, no. 3, pp. 367-370, 2015.

[108] X. L. Deán-Ben, A. C. Stiel, Y. Jiang, V. Ntziachristos, G. G. Westmeyer, and D. Razansky, “Light fluence normalization in turbid tissues via temporally unmixed multispectral optoacoustic tomography.,” *Opt. Lett.*, vol. 40, no. 20, pp. 4691–4694, 2015.

[109] A. Krumholz, S. J. Vanvickle-Chavez, J. Yao, T. P. Fleming, W. E. Gillanders, and L. V Wang, “Photoacoustic microscopy of tyrosinase reporter gene in vivo.,” *J. Biomed. Opt.*, vol. 16, pp. 080503, 2011.

[110] D. M. Shcherbakova, P. Sengupta, J. Lippincott-Schwartz, and V. V Verkhusha, “Photocontrollable fluorescent proteins for superresolution imaging.,” *Annu. Rev. Biophys.*, vol. 43, pp. 303–29, 2014.

[111] G. H. Patterson, “A Photoactivatable GFP for Selective Photolabeling of Proteins and Cells.,” *Science.*, vol. 297, no. 5588, pp. 1873–1877, 2002.

[112] C. Eggeling, M. Hilbert, H. Bock, C. Ringemann, M. Hofmann, A. C. Stiel, M. Andresen, S. Jakobs, A. Egner, A. Schönle, and S.W. Hell, “Reversible photoswitching enables single-molecule fluorescence fluctuation spectroscopy at high molecular concentration.,” *Microsc. Res. Tech.*, vol. 70, no. 12, pp. 1003–1009, 2007.

[113] E. Betzig, G. H. Patterson, R. Sougrat, O. W. Lindwasser, S. Olenych, J. S. Bonifacino, M. W. Davidson, J. Lippincott-Schwartz, and H. F. Hess, “Imaging intracellular fluorescent proteins at nanometer resolution.,” *Science*, vol. 313, no.5793, pp. 1642–1645, 2006.

[114] S. W. Hell and J. Wichman, “Breaking the diffraction resolution limit by stimulated emission: stimulated-emission-depletion fluorescence microscopy.,” *Opt. Lett.*, vol. 19, no. 11, pp. 780 – 782, 1994.

[115] T. A Klar, S. Jakobs, M. Dyba, a Egner, and S. W. Hell, “Fluorescence microscopy with diffraction resolution barrier broken by stimulated emission.,” *Proc. Natl. Acad. Sci. U. S. A.*, vol. 97, no. 15, pp. 8206–8210, 2000.

[116] M. J. Rust, M. Bates, and X. Zhuang, “Sub-diffraction-limit imaging by stochastic optical reconstruction microscopy (STORM).,” *Nat. Methods*, vol. 3, no. 10, pp. 793–796, 2006.

[117] G. Marriott, S. Mao, T. Sakata, J. Ran, D. K. Jackson, C. Petchprayoon, T. J. Gomez, E. Warp, O. Tulyathan, H. L. Aaron, E. Y. Isacoff, and Y. Yan, “Optical lock-in detection imaging microscopy for contrast-enhanced imaging in living cells.,” *Proc. Natl. Acad. Sci. U. S. A.*, vol. 105, no. 46, pp. 17789–17794, 2008.

[118] Z. Tian and A. D. Q. Li, “Photoswitching-enabled novel optical imaging: Innovative solutions

for real-world challenges in fluorescence detections.," *Acc. Chem. Res.*, vol. 46, no. 2, pp. 269–279, 2013.

[119] M. Andresen, A. C. Stiel, S. Trowitzsch, G. Weber, C. Eggeling, M. C. Wahl, S. W. Hell, and S. Jakobs, "Structural basis for reversible photoswitching in Dronpa.," *Proc. Natl. Acad. Sci. U. S. A.*, vol. 104, no. 32, pp. 13005–13009, 2007.

[120] A. C. Stiel, S. Trowitzsch, G. Weber, M. Andresen, C. Eggeling, S. W. Hell, S. Jakobs, and M. C. Wahl, "1.8 A bright-state structure of the reversibly switchable fluorescent protein Dronpa guides the generation of fast switching variants.," *Biochem. J.*, vol. 402, no. 1, pp. 35–42, Feb. 2007.

[121] R. Ando, H. Mizuno, and A. Miyawaki, "Regulated fast nucleocytoplasmic shuttling observed by reversible protein highlighting.," *Science*, vol. 306, no. 5700, pp. 1370–1373, 2004.

[122] M. Kaucikas, M. Tros, and J. J. van Thor, "Photoisomerization and Proton Transfer in the Forward and Reverse Photoswitching of the Fast-Switching M159T Mutant of the Dronpa Fluorescent Protein.," *J. Phys. Chem. B*, vol. 119, no. 6, pp. 2350–2362, 2015.

[123] S. Habuchi, P. Dedecker, J. Hotta, C. Flors, R. Ando, H. Mizuno, A. Miyawaki, and J. Hofkens, "Photo-induced protonation/deprotonation in the GFP-like fluorescent protein Dronpa: mechanism responsible for the reversible photoswitching.," *Photochem. Photobiol. Sci.*, vol. 5, no. 6, pp. 567–76, 2006.

[124] S. Habuchi, R. Ando, P. Dedecker, W. Verheijen, H. Mizuno, A. Miyawaki, and J. Hofkens, "Reversible single-molecule photoswitching in the GFP-like fluorescent protein Dronpa.," *Proc. Natl. Acad. Sci. U. S. A.*, vol. 102, no. 27, pp. 9511–9516, 2005.

[125] X. X. Zhou and M. Z. Lin, "Photoswitchable fluorescent proteins: ten years of colorful chemistry and exciting applications.," *Curr. Opin. Chem. Biol.*, vol. 17, no. 4, pp. 682–690, 2013.

[126] M. A. Haidekker and E. A. Theodorakis, "Molecular rotors--fluorescent biosensors for viscosity and flow.," *Org. Biomol. Chem.*, vol. 5, no. 11, pp. 1669-1678, 2007.

[127] Y. T. Kao, X. Zhu, and W. Min, "Protein-flexibility mediated coupling between photoswitching kinetics and surrounding viscosity of a photochromic fluorescent protein.," *Proc. Natl. Acad. Sci.*, vol. 109, no. 9, pp. 3220–3225, 2012.

[128] S. L. Jacques, "Coupling 3D Monte Carlo light transport in optically heterogeneous tissues to photoacoustic signal generation.," *Photoacoustics*, vol. 2, no. 4, pp. 137–142, 2014.

[129] M. Schweiger and S. Arridge, "The Toast++ software suite for forward and inverse modeling in optical tomography.," *J. Biomed. Opt.*, vol. 19, no. 4, pp. 040801, 2014.

[130] B. T. Cox, S. R. Arridge, K. P. Köstli, and P. C. Beard, "Two-dimensional quantitative photoacoustic image reconstruction of absorption distributions in scattering media by use of a simple iterative method.," *Appl. Opt.*, vol. 45, no. 8, pp. 1866–1875, 2006.

[131] S. L. Jacques, "Corrigendum: Optical properties of biological tissues: a review.," *Phys. Med. Biol.*, vol. 58, no. 14, pp. 5007–5008, 2013.

[132] A. Danielli, C. P. Favazza, K. Maslov, and L. V. Wang, "Picosecond absorption relaxation measured with nanosecond laser photoacoustics.," *Appl. Phys. Lett.*, vol. 97, no. 16, pp. 163701, 2010.

[133] V. P. Zharov, “Ultrasharp nonlinear photothermal and photoacoustic resonances and holes beyond the spectral limit.,” *Nat. Photonics*, vol. 5, no.2, pp. 110–116, 2011.

[134] T. Müller, C. Schumann, and A. Kraegeloh, “STED microscopy and its applications: new insights into cellular processes on the nanoscale.,” *Chemphyschem*, vol. 13, no. 8, pp. 1986–2000, 2012.

[135] J. Yao, L. Wang, J. Yang, K. I. Maslov, T. T. W. Wong, L. Li, C. Huang, J. Zou, and L. V Wang, “High-speed label-free functional photoacoustic microscopy of mouse brain in action.,” *Nat. Methods*,vol. 12, no.5, pp. 407–410, 2015.

[136] S. Ashkenazi, S.-W. Huang, T. Horvath, Y. L. Koo, and R. Kopelman, “Photoacoustic probing of fluorophore excited state lifetime with application to oxygen sensing.,” *J. Biomed. Opt.*, vol. 13, no. 3, pp. 034023, 2013.

[137] V. N. Belov, C. A. Wurm, V. P. Boyarskiy, S. Jakobs, and S. W. Hell, “Rhodamines NN: a novel class of caged fluorescent dyes.,” *Angew. Chem. Int. Ed. Engl.*, vol. 49, no. 20, pp. 3520–3, 2010.

[138] Y. J. Lin and A. P. Koretsky, “Manganese ion enhances T1-weighted MRI during brain activation: an approach to direct imaging of brain function.,” *Magn. Reson. Med.*, vol. 38, no. 3, pp. 378–88, 1997.

[139] R. Weissleder and U. Mahmood, “Molecular Imaging.,” *Radiology*, vol. 219, no. 2, pp. 316–333, 2001.

[140] W. M. Pardridge, “Blood-brain barrier drug targeting: the future of brain drug development.,” *Mol. Interv.*, vol. 3, no. 2, pp. 90–105, 51, 2003.

[141] W. Pardridge, “Non-invasive drug delivery to the human brain using endogenous blood-brain barrier transport systems.,” *Pharm. Sci. Technolo. Today*, vol. 2, no. 2, pp. 49–59, 1999.

[142] N. D. Doolittle, M. E. Miner, W. a Hall, T. Siegal, E. Jerome, E. Osztie, L. D. McAllister, J. S. Bubalo, D. F. Kraemer, D. Fortin, R. Nixon, L. L. Muldoon, and E. a Neuwelt, “Safety and efficacy of a multicenter study using intraarterial chemotherapy in conjunction with osmotic opening of the blood-brain barrier for the treatment of patients with malignant brain tumors.,” *Cancer*, vol. 88, no. 3, pp. 637–647, 2000.

[143] K. Matsukado, M. Sugita, and K. L. Black, “Intracarotid low dose bradykinin infusion selectively increases tumor permeability through activation of bradykinin B2 receptors in malignant gliomas.,” *Brain Res.*, vol. 792, no. 1, pp. 10–15, 1998.

[144] B. Oztas and M. Kucuk, “Intracarotid hypothermic saline infusion: A new method for reversible blood-brain barrier disruption in anesthetized rats.,” *Neurosci. Lett.*, vol. 190, no. 3, pp. 203–206, 1995.

[145] A. Nadal, E. Fuentes, J. Pastor, and P. A McNaughton, “Plasma albumin is a potent trigger of calcium signals and DNA synthesis in astrocytes.,” *Proc. Natl. Acad. Sci. U. S. A.*, vol. 92, no. 5, pp. 1426–1430, 1995.

[146] S. I. Rapoport, “Osmotic opening of the blood-brain barrier: Principles, mechanism, and therapeutic applications.,” *Cell. Mol. Neurobiol.*, vol. 20, no. 2, pp. 217–230, 2000.

[147] K. Hynynen, N. McDannold, N. A. Sheikov, F. A Jolesz, and N. Vykhodtseva, “Local and reversible blood-brain barrier disruption by noninvasive focused ultrasound at frequencies

suitable for trans-skull sonications.," *Neuroimage*, vol. 24, no. 1, pp. 12–20, 2005.

[148] J. J. Choi, M. Pernot, S. a Small, and E. E. Konofagou, "Noninvasive, transcranial and localized opening of the blood-brain barrier using focused ultrasound in mice.," *Ultrasound Med. Biol.*, vol. 33, no. 1, pp. 95–104, 2007.

[149] Y. S. Tung, F. Marquet, T. Teichert, V. Ferrera, and E. E. Konofagou, "Feasibility of noninvasive cavitation-guided blood-brain barrier opening using focused ultrasound and microbubbles in nonhuman primates.," *Appl. Phys. Lett.*, vol. 98, no. 16, pp. 163704, 2011.

[150] F. J. F. andRolfs F. K. John W. Barnard, William J. Fry, "Effects of high intensity ultrasound on the central nervous system of the cat.," *Issue J. Comp. Neurol. J. Comp. Neurol.*, vol. 103, no. 3, pp. 459–484, 1955.

[151] N. I. Vykhodtseva, K. Hynynen, and C. Damianou, "Histologic effects of high intensity pulsed ultrasound exposure with subharmonic emission in rabbit brain in vivo.," *Ultrasound Med. Biol.*, vol. 21, no. 7, pp. 969–979, 1995.

[152] K. H. Natalia Vykhodtseva, N. McDannold, "Progress and problems in the application of focused ultrasound for blood–brain barrier disruption." *Ultrasonics*, vol. 48, no. 4, pp. 279–296, 2008.

[153] F. J. Fry and J. E. Barger, "Acoustical properties of the human skull.," *J. Acoust. Soc. Am.*, vol. 63, no. 5, pp. 1576–1590, 1978.

[154] K. Hynynen, N. McDannold, N. Vykhodtseva and F. A. Jolsez, "Nonivasive MR Imaging – guided Focal Opening of the Blood-Brain Barrier in Rabbits.," *Radiology*, vol. 220, no. 3, pp. 641–646, 2001.

[155] J. J. Choi, M. Pernot, T. R. Brown, S. A. Small, and E. E. Konofagou, "Spatio-temporal analysis of molecular delivery through the blood-brain barrier using focused ultrasound.," *Phys. Med. Biol.*, vol. 52, no. 18, pp. 5509–30, 2007.

[156] F. Y. Yang and P. Y. Lee, "Efficiency of drug delivery enhanced by acoustic pressure during blood-brain barrier disruption induced by focused ultrasound.," *Int. J. Nanomedicine*, vol. 7, pp. 2573–2582, 2012.

[157] F. Xie, M. D. Boska, J. Lof, M. G. Uberti, J. M. Tsutsui, and T. R. Porter, "Effects of transcranial ultrasound and intravenous microbubbles on blood brain barrier permeability in a large animal model.," *Ultrasound Med. Biol.*, vol. 34, no. 12, pp. 2028–2034, 2008.

[158] K. Ferrara, R. Pollard, and M. Borden, "Ultrasound microbubble contrast agents: fundamentals and application to gene and drug delivery.," *Annu. Rev. Biomed. Eng.*, vol. 9, pp. 415–447, 2007.

[159] K. W. Ferrara, "Driving delivery vehicles with ultrasound.," *Adv. Drug Deliv. Rev.*, vol. 60, no. 10, pp. 1097–1102, 2008.

[160] L. K. Bengez, M. R. Mayberg, and D. Janigro, "The cerebral vasculature as a therapeutic target for neurological disorders and the role of shear stress in vascular homeostatis and pathophysiology.," *Neurol. Res.*, vol. 26, no. 8, pp. 846–853, 2004.

[161] Y. S. Tung, F. Vlachos, J. A. Feshitan, M. A. Borden, and E. E. Konofagou, "The mechanism of interaction between focused ultrasound and microbubbles in blood-brain barrier opening in mice.," *J. Acoust. Soc. Am.*, vol. 130, no. 5, pp. 3059–67, 2011.

[162] N. Vykhodtseva, N. McDannold, and K. Hynynen, "Progress and problems in the application of focused ultrasound for blood-brain barrier disruption." *Ultrasonics*, vol. 48, no. 4, pp. 279–296, 2008.

[163] N. Sheikov, N. McDannold, N. Vykhodtseva, F. Jolesz, and K. Hynynen, "Cellular mechanisms of the blood-brain barrier opening induced by ultrasound in presence of microbubbles.," *Ultrasound Med. Biol.*, vol. 30, no. 7, pp. 979–989, 2004.

[164] N. Sheikov, N. McDannold, S. Sharma , and K. Hynynen, "Effect of focused ultrasound applied with an ultrasound contrast agent on the tight junctional integrity of the brain microvascular endothelium.," *Ultrasound Med Biol*, vol. 34, no. 7, pp. 1093–1104, 2009.

[165] F. Vlachos, Y. S. Tung, and E. Konofagou, "Permeability dependence study of the focused ultrasound-induced blood-brain barrier opening at distinct pressures and microbubble diameters using DCE-MRI.," *Magn. Reson. Med.*, vol. 66, no. 3, pp. 821–830, 2011.

[166] E. Sassaroli and K. Hynynen, "Resonance frequency of microbubbles in small blood vessels: a numerical study.," *Phys. Med. Biol.*, vol. 50, no. 22, pp. 5293–5305, 2005.

[167] S. Qin and K. W. Ferrara, "The natural frequency of nonlinear oscillation of ultrasound contrast agents in microvessels.," *Ultrasound Med. Biol.*, vol. 33, no. 7, pp. 1140–1148, 2007.

[168] N. Nishimura, C. B. Schaffer, B. Friedman, P. D. Lyden, and D. Kleinfeld, "Penetrating arterioles are a bottleneck in the perfusion of neocortex.," *Proc. Natl. Acad. Sci. U. S. A.*, vol. 104, no. 1, pp. 365–370, 2007.

[169] B. V. Zlokovic, "The blood-brain barrier in health and chronic neurodegenerative disorders.," *Neuron*, vol. 57, no. 2, pp. 178–201, 2008.

[170] F. Marquet, Y.-S. Tung, and E. E. Konofagou, "Feasibility Study of a Clinical Blood–Brain Barrier Opening Ultrasound System.," *Nano Life*, vol. 01, no. 03n04, pp. 309-322, 2010.

[171] H. Chen and E. E. Konofagou, "The size of blood-brain barrier opening induced by focused ultrasound is dictated by the acoustic pressure.," *J. Cereb. Blood Flow Metab.*, no. pp. 1–8, 2014.

[172] M. Schneider, "SonoVue, a new ultrasound contrast agent.," *Eur. Radiol.*, vol. 9 Suppl 3, pp. S347–S348, 1999.

[173] M. Schneider, "Characteristics of SonoVue™.," *Echocardiography*, vol. 16, pp. 743–746, 1999.

[174] J. J. Choi, S. Member, J. A. Feshitan, B. Baseri, S. Wang, Y. Tung, M. A. Borden, and E. E. Konofagou, "Microbubble-Size Dependence of Focused Ultrasound-Induced Blood–Brain Barrier Opening in Mice In Vivo.," *Biomed. Eng. (NY).*, vol. 57, no. 1, pp. 145–154, 2010.

[175] L. H. Treat, N. McDannold, N. Vykhodtseva, Y. Zhang, K. Tam, and K. Hynynen, "Targeted delivery of doxorubicin to the rat brain at therapeutic levels using MRI-guided focused ultrasound.," *Int. J. Cancer*, vol. 121, no. 4, pp. 901–907, 2007.

[176] J. W. Belliveau, D. N. Kennedy, R. C. McKinstry, B. R. Buchbinder, R. M. Weisskoff, M. S. Cohen, J. M. Vevea, T. J. Brady, and B. R. Rosen, "Functional mapping of the human visual cortex by magnetic resonance imaging.," *Science*, vol. 24, no. 5032, pp. 716–719, 1991.

[177] S. Ogawa, T. M. Lee, A. S. Nayak, and P. Glynn, "Oxygenation-sensitive contrast in magnetic resonance image of rodent brain at high magnetic fields.," *Magn. Reson. Med.*, vol. 14, no. 1,

pp. 68–78, 1990.

[178] A. Jasanoff, “Functional MRI using molecular imaging agents.,” *Trends Neurosci.*, vol. 28, no. 3, pp. 120–126, 2005.

[179] M. J. Berridge, P. Lipp, and M. D. Bootman, “The versatility and universality of calcium signalling.,” *Nat. Rev. Mol. Cell Biol.*, vol. 1, no. 1, pp. 11–21, 2000.

[180] G. G. Somjen, *Ions in the brain: normal function, seizures, and stroke*. Oxford University Press USA:, 2004.

[181] R. A. Yokel, “Manganese flux across the blood-brain barrier.,” *Neuromolecular Med.*, vol. 11, no. 4, pp. 297–310, 2009.

[182] R. Nau, F. Sörgel, and H. Eiffert, “Penetration of drugs through the blood-cerebrospinal fluid/blood-brain barrier for treatment of central nervous system infections.,” *Clin. Microbiol. Rev.*, vol. 23, no. 4, pp. 858–83, 2010.

[183] X. Yu, Y. Z. Wadghiri, D. H. Sanes, and D. H. Turnbull, “In vivo auditory brain mapping in mice with Mn-enhanced MRI.,” *Nat. Neurosci.*, vol. 8, no. 7, pp. 961–968, 2005.

[184] G. P. Howles, Y. Qi, and G. A. Johnson, “Ultrasonic disruption of the blood-brain barrier enables in vivo functional mapping of the mouse barrel field cortex with manganese-enhanced MRI.,” *Neuroimage*, vol. 50, no. 4, pp. 1464–71, 2010.

[185] P. H. Wang, H. L. Liu, P. H. Hsu, C. Y. Lin, C.R. C. Wang, P. Y. Chen, K. C. Wei, T. C. Yen, and M. L. Li, “Gold-nanorod contrast-enhanced photoacoustic micro-imaging of focused-ultrasound induced blood-brain-barrier opening in a rat model.,” *J. Biomed. Opt.*, vol. 17, no. 6, pp. 061222, 2012.

[186] H. L. Liu, P. H. Hsu, P. N. Chu, Y. Y. Wai, J. C. Chen, C. R. Shen, T. C. Yen, and J. J. Wang, “Magnetic resonance imaging enhanced by superparamagnetic iron oxide particles: Usefulness for distinguishing between focused ultrasound-induced blood-brain barrier disruption and brain hemorrhage,” *J. Magn. Reson. Imaging*, vol. 29, no. 1, pp. 31–38, 2009.

[187] S. B. Raymond, L. H. Treat, J. D. Dewey, N. J. McDannold, K. Hynynen, and B. J. Bacskai, “Ultrasound enhanced delivery of molecular imaging and therapeutic agents in Alzheimer’s disease mouse models.,” *PLoS One*, vol. 3, no. 5, pp. e2175, 2008.

[188] J. J. Choi, S. Wang, Y. S. Tung, B. Morrison, and E. E. Konofagou, “Molecules of various pharmacologically-relevant sizes can cross the ultrasound-induced blood-brain barrier opening in vivo.,” *Ultrasound Med. Biol.*, vol. 36, no. 1, pp. 58–67, 2010.

[189] M. Kinoshita, N. McDannold, F. a Jolesz, and K. Hynynen, “Noninvasive localized delivery of Herceptin to the mouse brain by MRI-guided focused ultrasound-induced blood-brain barrier disruption.,” *Proc. Natl. Acad. Sci. U. S. A.*, vol. 103, no. 31, pp. 11719–23, 2006.

[190] Z. Kovacs, P. Luciani, P. Roth, J.-C. Leroux, E. Martin, and B. Werner, “Blood-brain barrier opening-based local delivery of 80 nm-sized liposomes in mice using pulsed focused ultrasound.,” *J. Ther. Ultrasound*, vol. 3, no. Suppl 1, pp. P24, 2015.

[191] E. E. Konofagou, “Optimization of the Ultrasound-Induced Blood-Brain Barrier Opening.,” *Theranostics*, vol. 2, no. 12, pp. 1223–1237, 2012.

[192] M. D. Santin, T. Debeir, S. L. Bridal, T. Rooney, and M. Dhenain, “Fast in vivo imaging of

amyloid plaques using μ-MRI Gd-staining combined with ultrasound-induced blood-brain barrier opening.," *Neuroimage*, vol. 79, pp. 288–294, 2013.

[193] K. H. Nathan McDannold, Natalia Vykhodtseva, "Blood-brain barrier disruption induced by focused ultrasound and circulating preformed microbubbles appears to be characterized by the mechanical index.," *Ultrasound Med Biol.*, vol. 34, no. 5, pp. 834–840, 2008.

[194] H. L. Liu, M.Y. Hua, H. W. Yang, C. Y. Huang, P. C. Chu, J.-S. Wu, I. C. Tseng, J. J. Wang, T. C. Yen, P. Y. Chen, and K. C. Wei, "Magnetic resonance monitoring of focused ultrasound/magnetic nanoparticle targeting delivery of therapeutic agents to the brain.," *Proc. Natl. Acad. Sci. U. S. A.*, vol. 107, no. 34, pp. 15205–10, 2010.

[195] G. P. Howles, Y. Qi, and G. A. Johnson, "Ultrasonic disruption of the blood-brain barrier enables in vivo functional mapping of the mouse barrel field cortex with manganese-enhanced MRI.," *In Vivo (Brooklyn).*, vol. 50, no. 4, pp. 1464–1471, 2011.

[196] F. Marquet, Y.S. Tung, T. Teichert, V. P. Ferrera, and E. E. Konofagou, "Noninvasive, transient and selective blood-brain barrier opening in non-human primates in vivo.," *PLoS One*, vol. 6, no. 7, pp. e22598, Jan. 2011.

[197] Y. S. Tung, F. Vlachos, J. J. Choi, T. Deffieux, K. Selert, and E. E. Konofagou, "In vivo transcranial cavitation threshold detection during ultrasound-induced blood-brain barrier opening in mice.," *Phys. Med. Biol.*, vol. 55, no. 20, pp. 6141–55, 2010.

[198] J. J. Choi, K. Selert, Z. Gao, G. Samiotaki, B. Baseri, and E. E. Konofagou, "Noninvasive and localized blood-brain barrier disruption using focused ultrasound can be achieved at short pulse lengths and low pulse repetition frequencies.," *J. Cereb. Blood Flow Metab.*, vol. 31, no. 2, pp. 725–37, 2011.

[199] K. H. Nathan McDannold, Natalia Vykhodtseva, "Effects of acoustic parameters and ultrasound contrast agent dose on focused-ultrasound induced blood-brain barrier disruption," *Ultrasound Med. Biol.*, vol. 34, no. 6, pp. 930–937, 2008.

[200] G. P. Howles, K. F. Bing, Y. Qi, S. J. Rosenzweig, K. R. Nightingale, and G. A. Johnson, "Contrast-enhanced in vivo magnetic resonance microscopy of the mouse brain enabled by noninvasive opening of the blood-brain barrier with ultrasound.," *Magn. Reson. Med.*, vol. 64, no. 4, pp. 995–1004, 2010.

[201] A. H. Liao, H. L. Liu, C.-H. Su, M. Y. Hua, H. W. Yang, Y. T. Weng, P. H. Hsu, S. M. Huang, S.-Y. Wu, H. E. Wang, T. C. Yen, and P. C. Li, "Paramagnetic perfluorocarbon-filled albumin-(Gd-DTPA) microbubbles for the induction of focused-ultrasound-induced blood-brain barrier opening and concurrent MR and ultrasound imaging.," *Phys. Med. Biol.*, vol. 57, no. 9, pp. 2787–802, 2012.

[202] F. Yang, Y. Li, Z. Chen, Y. Zhang, J. Wu, and N. Gu, "Superparamagnetic iron oxide nanoparticle-embedded encapsulated microbubbles as dual contrast agents of magnetic resonance and ultrasound imaging.," *Biomaterials*, vol. 30, no. 23–24, pp. 3882–90, 2009.

[203] B. Baseri, J. J. Choi, Y. S. Tung and E. E. Konofagou, "Multi-Modality Safety Assessment of Blood-Brain Barrier Opening Using Focused Ultrasound and Definity Microbubbles: A Short-Term Study.," *Ultrasound Med. Biol.*, vol. 36, no. 9, pp. 1145–1459, 2010.

[204] N. McDannold, N. Vykhodtseva, S. Raymond, F. A. Jolesz, and K. Hynynen, "MRI-guided targeted blood-brain barrier disruption with focused ultrasound : Histological findings in rabbits.," *Ultrasound Med. Biol.*, vol. 31, no. 11, pp. 1527–1537, 2005.

[205] J. F. Jordão, C. A. Ayala-Grosso, K. Markham, Y. Huang, R. Chopra, J. McLaurin, K. Hynynen, and I. Aubert, “Antibodies targeted to the brain with image-guided focused ultrasound reduces amyloid-β plaque load in the TgCRND8 mouse model of Alzheimer’s disease.,” *PLoS One*, vol. 5, no. 5, pp. 4–11, 2010.

[206] J. F. Jordão, E. Thévenot, E. Markham-Coultes,T. Scarcelli, Y.Q. Weng, K. Xhima K,M. O’Reilly, Y. Huang, J. McLaurin, and K. Hynynen, “Amyloid-β plaque reduction, endogenous antibody delivery and glial activation by brain-targeted, transcranial focused ultrasound.,” *Exp. Neurol.*, vol. 248, no. 6, pp. 16–29, 2013.

[207] G. Leinenga and J. Gotz, “Scanning ultrasound removes amyloid- and restores memory in an Alzheimer’s disease mouse model.,” *Sci. Transl. Med.*, vol. 7, no. 278, pp. 278ra33, 2015.

[208] J. G. Zalatan, M. E. Lee, R. Almeida, L. A. Gilbert, E. H. Whitehead, M. La Russa, J. C. Tsai, J. S. Weissman, J. E. Dueber, L. S. Qi, and W. a. Lim, “Engineering Complex Synthetic Transcriptional Programs with CRISPR RNA Scaffolds.,” *Cell*, vol. 160, no. 1, pp. 339–350, 2014.

[209] J. Yao, A. A. Kaberniuk, L. Li, D. M. Shcherbakova, R. Zhang, L. Wang, G. Li, V. V Verkhusha, and L. V. Wang, “Multiscale photoacoustic tomography using reversibly switchable bacterial phytochrome as a near-infrared photochromic probe.,” *Nat. Methods*, vol. 13,no.1, pp. 67–73, 2015.